UNIVERSITÀ DI PISA

**Facoltà di Ingegneria**

**Master Thesis in Aerospace Engineering**

# Alternative Control Strategy for Test Mass Release of Spaceborne Inertial Sensors


*Supervisors:*
Prof. Giovanni Mengali
Dipl.-Ing. Tobias Ziegler
Dipl.-Ing. Nico Brandt

*Candidate:*
Luca Trobbiani


A. A. 2012-2013

*To my family*

Abstract

In this thesis, a control strategy that maximizes exploitation of the available electrostatic actuation authority is studied, and its application to the case of the LISA Pathfinder Accelerometer Mode is carried out.
The successful catching of test masses after release from their launch lock is crucial to the operation of spaceborne inertial sensors. Due to potentially high release velocities, high electrostatic forces need to be applied while avoiding saturation of the sensor electronics. Work on the LISA Pathfinder mission showed that this particular phase is still critical and, for possible future missions, improvements of the existing design are desirable.
Three main components can be identified as involved in this particular phase: the available hardware, the force to voltage conversion law, and the test mass control law.
The present work contributes to the research of a control strategy that best exploits the available hardware, with the goal of increasing robustness of the catching process.
In order to do so, the limits of linear control are explored, by designing and comparing several different concepts. The idea of maximum actuation exploitation is then developed, and a nonlinear bang-bang velocity breaking controller is designed. An extension of the existing actuation algorithm is developed, that realizes the maximum possible force generation out of the current electronics and geometric configuration. In ideal testing environment, the new concept shows ability to exploit the system electrostatic actuation up to 96.5% of its theoretical limit. The velocity breaking controller is finally combined with a linear controller and a Kalman filter, to define a complete control strategy. Controller testing is then carried out using the nonlinear LISA Pathfinder performance simulator. Comparison with the existing design shows an improvement in maximum tolerable release velocity by a factor of approximately 2.5.

# Sommario

In questa tesi è eseguito lo studio di una strategia di controllo che sfrutti al massimo l'uso dell'attuazione elettrostatica disponibile. Ne viene poi eseguita l'applicazione al caso dell'Accelerometer Mode per la missione LISA Pathfinder.
La cattura corretta delle masse di prova dopo il rilascio dal loro alloggiamento di lancio è fondamentale per il funzionamento di sensori inerziali nello spazio. A causa delle potenzialmente elevate velocità di rilascio, si rende necessaria la possibilità di applicare elevate forze elettrostatiche, evitando allo stesso tempo saturazione dell'elettronica dello strumento. Il lavoro svolto nell'ambito della missione LISA Pathfinder ha messo in luce che questa fase è ancora critica e, per possibili missioni future, è auspicabile un miglioramento della soluzione esistente.
Tre elementi principali sono coinvolti in questa fase: l'hardware esistente, la legge di conversione forze-voltaggi, e la legge di controllo della massa.
Questo lavoro contribuisce alla ricerca di una strategia di controllo che sfrutti al meglio l'hardware esistente, con l'obiettivo di aumentare la robustezza del processo di cattura. Per fare ciò, in primo luogo sono esplorati i limiti del controllo lineare, definendo e comparando varie possibilità. In seguito, è sviluppata l'idea di sfruttamento massimo dell'attuazione, risultando nella definizione di un controllore nonlineare di tipo bang-bang per la frenata della velocità. Viene quindi sviluppata un estensione dell'attuale algoritmo di attuazione, che realizza la massima forza possibile per l'hardware esistente. In condizioni di test ideali, il nuovo metodo di controllo si dimostra capace di sfruttare l'attuazione elettrostatica fino al 96.5% del suo limite teorico. Il controllore di frenata della velocità è quindi combinato con un controllore lineare e un filtro di Kalman, così da definire una strategia di controllo completa. Vari test del controllore sono eseguiti usando il simulatore nonlineare di prestazioni della missione LISA Pathfinder. Confronti con la soluzione attuale dimostrano un incremento nella massima velocità di rilascio tollerata di un fattore 2.5 circa.

# *Acknowledgements*

This thesis is the result of a six months work at Airbus Defence and Space (former Astrium GmbH) in Friedrichshafen Germany.

I would like to express my gratitude to all the people that, in many ways, made this not only possible, but really enjoyable as well. Without mentioning them all by their names, as the list would be too long, I hope to include everybody in my sincerest thanks.

My first mention goes to Dipl.-Ing. Tobias Ziegler: thank you for the opportunity you gave me to work on such an interesting topic; for the support, for all your advices and opinions, and the patience you showed.

Thanks to Dipl.-Ing. Nico Brandt and Dipl.-Ing. Alexander Schleicher, who contributed to this work with their precious advices and experience.

Thanks to all the colleagues in Astrium, with whom I had a great time during these six months.

Thanks to my Italian and German friends, or whatever country you came from. I had a great time with you and hope you're doing well wherever you are now.

Thanks to Chiara, for the patience she showed me these last months.

# Contents


**Abstract** ii

**Sommario** iii

**Acknowledgements** iv

**Contents** v

**List of Figures** viii

**List of Tables** xi

**Preface** 1

**1 Introduction** 2
- 1.1 The LISA Experiment . . . . . 2
  - 1.1.1 The LISA Pathfinder . . . . . 3
  - 1.1.2 The eLISA Mission . . . . . 4
- 1.2 Previous Work . . . . . 5
  - 1.2.1 The LISA Pathfinder Capacitive Actuation Algorithm . . . . . 5
  - 1.2.2 The LISA Pathfinder Accelerometer Mode Controller . . . . . 5
  - 1.2.3 The Improved Capacitive Actuation Algorithm . . . . . 6
- 1.3 Motivation . . . . . 6
- 1.4 Thesis Contributions . . . . . 7

**2 System Description** 9
- 2.1 Test Mass Dynamics . . . . . 9
  - 2.1.1 Release Direction . . . . . 10
- 2.2 Electrostatic Actuation . . . . . 11
  - 2.2.1 Force Model . . . . . 11
- 2.3 Summary of Operating Conditions . . . . . 15
  - 2.3.1 Test Mass Initial States . . . . . 15
  - 2.3.2 Maximum overshoots . . . . . 15
  - 2.3.3 Control Accuracy (transition to steady state) . . . . . 15
  - 2.3.4 Disturbance Estimates . . . . . 16
  - 2.3.5 Definition of Nominal Conditions . . . . . 16

2.3.5.1 Simplified Simulator . . . . . . . . . . . . . . . . . . . . . 16
2.3.5.2 End to End Simulator . . . . . . . . . . . . . . . . . . . . 16

**3 Design and Analysis of Linear Control Methods 18**
3.1 PID Controller . . . . . . . . . . . . . . . . . . . . . . . . . . . . . 18
3.1.1 Unfiltered PID Controller . . . . . . . . . . . . . . . . . . . . 22
3.1.2 Filtered PID Controller . . . . . . . . . . . . . . . . . . . . . 23
3.2 State Space Controller . . . . . . . . . . . . . . . . . . . . . . . . . 29
3.2.1 Addition of an Integrator . . . . . . . . . . . . . . . . . . . . 30
3.2.2 Pre-Compensation . . . . . . . . . . . . . . . . . . . . . . . . 32
3.2.3 Choice of State-Space Control Law . . . . . . . . . . . . . . . 33
3.2.4 State Estimator Design . . . . . . . . . . . . . . . . . . . . . 33
3.2.4.1 Reduced State Observer Design . . . . . . . . . . . . . . 35
3.2.4.2 Kalman Filter Design . . . . . . . . . . . . . . . . . . . . 36
3.2.4.3 Choice of State Estimator . . . . . . . . . . . . . . . . . . 36
3.2.5 Complete State Space Controller . . . . . . . . . . . . . . . . 37
3.3 Best Linear Controller . . . . . . . . . . . . . . . . . . . . . . . . . 37

**4 Design and Analysis of Nonlinear Control Methods 41**
4.1 Motivation and Strategy . . . . . . . . . . . . . . . . . . . . . . . . 41
4.2 Development of Maximum Force Actuation Algorithm . . . . . . . . . . . 42
4.2.1 Concept of Maximum Force Actuation Algorithm . . . . . . . . . . 43
4.2.2 Torque Limitation . . . . . . . . . . . . . . . . . . . . . . . . 44
4.3 Design of Nonlinear Controller . . . . . . . . . . . . . . . . . . . . . 45

**5 Comparison of Best Linear versus Nonlinear Control Strategy 47**
5.1 Performance Comparison . . . . . . . . . . . . . . . . . . . . . . . . 47
5.1.1 Testing of the LPF Requirements Release Conditions . . . . . . . . 47
5.1.2 Velocity Limit Testing . . . . . . . . . . . . . . . . . . . . . . 50
5.2 Evaluation of Ideal Performance . . . . . . . . . . . . . . . . . . . . 53
5.2.1 Controller Performance Indices . . . . . . . . . . . . . . . . . . 54

**6 Overall Control Strategy 57**
6.1 Description of Strategy and Justification . . . . . . . . . . . . . . . . 57
6.1.1 Strategy . . . . . . . . . . . . . . . . . . . . . . . . . . . . . 57
6.1.2 Justification of Strategy . . . . . . . . . . . . . . . . . . . . . 58
6.2 Verification . . . . . . . . . . . . . . . . . . . . . . . . . . . . . . 58
6.2.1 Nominal Run . . . . . . . . . . . . . . . . . . . . . . . . . . . 59
6.2.1.1 Displacements and Attitudes . . . . . . . . . . . . . . . . 59
6.2.1.2 Velocities and Rates . . . . . . . . . . . . . . . . . . . . . 61
6.2.1.3 Forces and Torques . . . . . . . . . . . . . . . . . . . . . 63
6.2.2 Breaking Velocity Limit - Worst Case . . . . . . . . . . . . . . . 65
6.2.3 Breaking Velocity Limit - Realistic Case . . . . . . . . . . . . . . 69
6.2.4 Test Mass Charge Limit . . . . . . . . . . . . . . . . . . . . . 71
6.3 Operational Limits of Investigated Control Strategies . . . . . . . . . . 75

**7 Conclusions 76**

**8 Outlook** **78**

**A System Model Features** **80**
A.1 Test Mass Dynamics . . . . . . . . . . . . . . . . . . . . . . . . . . . 80
A.2 Adopted Model Limits . . . . . . . . . . . . . . . . . . . . . . . . . . 84

**B PID Controller Gains Derivation** **86**

**C State Estimators Design** **89**
C.1 Reduced State Observer . . . . . . . . . . . . . . . . . . . . . . . . . 89
C.2 Kalman Filter Design . . . . . . . . . . . . . . . . . . . . . . . . . . 91
C.2.1 Final Filter Equations . . . . . . . . . . . . . . . . . . . . . . . 93
C.2.2 Implementation Remarks . . . . . . . . . . . . . . . . . . . . . 94
C.2.3 Weight Matrices Derivation . . . . . . . . . . . . . . . . . . . . 95
C.2.4 Derivation of the Q Matrix . . . . . . . . . . . . . . . . . . . . 96
C.2.4.1 Assessment of Noise Uncertainty . . . . . . . . . . . . . . 97
C.2.4.2 Assessment of Command Error Uncertainty . . . . . . . . 98
C.2.4.3 Final Q Matrices . . . . . . . . . . . . . . . . . . . . . . . 99
C.2.5 Derivation of the R matrix . . . . . . . . . . . . . . . . . . . . . 99
C.2.5.1 Assessment of Noise Uncertainty . . . . . . . . . . . . . . 100
C.2.5.2 Assessment of Measurement Error Uncertainty . . . . . . 101
C.2.5.3 Final R Matrices . . . . . . . . . . . . . . . . . . . . . . . 101
C.3 Estimator Selection . . . . . . . . . . . . . . . . . . . . . . . . . . . 102
C.3.1 Test mass position and attitude estimates . . . . . . . . . . . . 103
C.3.2 Test mass velocity and rate estimates . . . . . . . . . . . . . . 104
C.3.3 Test mass velocity and rate estimate errors . . . . . . . . . . . 105
C.3.4 Disturbance forces and torques estimates . . . . . . . . . . . . 106
C.3.5 Disturbance forces and torques estimates errors . . . . . . . . . 107

**D Maximum Force Actuation Algorithm** **109**
D.1 Derivation of Maximum Force Actuation Algorithm . . . . . . . . . . 109
D.2 Evaluation of Minimum Torque Limit . . . . . . . . . . . . . . . . . 114
D.3 Maximum Force Command Calculation for Estimator Input . . . . . . 117

**Bibliography** **121**

# List of Figures


1.1 LISA mission . . . 3
1.2 Artist's impression of the LTP ©ESA . . . 3
1.3 Artist's impression of the LISA Pathfinder spacecraft ©ESA . . . 3
1.4 Artist's impression of one of the three LISA spacecraft ©Airbus Defence and Space . . . 4
1.5 Schematic of one year orbit of the LISA spacecraft formation ©ESA . . . 4

2.1 Test mass release plungers schematic . . . 10
2.2 IS electrodes . . . 11
2.3 IS capacitances . . . 12
2.4 Positive $x$ force generation . . . 13
2.5 Positive $\phi$ torque generation . . . 13
2.6 Force distance . . . 14
2.7 Positive $x$ force generation . . . 14
2.8 Positive $\phi$ torque generation . . . 14

3.1 PID controller, $z$ Bode plots . . . 20
3.2 PID controller, $z$ margins . . . 20
3.3 PID controller, $\eta$ Bode plots . . . 21
3.4 PID controller, $\eta$ performance . . . 22
3.5 PID controller, $\eta$ torque control signal . . . 23
3.6 System block diagram with filter . . . 23
3.7 Filtered PID controller, $z$ Bode plots . . . 25
3.8 Filtered PID controller, $\eta$ Bode plots . . . 26
3.9 Lowpass Filter Step Response . . . 27
3.10 Filtered/Unfiltered PID Torque Command Comparison . . . 28
3.11 Filtered/Unfiltered PID $\eta$ Dynamics Comparison . . . 28
3.12 System block diagram with integrator . . . 30
3.13 Compensation strategies, displacements . . . 34
3.14 Compensation strategies, command . . . 34
3.15 PID vs LQG comparison, Test Mass position . . . 39
3.16 PID vs LQG comparison, force control signal . . . 39
3.17 PID vs LQG comparison, test mass attitude . . . 40
3.18 PID vs LQG comparison, torque control signal . . . 40

4.1 Nonlinear force control switching logic . . . 46
4.2 Nonlinear torque control switching logic . . . 46

5.1 Controllers comparison: $z$ coordinate performance . . . 48

5.2 Controllers comparison: force control signal . . . 48
5.3 Controllers comparison: $\eta$ coordinate performance . . . 49
5.4 Controllers comparison: torque control signal . . . 49
5.5 Displacements for LQG velocity limit tests . . . 51
5.6 Force command for LQG velocity limit tests . . . 52
5.7 Displacements for VGS velocity limit tests . . . 52
5.8 Force command for VGS velocity limit tests . . . 53
5.9 Maximum tolerable release velocity versus maximum displacement limit . 55

6.1 Sliding Mode Controller nominal run Displacements . . . 59
6.2 Sliding Mode Controller nominal run Angles . . . 60
6.3 Switching Controller nominal run Displacements . . . 60
6.4 Switching Controller nominal run Angles . . . 61
6.5 Sliding Mode Controller nominal run Velocities . . . 61
6.6 Sliding Mode Controller nominal run Rates . . . 62
6.7 Switching Controller nominal run Velocities . . . 62
6.8 Switching Controller nominal run Rates . . . 63
6.9 Sliding Mode Controller nominal run Forces . . . 63
6.10 Sliding Mode Controller nominal run Torques . . . 64
6.11 Switching Controller nominal run Forces . . . 64
6.12 Switching Controller nominal run Torques . . . 65
6.13 Worst Case release velocity limit, displacements . . . 66
6.14 Worst Case release velocity limit, velocities . . . 67
6.15 Worst Case release velocity limit, forces . . . 68
6.16 Realistic Case release velocity limit, displacements . . . 70
6.17 Realistic Case release velocity limit, velocities . . . 70
6.18 Realistic Case release velocity limit, forces . . . 71
6.19 Test Mass charge limit, displacements . . . 73
6.20 Test Mass charge limit, velocities . . . 73
6.21 Test mass charge limit, forces . . . 74
6.22 Test mass charge limit, forces, particular . . . 74

A.1 Reference systems . . . 81
A.2 $6^{th}$ order forces showing model validity limits . . . 85

C.1 Timeline for a priori and a posteriori estimates and error covariances [1] . 92
C.2 Magnitude Bode plot for the actuation noise shape filter . . . 97
C.3 Magnitude Bode plot for the sensing noise shape filter . . . 100
C.4 z displacement, KF estimate . . . 103
C.5 $\eta$ angle, KF estimate . . . 103
C.6 KF and Observer velocity estimates . . . 104
C.7 KF and Observer rate estimates . . . 104
C.8 KF and Observer velocity estimates error . . . 105
C.9 KF and Observer rate estimates error . . . 105
C.10 KF and Observer DC force estimates . . . 106
C.11 KF and Observer DC torque estimates . . . 106
C.12 KF and Observer DC force estimates errors . . . 107
C.13 KF and Observer DC torque estimates errors . . . 107

D.1 Generated forces for complete and linearized maximum force actuation algorithm implementations . . . 112
D.2 Generated torques for complete and linearized maximum force actuation algorithm implementations, positive z displacement . . . 112
D.3 Generated torques for complete and linearized maximum force actuation algorithm implementations, negative z displacement . . . 113
D.4 Schematic diagram of the maximum force actuation algorithm logic . . . 114
D.5 Minimum required torque for 10 mrad maximum overshoot . . . 116
D.6 Minimum required torque for 0.1 mrad/s release rate . . . 117
D.7 Comparison of computed force for $1^{st}$ and $6^{th}$ order capacitance model . . . 118
D.8 Composition of corrected force output . . . 118
D.9 Adopted force calculation output . . . 120

# List of Tables


2.1 Test Mass initial conditions after release . . . . . 15
2.2 Test Mass control accuracy requirements . . . . . 15
2.3 Disturbance estimates, linear and angular accelerations . . . . . 16
2.4 Disturbance estimates, forces and torques . . . . . 16
2.5 Nominal Release Conditions for Simplified Simulator . . . . . 16
2.6 Nominal Release Conditions for End to End Simulator . . . . . 17

3.1 PID controller, $\eta$ margins . . . . . 21
3.2 Filtered PID controller, $z$ margins . . . . . 25
3.3 Filtered PID controller, $\eta$ margins . . . . . 26

A.1 $6^{th}$ order model displacement limits . . . . . 84

C.1 Process noise variances . . . . . 98
C.2 Command error variances . . . . . 99
C.3 Final Q matrix variances values . . . . . 99
C.4 Measurement noise variances . . . . . 100
C.5 Measurement error variances . . . . . 101
C.6 Final R matrix variances . . . . . 102
C.7 Command Errors against Disturbances Comparison . . . . . 108

D.1 Resulting values for force threshold . . . . . 119

# Preface

This thesis has been performed at Airbus Defence and Space (former Astrium GmbH) in Friedrichshafen, Germany.
It has been performed under the supervision of Dipl.-Ing. Tobias Ziegler and Dipl.-Ing. Nico Brandt, with the collaboration of Dipl.-Ing. Alexander Schleicher.

# Chapter 1

# Introduction

After the LISA spacecraft have reached their target orbit, before science operations can begin, the test masses they carry have to be released from their launch lock, and caught using electrostatic actuation. The successful catching of the Test Mass after release is essential for the mission. During the development and implementation of the LISA Pathfinder mission, it has been recognized that the test mass release from the launch lock is still critical. For this reason, improvements in hardware, capacitive actuation algorithm and control law are desirable.

This master thesis work focuses on the development of a control strategy and algorithm design with the goal to achieve the best possible catching performances, for the existing hardware constraints.

After some background on the LISA missions is given, a recap of the work on which the present control strategy has been designed is presented. Finally, the motivation to improve the existing design is explained, and the contributions of this thesis are presented.

## 1.1 The LISA Experiment

The Evolved Laser Interferometer Space Antenna (eLISA) is a proposed space mission concept designed to detect and measure gravitational waves, whose existence was predicted by Einstein within the frame of his General Relativity Theory.

eLISA will be the first space-based gravitational wave detector. The need for a space detector arises from the fact that the strongest expected gravitational waves (the ones originating from massive black holes and star binaries) are predicted to have frequencies

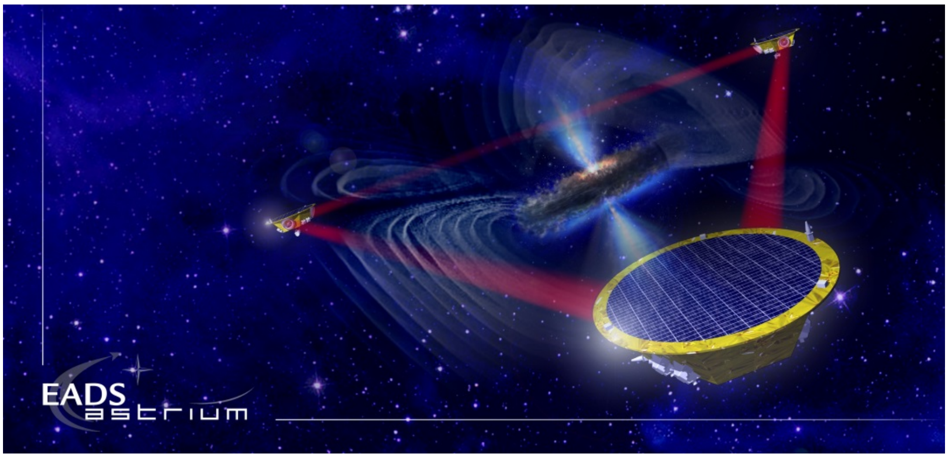


FIGURE 1.1: Artist's impression of the three LISA spacecraft ©Airbus Defence and Space

in the $10^{-4}$ to $10^{-1}$ Hz range, and generate a strain (the fraction of stretching or squeezing of the space they travel into) expected to be $h \cong 10^{-20}$ when passing through the Earth. The combination these two factors makes them essentially impossible to measure in ground facilities, due to all sorts of ground-related disturbances.

However, the realization of such an ambitious mission requires the use of various new technologies never built and tested before, some of which cannot at all be tested on ground. An entire mission, LISA Pathfinder, has been developed for this reason, as a technology demonstrator and testing platform for the eLISA critical systems.

### 1.1.1 The LISA Pathfinder

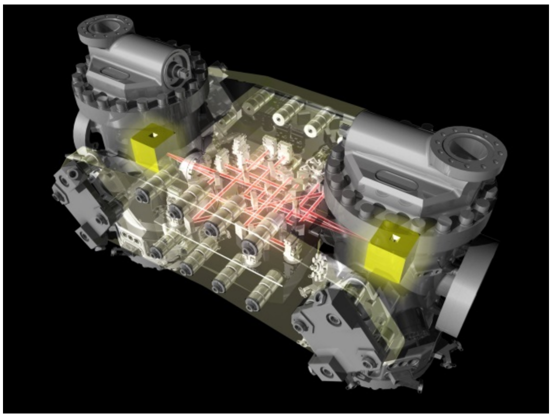

FIGURE 1.2: Artist's impression of the LTP ©ESA

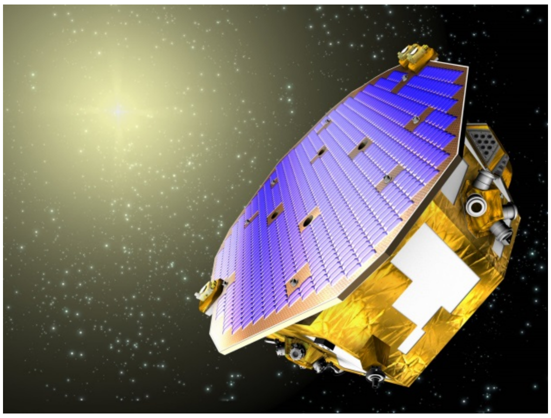

FIGURE 1.3: Artist's impression of the LISA Pathfinder spacecraft ©ESA

LISA Pathfinder mimics one arm of the LISA constellation, reducing its length from 5 million kilometres to 38 centimetres, while still keeping all the technology necessary for the actual mission. It will be launched in a Lissajous orbit around the Earth-Sun L1 point, and it will stay there for a science operations nominal lifetime of 180 days. The core payload is the LISA Technology Package (LTP) built by Astrium with the collaboration of several European institutes and companies. The payload contains essentially all the technology required for the gravitational wave detection, as carried out by LISA.

The implementation of the LISA Pathfinder spacecraft is now in its final phases, with the launch being scheduled for 2015.

### 1.1.2 The eLISA Mission

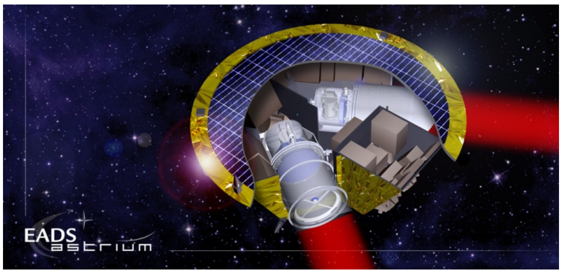


FIGURE 1.4: Artist's impression of one of the three LISA spacecraft ©Airbus Defence and Space

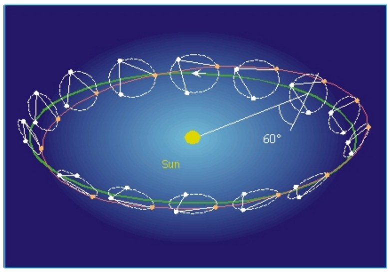


FIGURE 1.5: Schematic of one year orbit of the LISA spacecraft formation ©ESA

The eLISA mission will consist of a formation of three spacecraft, flying at the vertices of a 5 million kilometres arm equilateral triangle, while following a heliocentric orbit.

It will directly measure gravitational waves by means of laser interferometry, measuring variations of the optical path length between different spacecraft. Each one will carry two Inertial Sensors, each including one free falling test mass which acts as a mirror for the laser.

Through the use of suitably designed optical benches, Michelson-like interferometers are formed, that allow measuring very small changes in optical path length, which in turn correspond to very small changes of the relative distance between test masses 5 million kilometres apart from each other.

The program was chosen as the L3 mission within the ESA Cosmic Vision Program, with a tentative launch date in 2034.

## 1.2 Previous Work

All the work that has been done to improve the TM capturing performances took as a starting point the established experience and work done for the LISA Pathfinder mission. The past contributions that were most involved in the process, the baselines that have been either expanded or substituted, are now presented and briefly described.

### 1.2.1 The LISA Pathfinder Capacitive Actuation Algorithm

The Capacitive Actuation Algorithm [2] is a piece of software that converts the commanded forces and torques to be applied to the test mass, to voltages to be applied to the housing electrodes (see figure 2.2). Such a conversion is not trivial because of the position-dependent pull that is produced on the test mass by an electrode, when a given voltage is applied. Moreover, saturation of the housing electrodes should always be avoided.

The LISA Pathfinder actuation algorithm [2] is based on a Taylor expansion of order 0 of the Inertial Sensor capacitance model [3]. For this reason, the applied voltages result in a "correct" (as-commanded) force only when the test mass is in its nominal position, and the errors quickly grow as the displacements increase. For a 1mm displacement, the actuated force is as low as 50% of the commanded one. Moreover, forces and torques have to be applied separately, introducing a duty cycle in the actuation that effectively halves the maximum obtainable forces and torques. As an additional consequence, during the force half-cycle, some cross-coupling torque is produced, and during the torque half-cycle, some cross-coupling force is produced, introducing further errors in the system.

### 1.2.2 The LISA Pathfinder Accelerometer Mode Controller

Due to the errors introduced by the Capacitive Actuation Algorithm, the design of the LISA Pathfinder Accelerometer Mode controller (the one dealing with TM catching after release) has been dominated by the need to be robust against system uncertainties. For this reason, several controller designs have been investigated in the past, both by Astrium [4] and ESA [5] with the selected one being a Sliding Mode controller. The Sliding control provides a systematic approach to the problem of maintaining stability and consistent performance in the face of modelling imprecision [6].

The main disadvantage of the Sliding Mode controller is that its design is still based on a priori calculation of the minimum expected actuation gain. For the LISA Pathfinder controller, this value has been computed as the ratio of the commanded force or torque versus the maximum possible actuation force/torque for the worst case displacement, considering also cross coupling effects. This means that, while the actuator will never saturate, it will only exploit its full capabilities when the worst case conditions occur. The maximum possible actuation authority is not always exploited.

### 1.2.3 The Improved Capacitive Actuation Algorithm

In the scope of improving TM catching performances, a new Capacitive Actuation Algorithm has been developed by Airbus Defence and Space and is presented in [7]. This new algorithm is based on a first order Taylor expansion of the Inertial Sensor capacitance model, therefore including informations on the test mass position and attitude in the voltage calculation. The performances of this new algorithm are greatly improved with respect to the original one [2]. The errors between commanded and actuated forces and torques are essentially negligible for test mass displacements and attitudes of about 1mm and 10mrads respectively. The need for a duty cycle is removed, and the voltage application has been changed from alternate to continuous, effectively doubling the maximum obtainable forces and torques. This actuation algorithm has been used as the starting point for the development of the work presented in the thesis.

## 1.3 Motivation

Since it is of fundamental importance to properly catch the test mass using electrostatic actuation, there is great interest in finding out the best possible way of accomplishing such a task.

It also must be done within the given electronics hardware constraints, which represent the state-of-the-art technology to provide voltages to the electrodes of the inertial sensor. Using a higher electrode voltage would benefit operations by increasing the available maximum force. However, three main components of the electronic setup are limiting such an increase:

- The output transistors are required to have a breakdown voltage double the electrode one (they operate between + and -). An additional margin of 2 is then taken and as a result, no space qualified parts are now available that allow an increase of the electrode voltages.
- The coaxial cable is also required to operate at the transistor breakdown voltage (300 V) with a margin of 2. Most space qualified coaxial cables are now 600 V.

- Actuation and sensing capacitors also have to operate at twice the operation voltage. Right now the limit in capacitor voltage is 250 V and since their quality plays a very important role in the operations, the use of higher voltage ones with worse performance is a problem.

Therefore the focus of this work will be on the definition of a control law that exploits the existing hardware to its maximum possibilities: that means to stop the test mass using all the force generated with the voltage amplitudes as provided by the currently available Inertial Sensor electronics.

In the evaluation phase of the various designs, it should be clear where value is placed, what the "best" controller should do better than the others. The clearly most important figure of merit, given the premises, is the maximum overshoot.

There are several reasons for this: first of all, since the top-level goal is avoiding the test mass from touching the housing, the smaller its displacement is, the better. Second, since the electrodes can only pull, and their pull becomes weaker as the TM displacement grows, it becomes more likely that the electrostatic force will not be sufficient to stop it. Last, the inertial sensor capacitance model used in the non-linear simulation environment for closed-loop verification is only an approximation, and the greater the TM displacements grow, the greater the errors between reality and model will be, such that it becomes unphysical for displacements bigger than 2 mm for x, 1.4 mm for y and 1.7 mm for z.

## 1.4 Thesis Contributions

The focus of this thesis is on the research of the control law that "best" performs in terms of TM catching, within the existing hardware constraints.

In the scope of this, the limits of linear control have been explored, by developing and comparing different designs: a simple position feedback PID controller, followed by a full-state feedback controller. A reduced state observer and a Kalman filter have been developed and compared to be used as state estimators for the state-space controller. The best performing linear controller has been identified.

The idea of exploiting the maximum hardware capabilities of the system has then been elaborated and a suitable nonlinear control law has been introduced.

The nonlinear control law always commands the maximum possible force to counteract the TM velocity. As a matter of fact, it is a bang-bang velocity controller whose output is not a fixed command value with positive or negative sign, but always request the “maximum possible force” of given sign for current test mass position, and torque command.

Since the “maximum possible force” has a position-dependent value, the Capacitive Actuation Algorithm [7] has been modified. The possibility to ask for a generic “maximum command” with a certain sign has been included, producing a voltage command that maximizes the actuated force based on test mass position and torque command. The addition of this particular feature allows to avoid any a priori and conservative evaluation of the maximum force that can be asked for, allowing the bang-bang controller to effectively exploit the hardware to its limits, but not to exceed them.

Having the most effective velocity breaking control strategy (nonlinear switching, controller with position and attitude dependent gain), a complete control strategy has been proposed: after successfully breaking the test mass velocity with the nonlinear controller, the test mass control law is switched to a linear controller, which then takes it back to the nominal position.

An investigation of the highest TM release velocity that can be tolerated has then been carried out, by running simulations with the best linear controller, and the nonlinear one. The resulting values have been compared to the result of a simplified model, to establish a performance parameter of the controllers.

Finally, the best performing controller has been implemented in the nonlinear LISA Pathfinder End-to-End simulator, and its behaviour for various test cases has been investigated.

# Chapter 2

# System Description

In this chapter, a mathematical description of the system to be controlled will be carried out. First, the equations of motion for the TM inside its housing are derived by considering the relative motion between TM and spacecraft, when both are affected by gravity, disturbance and control forces. Then, an overview of the adopted electrostatic actuation scheme is presented, explaining its main principles and limits. Finally, the LISA Pathfinder Accelerometer Mode controller requirements are listed, because they define the scenario in which the controller will have to operate.

## 2.1 Test Mass Dynamics

A full derivation of the test mass–spacecraft relative motion dynamics can be found in the Appendix A.1. Only the final results are reported here, as they constitute the model used in the controller design.

The equation for the test mass x degree of freedom writes:

$$\begin{aligned}\ddot{x}_1 = -\Omega_{11}^2 x_1 - u_{T\,x_{SC}} - d_{SC\,x_{SC}} + z_1(u_{T\,\theta_{SC}} + d_{SC\,\theta_{SC}}) \\ - y_1(u_{T\,\varphi_{SC}} + d_{SC\,\varphi_{SC}}) + u_{ES\,x_1} + d_{TM\,x_1}\end{aligned} \tag{2.1}$$

Where:

- $x_1$, $y_1$, $z_1$ are the test mass-spacecraft relative coordinates
- $\Omega_{11}^2$ is the test mass external stiffness

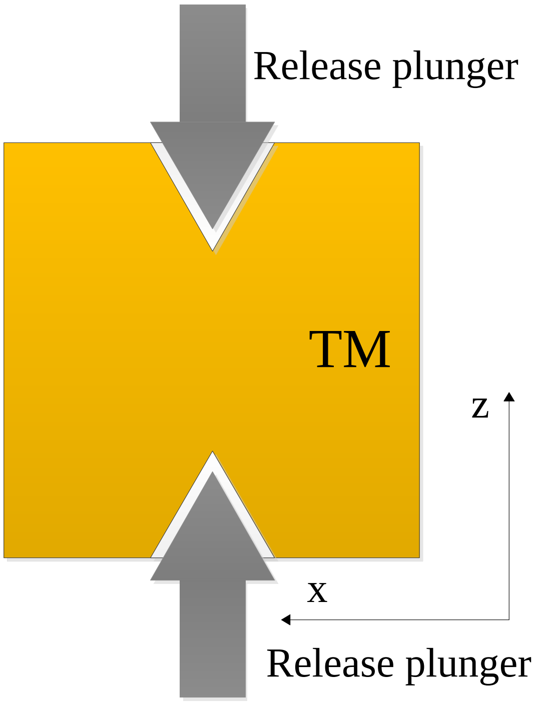


FIGURE 2.1: Test mass release plungers schematic

- $u_{Tq}$ is the thruster force along the q coordinate direction
- $d_{SCq}$ is the external disturbance force acting on the spacecraft along the q coordinate direction
- $u_{ESq}$ is the electrostatic actuation force along the q coordinate direction

If the external disturbances on the spacecraft are assumed to be compensated using thruster action, to a level where they are negligible with respect to TM external disturbances, the equation becomes:

$$\ddot{x} = -\Omega_{11}^2 x + u_{ESx} + d_{TMx} \tag{2.2}$$

This shape of the equation of motion simply expresses the dynamics of a forced spring.

### 2.1.1 Release Direction

The test mass release mechanism is positioned inside the inertial sensor such that the mechanical plungers which retain it in place retract along the z direction (see figure 2.1). Due to this reason, the most critical degree of freedom for the test mass catching phase is z. Along this axis the highest release velocities and displacements are expected, and the actuating electrodes are smallest (due to the area occupied by plunger holes).

## 2.2 Electrostatic Actuation

The inertial sensor houses a total of 18 electrodes, 12 of which are responsible for the electrostatic actuation, while the remaining 6 are called "sensing" electrodes, and are used to bias the test mass so that electrostatic sensing can be carried out. Figure 2.2 shows a schematic of electrode layout and numbering, and the coordinate system adopted for all the work.

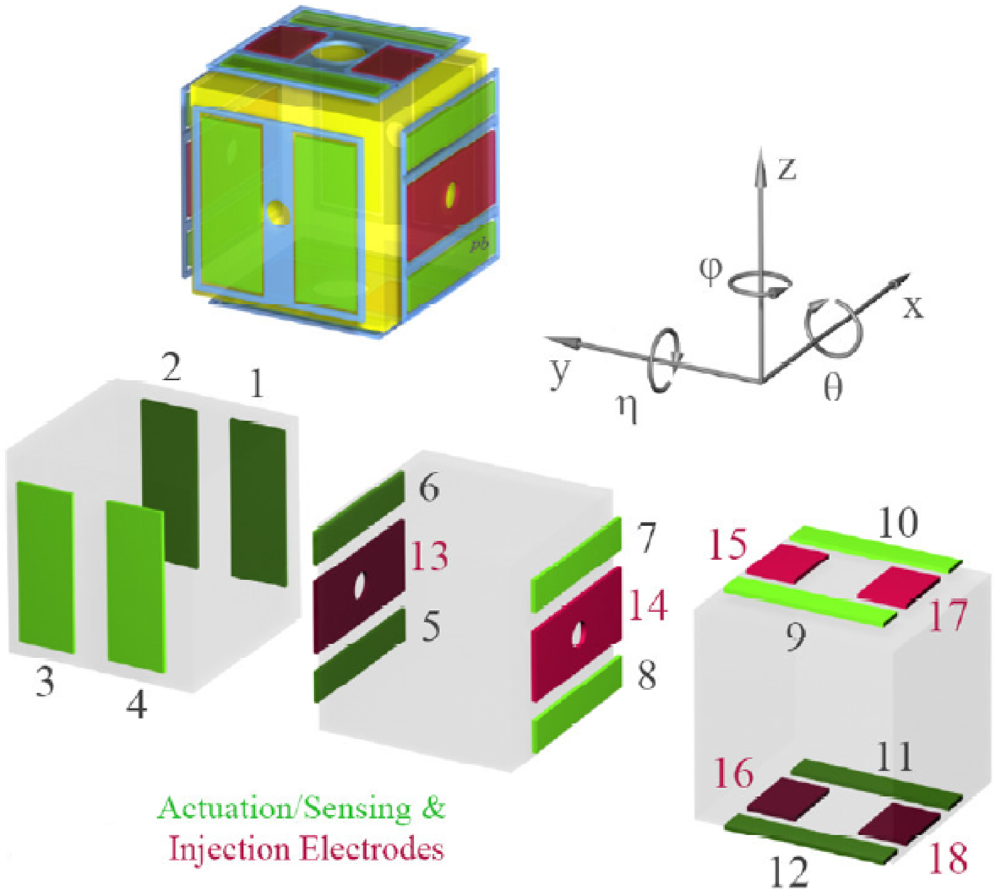


FIGURE 2.2: Inertial Sensor electrodes nomination and coordinates definition

### 2.2.1 Force Model

The actuation forces and torques on the test mass are obtained by applying voltages to the housing electrodes. The electrostatic system comprising electrodes, housing and test mass can be schematically represented as the network of capacitances and conductors depicted in figure 2.3.

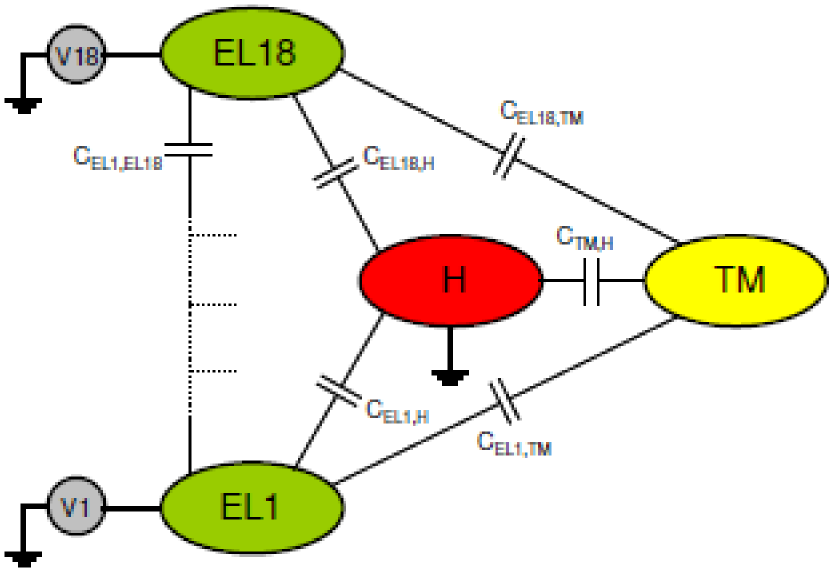


FIGURE 2.3: Schematic configuration of IS conductors and capacitances

The general form of the electrostatic force/torque equation can be derived by energetic considerations [3] and is given by:

$$F_q = \frac{1}{2}\sum_{i=1}^{18}\frac{\partial C_{EL_i,TM}}{\partial q}(V_i - V_{TM})^2 + \frac{\partial C_{EL_i,H}}{\partial q}V_i^2 + \frac{\partial C_{TM,H}}{\partial q}V_{TM}^2 \tag{2.3}$$

With the TM potential being given by:

$$V_{TM} = \frac{\sum_{i=1}^{18} C_{EL_i,TM}V_i}{C_{tot}} + \frac{Q_{TM}}{C_{tot}} \tag{2.4}$$

where $Q_{TM}$ stands for the test mass charge, and the total capacitance $C_{tot}$ can be expressed as:

$$C_{tot} = C_{TM,H} + \sum_{i=1}^{18} C_{EL_i,TM} \tag{2.5}$$

The notation $q$ stands for generalized coordinate, $V_i$ is the i-th electrode voltage (in principle also the sensing electrodes must be accounted for), $C_{EL_i,TM}$ the i-th electrode to TM capacitance, $C_{EL_i,H}$ the i-th electrode to housing capacitance, and $C_{TM,H}$ the test mass to housing capacitance.

In the following, it is assumed that the system will always operate using the Improved Actuation Algorithm. The simplifications introduced with this assumption make easier to understand the underlying principle and its limits.

In the Improved Actuation Algorithm, the 12 electrodes are separated in three sets of 4, each of which provides actuation along 2 TM coordinates. For example, electrodes 1 to 4 operate $x$ force and $\phi$ torque. This is a consequence of the fact that an electrode can only pull the test mass towards its surface. Therefore, to obtain a force along $x$, one will need to use electrodes whose surfaces are normal to the $x$ direction. At the same time, to rotate around $\phi$, one will need to use a suitable set of either $x$ or $y$ directed forces. Due to the Inertial Sensor arrangement, only $x$ electrodes have the layout required to produce a $\phi$ torque. Figures 2.4 and 2.5 illustrate the test mass, focusing on the $x/\phi$ electrodes layout. The separation of electrodes in different subsets is only possible if the test mass voltage is assumed to be zero [7]. The associated system of equation then is [7]:

$$F_x = \frac{1}{2}\sum_{i=1}^{4} a_i V_i^2 \tag{2.6}$$

$$F_\varphi = \frac{1}{2}\sum_{i=1}^{4} b_i V_i^2 \tag{2.7}$$

$$V_{TM} = \sum_{i=1}^{4} c_i V_i = 0 \tag{2.8}$$

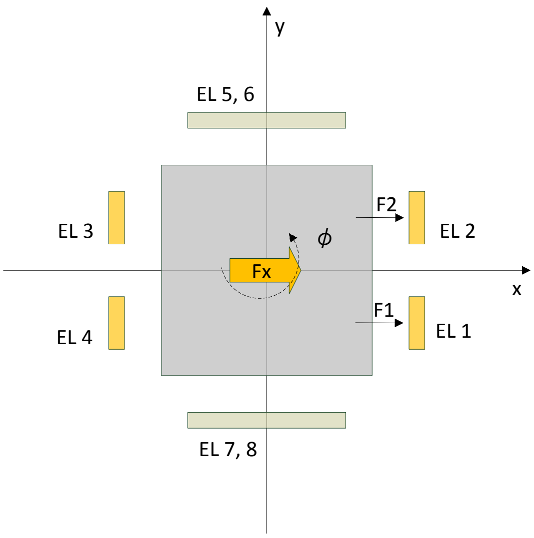


FIGURE 2.4: Positive $x$ force generation

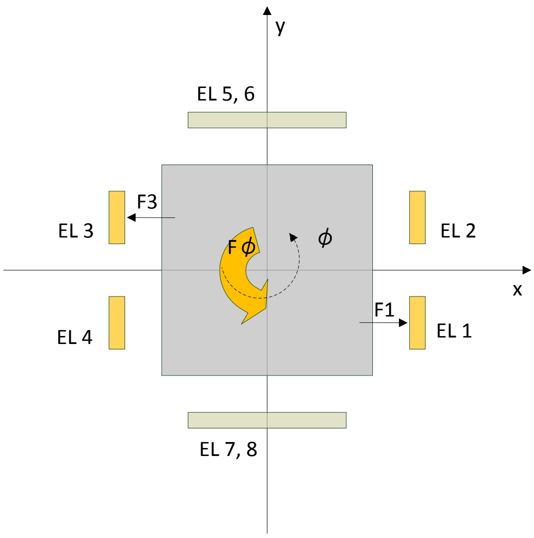


FIGURE 2.5: Positive $\phi$ torque generation

Another important characteristic of the electrostatic actuation is that, for a given electrode voltage, the pull exerted on the test mass decreases as the distance separating the electrode and test mass surfaces increases, as illustrated in figure 2.6.

A direct consequence of these two facts is that any restoring force (one that accelerates the test mass toward the nominal position) will always have to be generated by the least effective electrodes. For example, to counteract a positive x displacement, one should activate the electrodes 3 and 4, which for the same voltage generate a smaller force than electrodes 1 and 2. However, while electrodes 1 and 2 can generate a higher force,

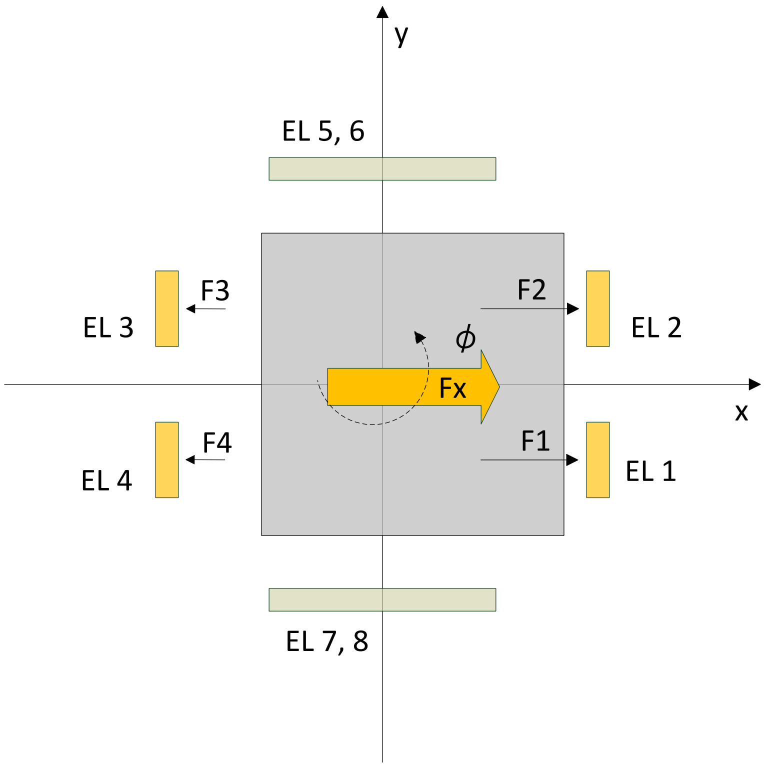


FIGURE 2.6: Electrodes pull dependence on TM displacement

they cannot generate one of the required sign (they cannot "push"). This concept is illustrated in figures 2.7 and 2.8 for force and torque respectively. The dashed arrows are shown to emphasize the concept that the electrodes which are not used could produce a greater force than the ones that must be used.

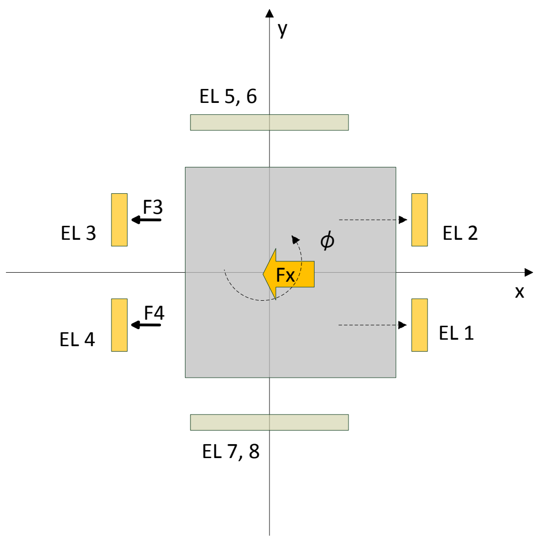


FIGURE 2.7: Positive $x$ force generation

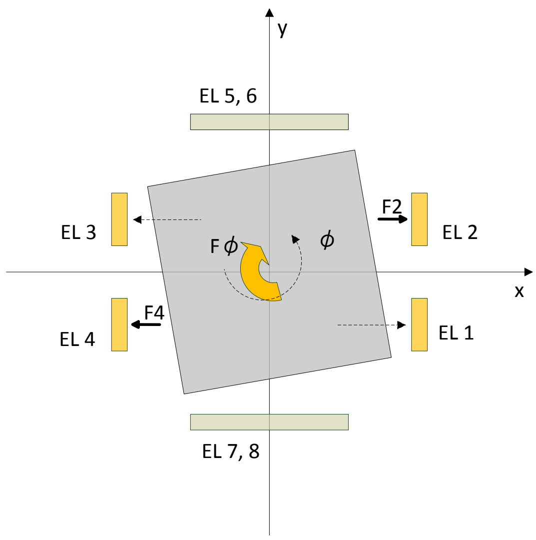


FIGURE 2.8: Positive $\phi$ torque generation

## 2.3 Summary of Operating Conditions

The whole problem of catching the test mass originates from the imperfection of the release mechanism. An ideal system would release the test mass in its nominal position, with zero velocity. A real system however cannot achieve perfect performance, and thus some requirements on the test mass position, attitude, residual linear and angular velocities after TM release into free flight have been defined. The task of catching the test mass after release essentially consists of removing the residual velocities and taking the mass back to a region close to the nominal position. The catching phase is completed when the TM states (position, attitude, velocities) are within specified steady state requirements.

The requirements specified for the LISA Pathfinder mission in [8] have been adopted as a baseline for the design process. They are listed in the following section.

### 2.3.1 Test Mass Initial States

| Test Mass State | Initial Value |
|---|---|
| Linear velocity, relative to test mass housing | $\pm 5 \cdot 10^{-6}$m/s |
| Rotational rate, relative to test mass housing | $\pm 1 \cdot 10^{-4}$rad/s |
| Displacement with respect to test mass housing | $\pm 200\mu$m |
| Attitude with respect to test mass housing | $\pm 2$mrad |

Table 2.1: Test Mass initial conditions after release

### 2.3.2 Maximum overshoots

- Maximum linear displacement overshoot: <1 mm;
- Maximum rotation overshoot: <10 mrad.

### 2.3.3 Control Accuracy (transition to steady state)

| Test Mass State | Control Accuracy |
|---|---|
| Linear velocity, relative to test mass housing | $< 1 \cdot 10^{-6}$m/s |
| Rotational rate, relative to test mass housing | $< 1 \cdot 10^{-5}$rad/s |
| Displacement with respect to test mass housing | $< 25\mu$m |
| Attitude with respect to test mass housing | $< 100\mu$rad |

Table 2.2: Test Mass control accuracy requirements

### 2.3.4 Disturbance Estimates

An estimate of the worst case external disturbances acting on the test mass (the $d_{TM_x}$) term in equation 2.2) has been carried out in [9]. The absolute values of the total disturbance forces for each degree of freedom, as derived in [9], are listed in tables 2.3 and 2.4, first as accelerations and then as forces and torques.

| Abs. value of max. disturbance forces (m/s$^2$) | | | Abs. value of max. disturbance torques(1/s$^2$) | | |
|---|---|---|---|---|---|
| $x$ | $y$ | $z$ | $\theta$ | $\eta$ | $\phi$ |
| $2.4 \cdot 10^{-8}$ | $4.3 \cdot 10^{-8}$ | $9.4 \cdot 10^{-8}$ | $3.3 \cdot 10^{-8}$ | $3.1 \cdot 10^{-8}$ | $2.4 \cdot 10^{-8}$ |

TABLE 2.3: Disturbance estimates, linear and angular accelerations

| Abs. value of max. disturbance forces (N) | | | Abs. value of max. disturbance torques(Nm) | | |
|---|---|---|---|---|---|
| $x$ | $y$ | $z$ | $\theta$ | $\eta$ | $\phi$ |
| $4.7 \cdot 10^{-8}$ | $8.4 \cdot 10^{-8}$ | $18.5 \cdot 10^{-8}$ | $22.6 \cdot 10^{-12}$ | $21.7 \cdot 10^{-12}$ | $16.3 \cdot 10^{-12}$ |

TABLE 2.4: Disturbance estimates, forces and torques

The force and torque values of the estimates have been calculated by multiplying their respective accelerations values by the mass (1.96 kg) for the forces, and by the moment of inertia ($6.912 \cdot 10^{-4}$ for all axis) for the torques.

### 2.3.5 Definition of Nominal Conditions

The nominal conditions for testing in the different simulator are defined.

#### 2.3.5.1 Simplified Simulator

The "nominal conditions" for testing in the simplified simulator are defined as in table 2.5.

| | Position | Attitude | Lin. Velocity | Rot. Velocity |
|---|---|---|---|---|
| TM1 | $+200\mu m$ | $+2mrad$ | $+5\mu m/s$ | $+100\mu rad/s$ |

TABLE 2.5: Nominal Release Conditions for Simplified Simulator

The applied disturbance forces are the ones defined in Table 2.3, always taken with a positive sign.

#### 2.3.5.2 End to End Simulator

The "nominal conditions" for testing in the nonlinear End to End Simulator are defined as in table 2.6:

| | Position | Attitude | Lin. Velocity | Rot. Velocity |
|---|---|---|---|---|
| TM1 | $+200\mu m$ | $-2mrad$ | $+5\mu m/s$ | $-100\mu rad/s$ |
| TM2 | $-200\mu m$ | $+2mrad$ | $-5\mu m/s$ | $+100\mu rad/s$ |

Table 2.6: Nominal Release Conditions for End to End Simulator

The disturbance forces are generated by the simulator models and are therefore not easily identified. The main one is the solar radiation pressure and for nominal conditions it is assumed as producing a $24\mu N$ force on the spacecraft, compensated by the thrusters with a 20% underestimation error (corresponding to a compensation of $19.2\mu N$).

# Chapter 3

# Design and Analysis of Linear Control Methods

In this chapter, the design of several linear control laws is presented, and their performances are compared to establish the "best" one. First, a simple PID design is illustrated, followed by two full state feedback controllers. A Kalman filter is then chosen as state estimator, its alternative being a reduced state observer whose performance is clearly inferior to the Kalman filter. Finally, a comparison between the PID controller and the best among the two state feedback controllers is carried out, and the state space controller implemented with a Kalman filter (resulting in an LQG) is accepted as our "best" linear controller.

## 3.1 PID Controller

As a starting point for the design and comparisons of linear controllers, a simple position feedback PID controller has been derived for each degree of freedom.

A PID controller is defined by its 3 gains: $K_P$, $K_D$ and $K_I$. In this work, the gains have been derived by using a technique tailored to the specific case. The gains are built such that a set fraction of the maximum actuation is used when facing worst case initial conditions. The idea behind the derivation is given here, for the full derivation refer to Appendix B.

The Laplace transform of the closed-loop controlled system free response (zero reference signal and nonzero initial conditions) is:

$$X(s) = \frac{s^2 x_0 + s\left(\dot{x}_0 + K_D x_0\right) + d}{s^3 + K_D s^2 + s\left(K_P + \Omega_{11}^2\right) + K_I} \tag{3.1}$$

The closed-loop controlled system has three poles, and the denominator can be written as the product of a real pole and a complex conjugate pair:

$$\left(s + {}^{1}\!/_{\tau}\right)\left(s^2 + 2\xi\omega_n s + \omega_n^2\right) \tag{3.2}$$

Where $\tau$ is the first order characteristic time, $\omega_n$ is the second order dynamics natural frequency and $\xi$ is its damping ratio. By expanding and comparing this to the former writing of the denominator, the gains can be written as:

$$K_D = {}^{1}\!/_{\tau} + 2\xi\omega_n \tag{3.3}$$

$$K_P + \Omega_{11}^2 = \frac{2\xi\omega_n}{\tau} + \omega_n^2 \tag{3.4}$$

$$K_I = \frac{\omega_n^2}{\tau} \tag{3.5}$$

The condition that the system must use a set fraction of the maximum available actuation when facing the worst case initial conditions writes:

$$u(0) = K_P x_0 + K_D \dot{x}_0 = u_c \tag{3.6}$$

Where $u_c$ is the chosen portion of total available actuation authority.

The system composed of the above equations can be solved for all the unknowns by making suitable assumptions on the required system dynamics.

This method, while being useful in terms of capture performance (due to the ability to choose the amount of command to use at a given initial condition) is lacking with respect to the classical bandwidth and gain/phase margins considerations, since the controller derivation is not based on such properties.

The resulting controllers for the various degrees of freedom have been calculated with the available data (e.g. external stiffnesses, maximum actuation authorities...) and resulted in good margins performances. The Bode plots and the minimum margins for the $z$ and $\eta$ controller are shown in figures 3.1 and 3.3, and tables 3.2 and 3.1.

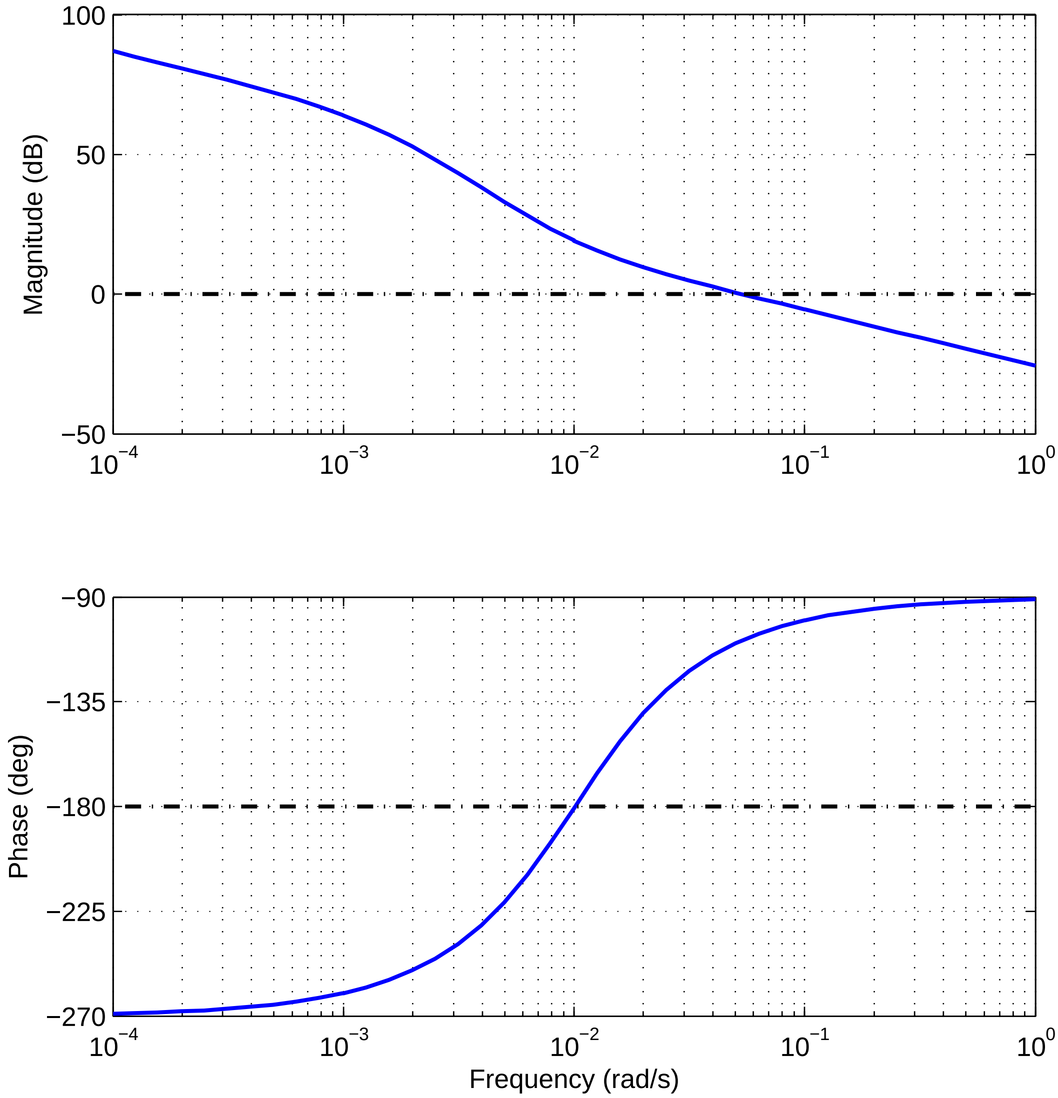


Figure 3.1: PID controller, $z$ Bode plots

| Gain margin [dB] | $\omega_c$ [rad/s] | Phase margin [deg] | $\omega_{180}$ [rad/sec] |
|---|---|---|---|
| -19.0 | 0.010 | 71 | 0.054 |

Figure 3.2: PID controller, $z$ margins

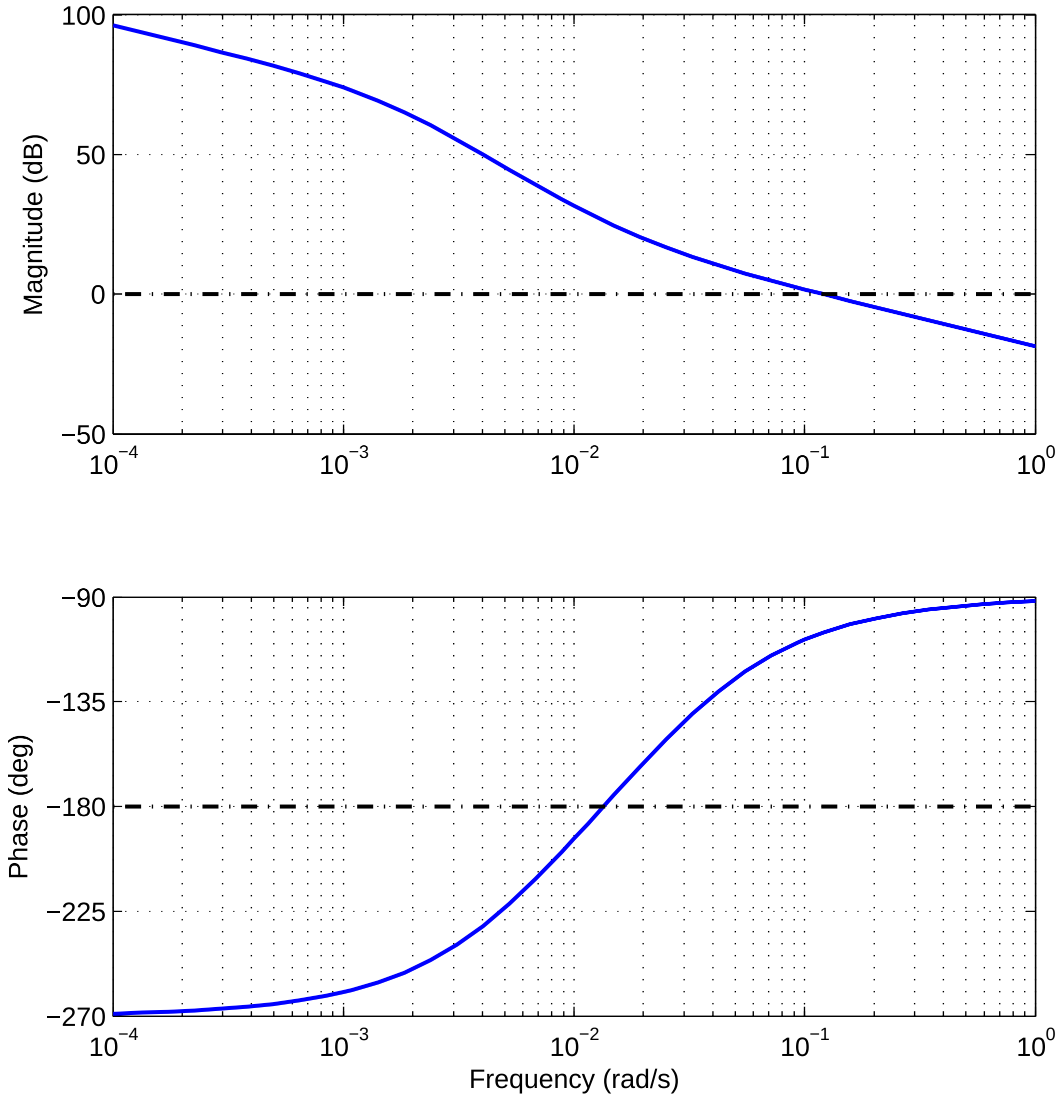


FIGURE 3.3: PID controller, $\eta$ Bode plots

| Gain margin [dB] | $\omega_c$ [rad/s] | Phase margin [deg] | $\omega_{180}$ [rad/sec] |
|---|---|---|---|
| -26.4 | 0.013 | 75 | 0.12 |

TABLE 3.1: PID controller, $\eta$ margins

While the derivations have been (and will continue to be) referred to the $x$ degree of freedom (mainly for a notation habit), all performances and controller characteristics such as margins will be done for the $z$ and $\eta$ degrees of freedom. Two axes are shown so the performances for both translational and rotational DoF controller can be examined. Among the various axes, the $z$ and $\eta$ ones are chosen because for the studied system, they happen to be the most critical couple.

### 3.1.1 Unfiltered PID Controller

The derived controller was tested, and showed very limited steady state performances. The problem originates from the derivative calculation of a noisy measured position signal, resulting in very high command noise, which for the rotational DoF prevents the controller from achieving the required steady state performances. Figure 3.4 shows the $\eta$ dof time history, and figure 3.5 shows the corresponding command signal.

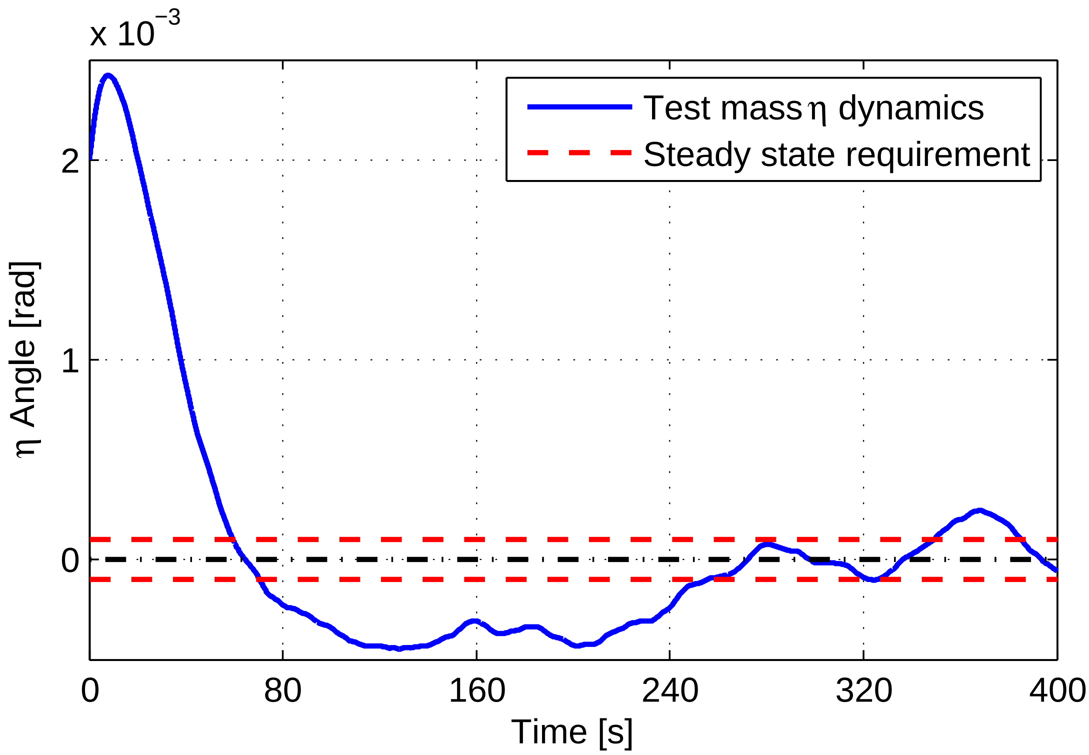


FIGURE 3.4: PID controller, $\eta$ performance

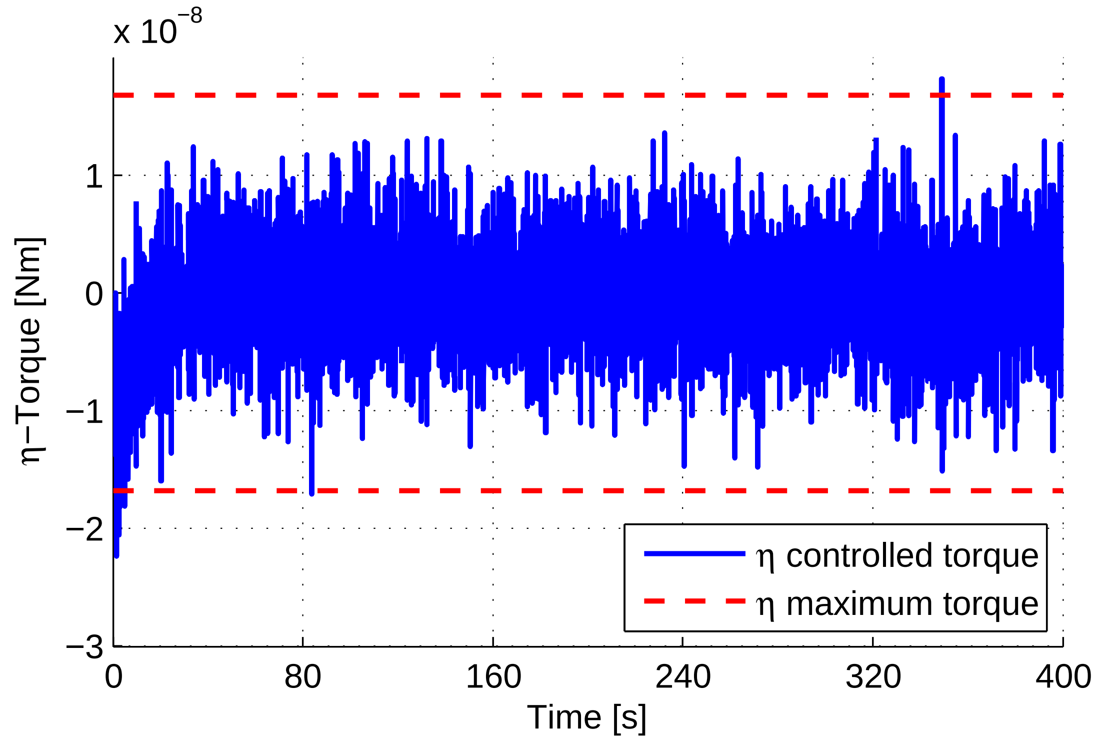


FIGURE 3.5: PID controller, $\eta$ torque control signal

### 3.1.2 Filtered PID Controller

To eliminate the problem of the noisy position signal, a low-pass filter has been added to the feedback loop. The new block diagram for the system is shown in figure 3.6

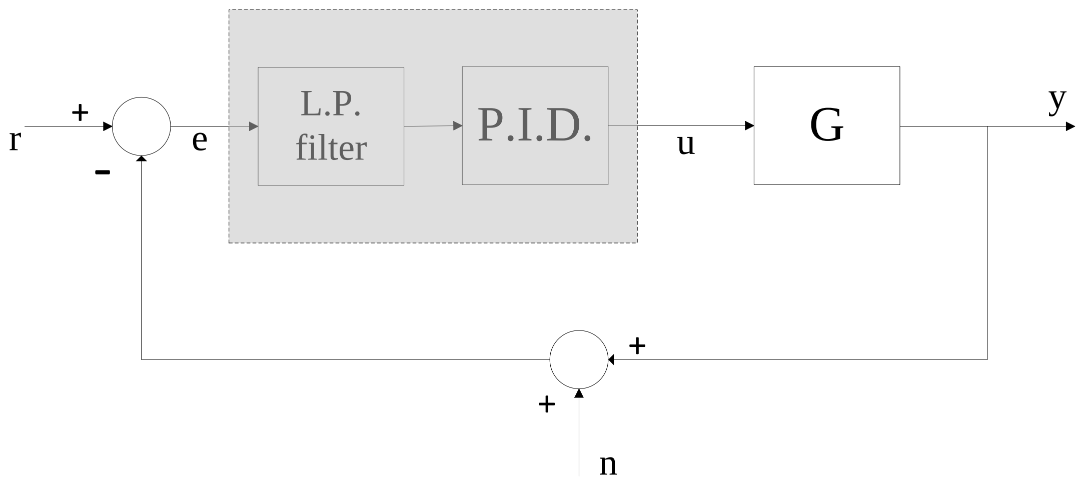


FIGURE 3.6: System block diagram with filter

The filter cutoff frequency is chosen such that the Bode diagrams of the open-loop system ($L = G \cdot K$) are left unchanged inside the controller bandwidth. For all degrees of freedom, the cutoff frequency has been chosen as 1 $rad/s$. The new Bode diagrams and the corresponding system margins, are shown in figures 3.7 and 3.8, and tables 3.2 and 3.3.

From figures 3.7 and 3.8 one can verify that inside the controller bandwidth the frequency response of the system is left unchanged. The stability margins as well are left essentially unchanged.

One drawback of the filter addition is that the overall system transfer function is modified (an additional pole is introduced), resulting in a mismatching between design and actual (simulated) maximum command fraction.

Simulation results show that the magnitude of the error is anyway not big enough to cause significant saturation issues. Even though the design command fraction is not obtained anymore, it still works as a guideline of what the real command signal will be. Decreasing the required command fraction also decreases the resulting command signal.

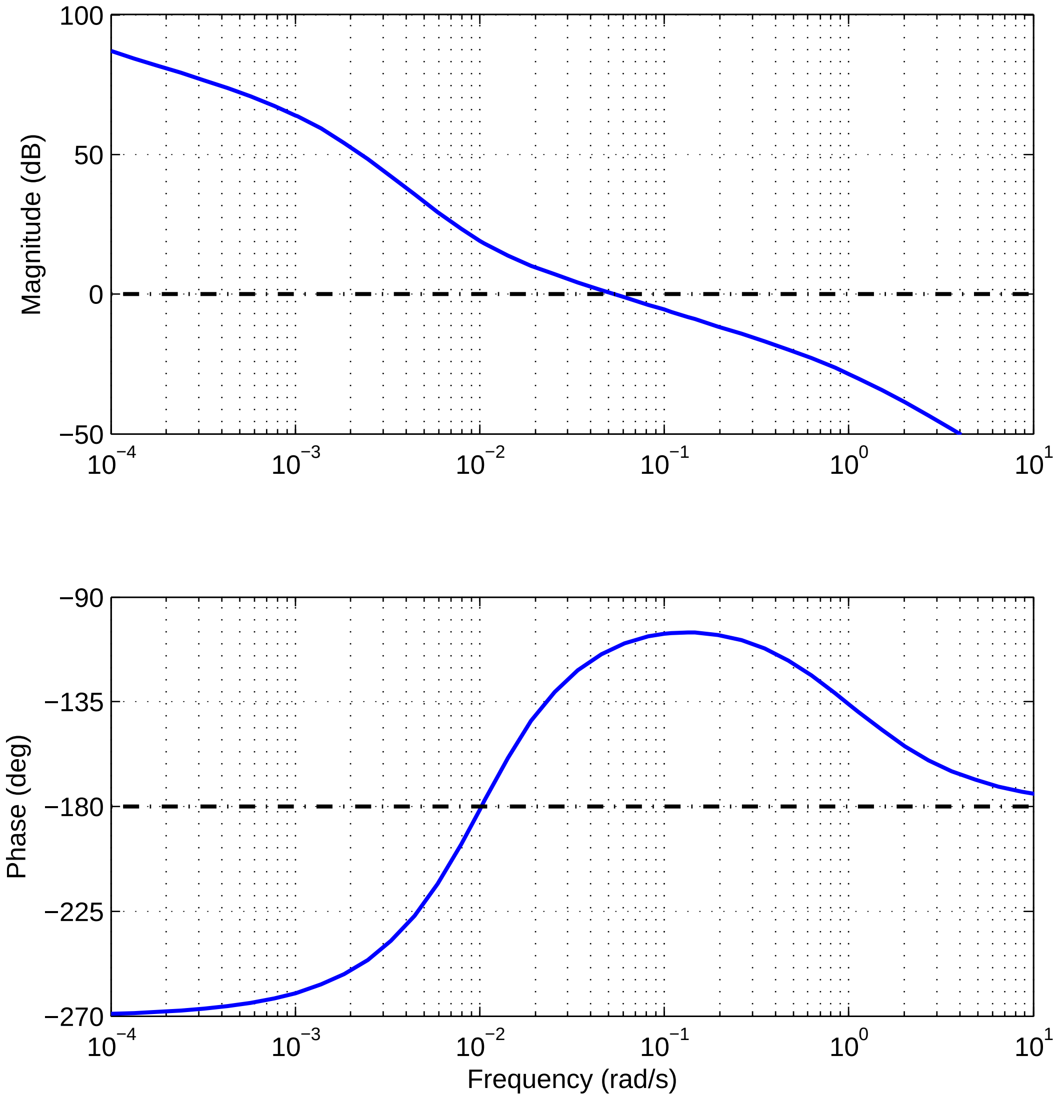


FIGURE 3.7: Filtered PID controller, $z$ Bode plots

| Gain margin [dB] | $\omega_c$ [rad/s] | Phase margin [deg] | $\omega_{180}$ [rad/sec] |
|---|---|---|---|
| -18.8 | 0.010 | 68 | 0.054 |

TABLE 3.2: Filtered PID controller, $z$ margins

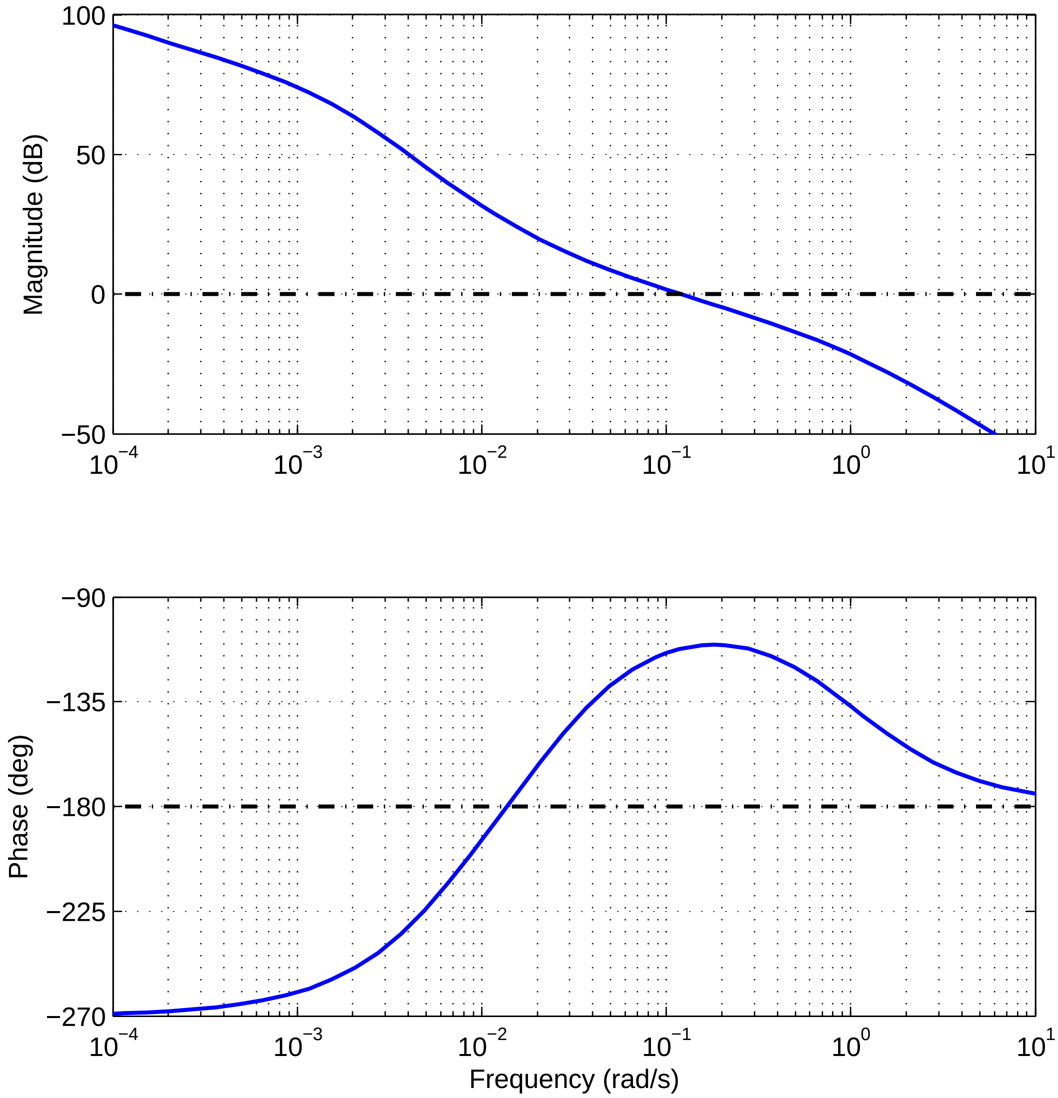


FIGURE 3.8: Filtered PID controller, $\eta$ Bode plots

| Gain margin [dB] | $\omega_c$ [rad/s] | Phase margin [deg] | $\omega_{180}$ [rad/sec] |
|---|---|---|---|
| -26 | 0.014 | 67.8 | 0.12 |

TABLE 3.3: Filtered PID controller, $\eta$ margins

The controller has then been tested in a simplified simulator, which included only a partial inertial sensor model and no spacecraft nor environment models, and showed much better performances with respect to the unfiltered one. However, a 6 seconds delay in the control activation had to be introduced to allow stabilization of the filter output (see the filter step response in figure 3.9).

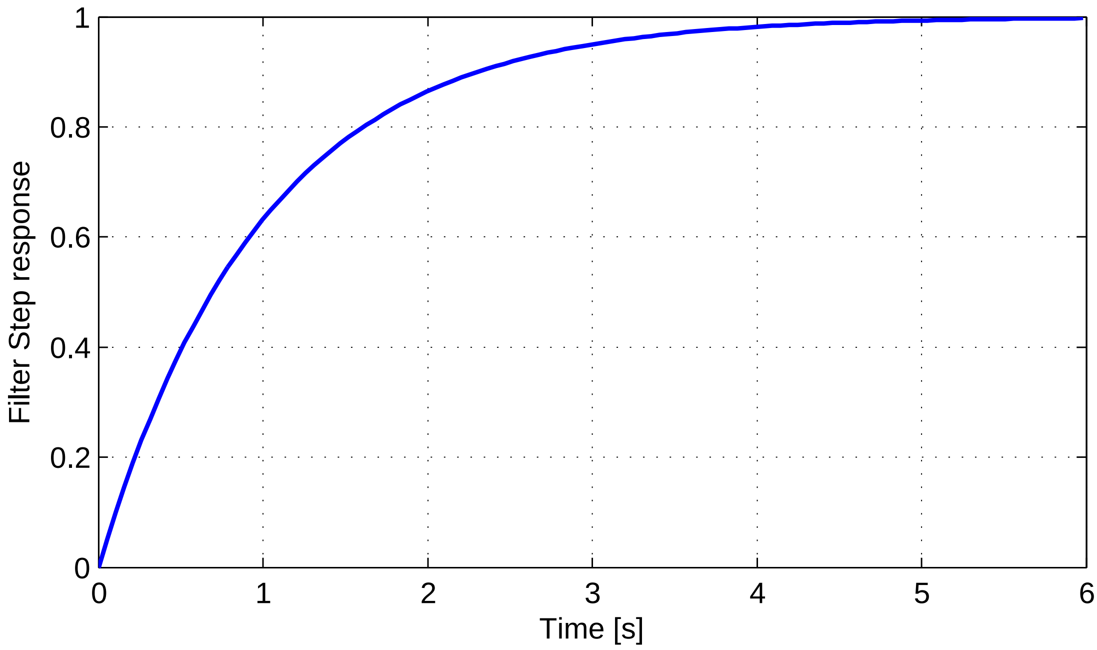


FIGURE 3.9: Lowpass Filter Step Response

The plots of the command signal in figure 3.10 clearly show the vast improvement in terms of command noise given by the introduction of the low pass filter. Figure 3.11 shows the resulting $\eta$ dynamics achieving steady state conditions.

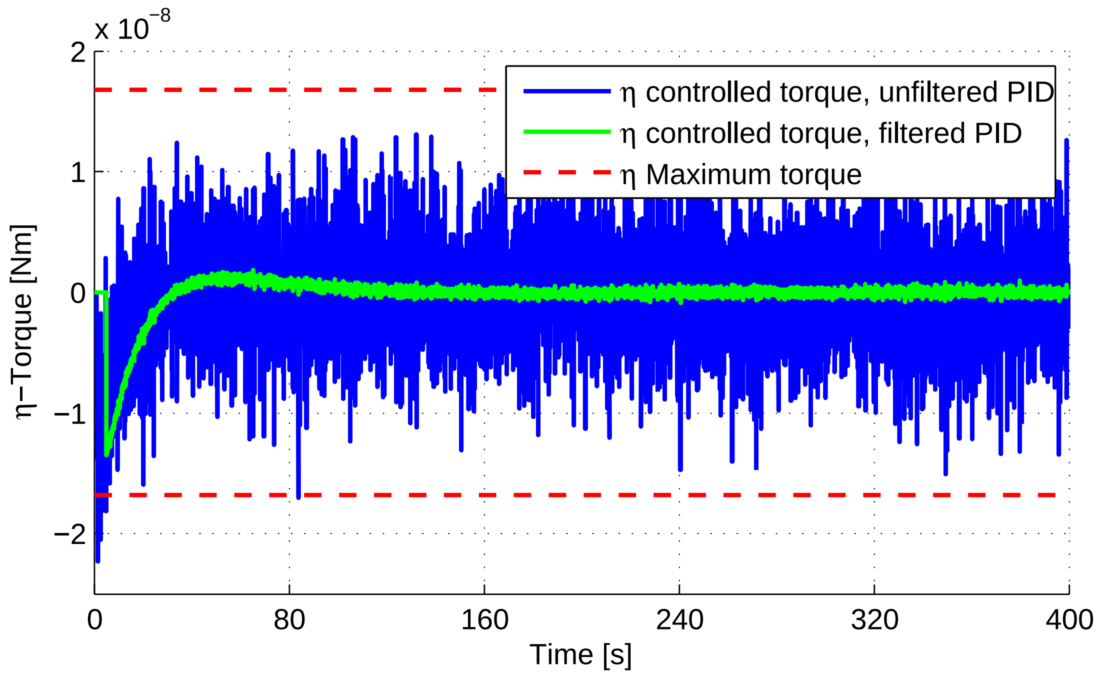


FIGURE 3.10: Filtered/Unfiltered PID Torque Command Comparison

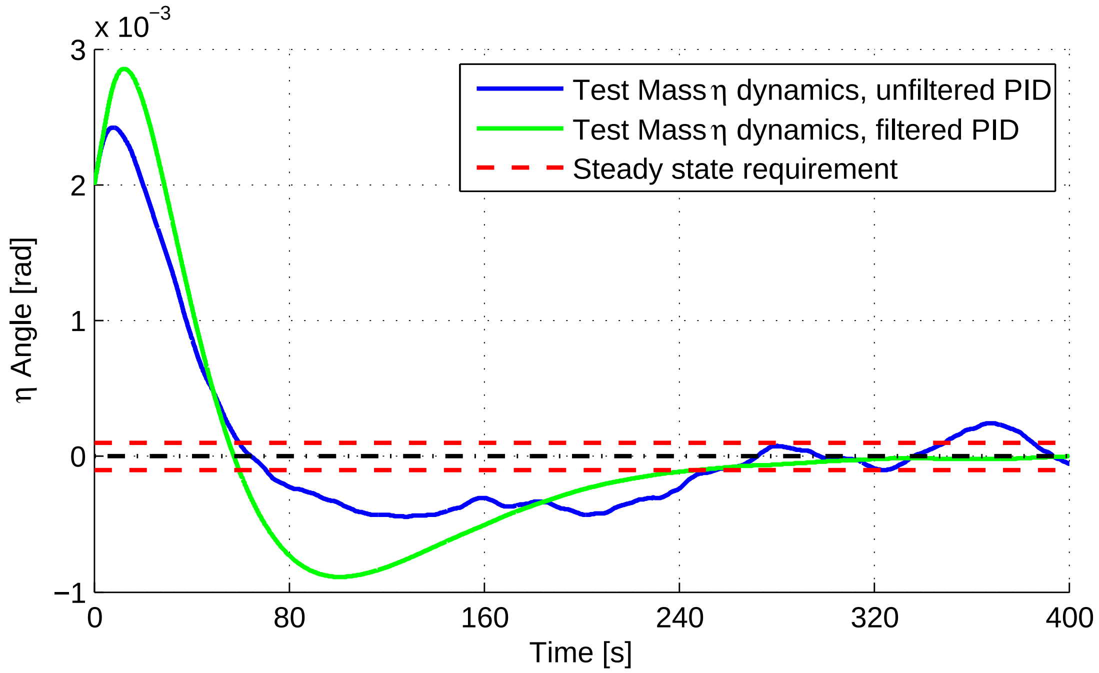


FIGURE 3.11: Filtered/Unfiltered PID $\eta$ Dynamics Comparison

## 3.2 State Space Controller

Once the PID controller with just position feedback has been completed, a time domain, or state space approach to the control problem is considered.

The idea is to use full state feedback to improve the performances of the system, mainly through exploitation of velocity signal feedback.

As in standard approach, thanks to the separation principle, first the controller design is carried out by assuming that the full state feedback is available, and then a proper estimator is designed to provide the actual state estimation feedback to the controller itself.

The matrix form of the equations of motion for one single degree of freedom, is derived. The x degree of freedom is still taken as example for the derivation.

In scalar representation, the equation of motion writes:

$$\ddot{x} = -\omega^2 x + u + d \tag{3.7}$$

Where $u$ is the control signal, and $d$ is the DC disturbance acceleration. Going to the matrix representation:

$$\left\{ \begin{array}{c} \dot{x} \\ \ddot{x} \end{array} \right\} = \left[ \begin{array}{cc} 0 & 1 \\ -\omega^2 & 0 \end{array} \right] \left\{ \begin{array}{c} x \\ \dot{x} \end{array} \right\} + \left[ \begin{array}{c} 0 \\ 1 \end{array} \right] u + \left[ \begin{array}{c} 0 \\ 1 \end{array} \right] d \tag{3.8}$$

Assuming the position $x$ to be the output of interest, the following state-space representation matrices can be identified:

$$A = \left[ \begin{array}{cc} 0 & 1 \\ -\omega^2 & 0 \end{array} \right]; \; B = \left[ \begin{array}{c} 0 \\ 1 \end{array} \right]; C = \left[ \begin{array}{cc} 1 & 0 \end{array} \right]; D = 0 \tag{3.9}$$

The presence of the disturbances $d$ prevents adoption of a proper, "clean", state-space representation. The problem of dealing with the disturbances can be solved by adopting two different strategies:

- Completely ignore the disturbances, and add an integrator to the controller, such that the system steady state error will be zero, whatever (within realistic limits) the disturbances are;
- Substitute the actual command signal with a fictitious one, called $u'$, defined as $u + d$, so that by pre-compensating the disturbances, a "clean" representation is recovered.

Both alternatives have been investigated, and the pre-compensated one, being based on a lower-order model, was found to be faster and better damped than the integrator one. For this reason, the full implementation of the controller (complete with state vector estimator) has been carried out only for the pre-compensation strategy.

However, both control strategies are illustrated for the z degree of freedom, and their performances are compared assuming perfect state vector feedback.

### 3.2.1 Addition of an Integrator

The $d$ term is here assumed as a disturbance introduced in an otherwise "pure" system; therefore it is neglected in the equations, and an integrator is added to avoid steady state errors [10].

Figure 3.12 shows the block diagram of the system, with the addition of an integrator.

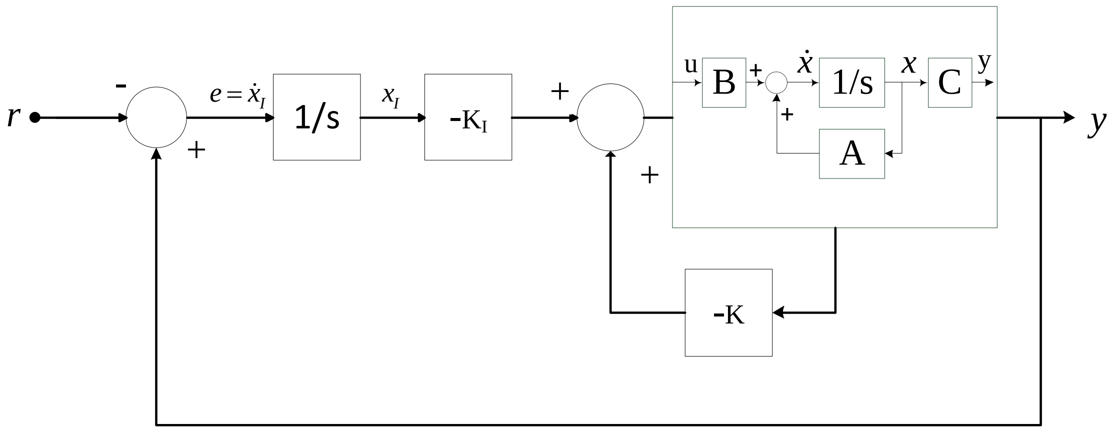


FIGURE 3.12: System block diagram with integrator

The matrix equations for the system then write:

$$\begin{aligned} \dot{\underline{x}} &= A\underline{x} + Bu \\ y &= C\underline{x} \\ \dot{x}_I &= r - y \\ u &= -K\underline{x} - K_I x_I \end{aligned} \tag{3.10}$$

By extending the state vector with the additional state $x_I$, the system can be written in an equivalent state space form:

$$\left\{ \begin{array}{c} \dot{\underline{x}} \\ \dot{x}_I \end{array} \right\} = \left[ \begin{array}{cc} A & 0 \\ -C & 0 \end{array} \right] \left\{ \begin{array}{c} \underline{x} \\ x_I \end{array} \right\} + \left[ \begin{array}{c} B \\ 0 \end{array} \right] u + \left[ \begin{array}{c} 0 \\ 1 \end{array} \right] r$$

$$y = \left[ \begin{array}{cc} C & 0 \end{array} \right] \left\{ \begin{array}{c} \underline{x} \\ x_I \end{array} \right\} \tag{3.11}$$

With no reference signal, the above description matches exactly that of a “pure” state space representation. The controller gain vector $\left[ \begin{array}{cc} K & K_I \end{array} \right]$ is then obtained using the LQR technique, which means, minimizing the cost function:

$$J = \int_0^t \left\{ \begin{array}{c} \underline{x} \\ x_I \end{array} \right\} Q \left\{ \begin{array}{c} \underline{x} \\ x_I \end{array} \right\}^T + uRu^T d\tau \tag{3.12}$$

The Q and R matrices are defined in the following way:

$$Q = \left[ \begin{array}{ccc} 1/x_{\max}^2 & 0 & 0 \\ 0 & 0 & 0 \\ 0 & 0 & k_1 \end{array} \right]; \; R = \frac{k_2}{u_{\max}^2} \tag{3.13}$$

With $k_1$ and $k_2$ being factors used to tune the controller itself. The $x_{max}$ and $u_{max}$ parameters are taken as, respectively, the maximum allowed overshoot and the maximum command that can be actuated at the zero position.

Once the controller gains are known, the overall system, from reference to output, is described by the following representation:

$$\left\{ \begin{array}{c} \dot{\underline{x}} \\ \dot{x}_I \end{array} \right\} = \left[ \begin{array}{cc} A - BK & -BK_I \\ -C & 0 \end{array} \right] \left\{ \begin{array}{c} \underline{x} \\ x_I \end{array} \right\} + \left[ \begin{array}{c} 0 \\ 1 \end{array} \right] r$$

$$y = \left[ \begin{array}{cc} C & 0 \end{array} \right] \left\{ \begin{array}{c} \underline{x} \\ x_I \end{array} \right\} \tag{3.14}$$

The choice of the parameters $k_1$ and $k_2$ is done on a trial and error basis, starting with a value of 1 and adjusting them according to the guidelines that:

- Changing $k_1$ mostly affects the time response (a smaller $k_1$ means smaller integral contribution, therefore slower convergence);

- Decreasing $k_2$ increases the magnitude of the command signal

The gains for the controller shown in the comparison of section 3.2.3 have been derived with the following values for the parameters:

- $k_1 = 50$
- $k_2 = 0.35$

and resulted in the following gains:

- $K = \begin{bmatrix} 0.0013 & 0.0502 \end{bmatrix}$
- $K_I = -6.7172 \cdot 10^{-6}$

### 3.2.2 Pre-Compensation

The disturbance term $d$ is here assumed to be a constant offset in the command signal; the equations can be written using a new notation:

$$\begin{aligned} \dot{\underline{x}} &= A\underline{x} + Bu' \\ y &= C\underline{x} \\ u' &= u + d \end{aligned} \tag{3.15}$$

The controller is, like in the previous case, derived by using the LQR technique, using the following weight matrices:

$$Q = \begin{bmatrix} {}^{1}\!/\!{x^2_{\max}} & 0 \\ 0 & 0 \end{bmatrix}; \; R = \frac{k}{(u_{\max} - d)^2} \tag{3.16}$$

The $R$ matrix must take into account the limitations on the actual command, even though it is acting as a weight on $u' = u + d$.
The maximum (absolute) value that $u$ can assume is $u_{max}$. Therefore, the maximum (absolute) value that $u'$ can assume must take into consideration the possibility of a command whose sign is opposite to the disturbance one. The limit is then $u' \leq u_{\max} - d$.
The $k$ factor is, again, used to tune the controller. The value of $k$ is chosen such that the system does not saturate. This tuning is carried out on a trial and error basis, following the guideline that decreasing $k$ will increase the command signal magnitude.

The gains for the controller shown in the comparison of section 3.2.3 have been derived with the following values for the parameters:

- $k = 0.17$

and resulted in the following gains:

- $K = \left[ \begin{array}{cc} 0.0011 & 0.0477 \end{array} \right]$

Once the controller gains are defined, in order to obtain the actual command signal by having the simplified one, the definition is inverted:

$$u = u' - d \tag{3.17}$$

The $u$ command is finally the one that is commanded to the electronics.
The disturbance factor to be subtracted from the simplified command must be somehow assessed. It will be done by designing a proper state estimator, which takes into account the DC disturbances as a third state.

### 3.2.3 Choice of State-Space Control Law

A controller example for the test mass $z$ degree of freedom was implemented with both strategies that have been introduced in the previous sections. Both resulting controllers were tuned to be essentially equivalent in command signal usage. Plots showing the displacements and command for both controllers are shown in figures 3.13 and 3.14.

The pre-compensated strategy, being based on a lower-order model, shows a faster and better damped time response. Its tuning is also simpler, being limited to the adjustment of one single parameter. For these reasons, the design process has been continued only for the pre-compensated controller.

### 3.2.4 State Estimator Design

The assumption of having a full-state feedback, on which the above controller designs are based, must be verified by designing a state estimator which can provide an accurate estimation of the system state vector to the controller.

The state estimator, however, will have to provide not only estimation of position (which is anyway available as measurement) and velocity, but also force and torque disturbances (usally called DC disturbances), for use in the determination of command offset for pre-compensation.

Two estimator designs have been considered and carried out:

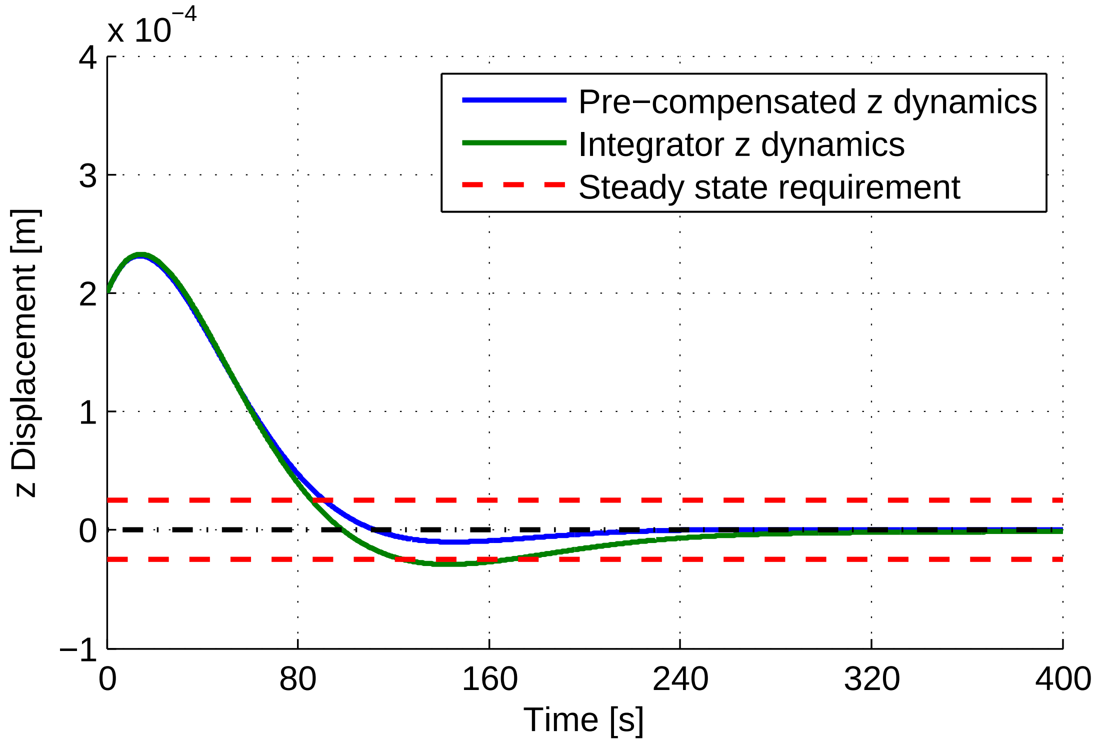


FIGURE 3.13: Compensation strategies, displacements

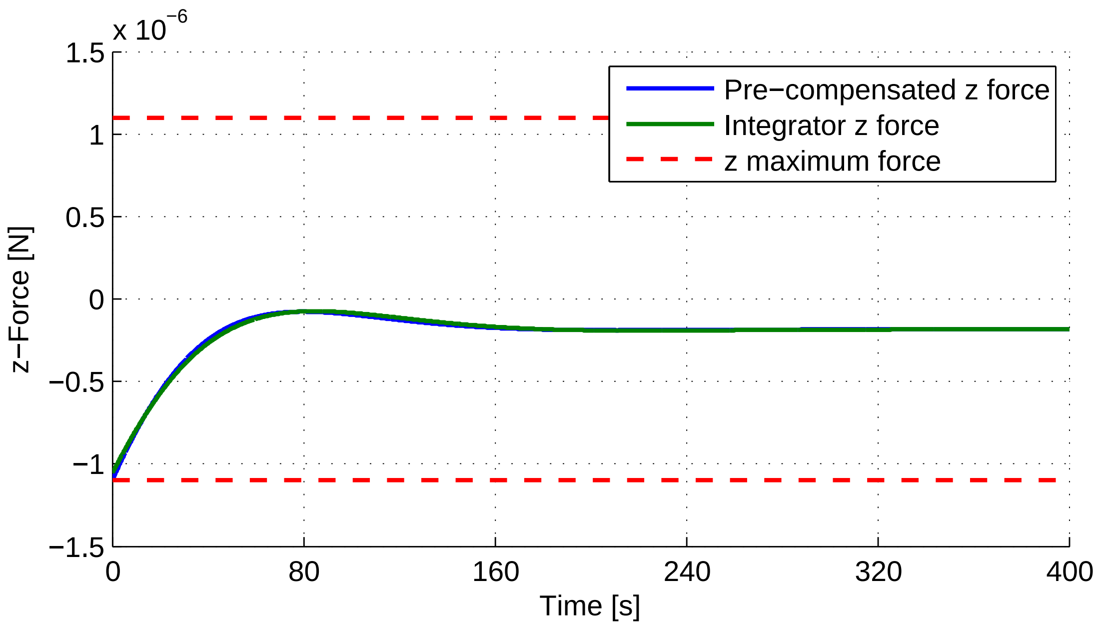


FIGURE 3.14: Compensation strategies, command

- A reduced state observer, based on the one already designed for the LISA pathfinder DFACS controller [4];
- An unsteady Kalman filter;

In order to be able to carry out estimation of the DC disturbances, both estimators are based on a three-state model of the system, in which the third state is the DC force itself. The matrix equations for this representation of the system write:

$$\left\{ \begin{array}{c} \dot{x}_1 \\ \dot{x}_2 \\ \dot{x}_2 \end{array} \right\} = \begin{bmatrix} 0 & 1 & 0 \\ -\omega^2 & 0 & 1 \\ 0 & 0 & 0 \end{bmatrix} \left\{ \begin{array}{c} x_1 \\ x_2 \\ x_3 \end{array} \right\} + \begin{bmatrix} 0 \\ 1 \\ 0 \end{bmatrix} u \tag{3.18}$$

$$y = \begin{bmatrix} 1 & 0 & 0 \end{bmatrix} \left\{ \begin{array}{c} x_1 \\ x_2 \\ x_3 \end{array} \right\}$$

With the following notation:

$$\begin{aligned} x_1 &= x \\ x_2 &= \dot{x} \\ x_3 &= d \end{aligned} \tag{3.19}$$

equation 3.18 becomes equivalent to the original system model. Please note that this representation could not be used to derive a controller design, since it can be shown that the controllability matrix for such a system is singular (the third state is not controllable; it has no connection to the input).

Starting from this system representation, the two estimators are derived.

#### 3.2.4.1 Reduced State Observer Design

The reduced state observer examined for the present controller design is derived by standard approach [10]. For its complete derivation see Appendix C.1. Its main characteristic is that the estimate is limited to the states which are not readily available (the position is therefore not estimated).

For the specific case, the design parameters upon which the gain vector is derived are:

- the observer dynamics damping ratio
- the observer settling time

The damping ratio $\xi$ is chosen to be 1 to obtain well-damped dynamics.
Imposing a short observer settling time (i.e. making the system fast) results in a noisy state estimate. On the other hand, making the system slow allows for more noise rejection at the cost of a longer convergence time.
A settling time of 10 seconds has been chosen. This results in a rather fast observer (the slowest state estimate to reach steady state takes about 30 seconds) that however does not show great noise rejection properties, especially on the third state estimate.

#### 3.2.4.2 Kalman Filter Design

The Kalman filter can be described as an algorithm that uses a succession of measurements of some quantity, corrupted by noise, to produce an estimate of some unknown variables.
The Kalman filter is an interesting estimator for the present case, due to the fact that both the taken measurements, and the applied command, are corrupted by some uncertainties and noise. It is then desirable to employ such an estimator, to obtain good noise rejection characteristics without having to wait a long time for the initial estimate to converge.
Fundamentals of Kalman filtering can be found in a number of optimal estimation textbooks ([1], [11]). The derivation process of the Kalman filter used for the studied system is reported in Appendix C.2. The main difference between a Kalman filter and a reduced state observer is that the KF is a time-variant system. It can be identified as a filter whose speed is initially determined by the error covariance matrix initial conditions, and settles in time to one whose speed is determined by the noise model of the system. While this characteristic has great advantages (very short convergence time due to fast filter at initialization, followed by great noise rejection due to slow filter at steady state) it also has its drawbacks, mainly in implementation difficulties.

#### 3.2.4.3 Choice of State Estimator

To provide the controller with an estimate of the system state vector, the Kalman filter has been chosen as the best state estimator for our purposes. This choice is based on the fact that the KF has faster initial dynamics than the observer (reaches more quickly the correct estimate) while still having better noise rejection properties at all times of interest (after controller activation). Moreover, the KF allows us to introduce in the estimating procedure the informations we have about the system uncertainties.

### 3.2.5 Complete State Space Controller

The combination of a Kalman filter and a control law based on LQR gains constitutes a Linear Quadratic Gaussian regulator (LQG).

The controller is based on the pre-compensation strategy. The tuning was carried out after implementation with the KF, so it could be tailored to the filter settling time. The controller cannot be activated before the estimates are available, i.e. the filter has settled. Therefore, there will be some free-drift time during which the worst-case initial conditions will evolve to some different states. The controller is then tuned such that even with worst case IC, after the free drift time, a relevant portion of the command is exploited while still avoiding saturation.
The resulting k parameters are:

- $k = 0.6$ for the $z$ degree of freedom;
- $k = 0.6$ for the $\eta$ degree of freedom;

Since the highest demand for command signal is at controller activation (displacement and velocity initial conditions plus system evolution during drift time), changing the activation time might require further tuning of the controller to either avoid saturation or better exploit the system actuation capabilities.

## 3.3 Best Linear Controller

The performance of the previously derived PID and LQG controllers are compared, to assess which one should be selected as the “best” linear controller for the studied system. For both implementations, first position control performances are presented, and then the related command signals are shown. As usual, the $z$ DoF is reported as representative of the translational degrees of freedom, while the $\eta$ one stands for the rotational.
From comparison of the simulation results for the two controllers, the following statements can be made:

- The PID controller has a slightly reduced maximum overshoot with respect to the LQG one on the rotational DOF. This is mainly due to the greater command signal at control activation. The particular derivation of the PID gains allows easy modification of the maximum commanded forces/torques, therefore obtaining a very good release velocity breaking performance. The use of weight matrices to tune the LQG controller does not allow such an easy control over the initial command.

- The LQG controller shows an overall faster dynamics to reach both steady state and zero position conditions, due to the fact that is based on a lower order model. Additionally, though not being a really significant effect, the PID command signal is noisier than the LQG one.

The overall best linear controller has been selected to be the LQG one. The reason for this choice is that, while the maximum overshoot of the two controllers is almost the same, the time it takes them to settle to steady state is different, clearly favoring the LQG controller (about 150 vs 180 seconds for the z DOF, 150 vs 240 seconds for the $\eta$ one).

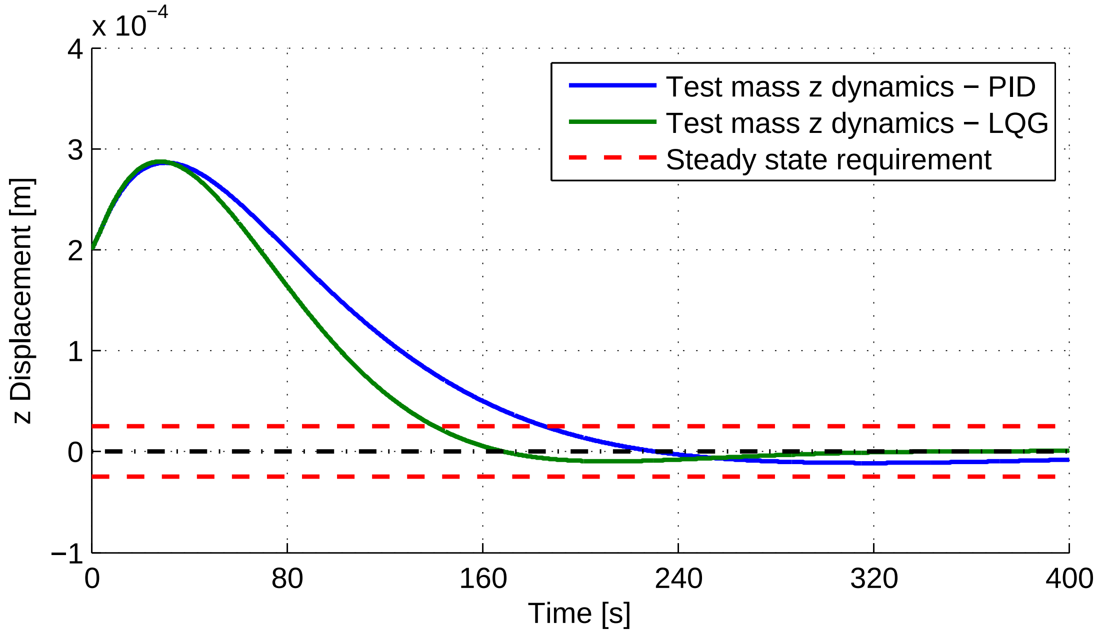


FIGURE 3.15: PID vs LQG comparison, Test Mass position

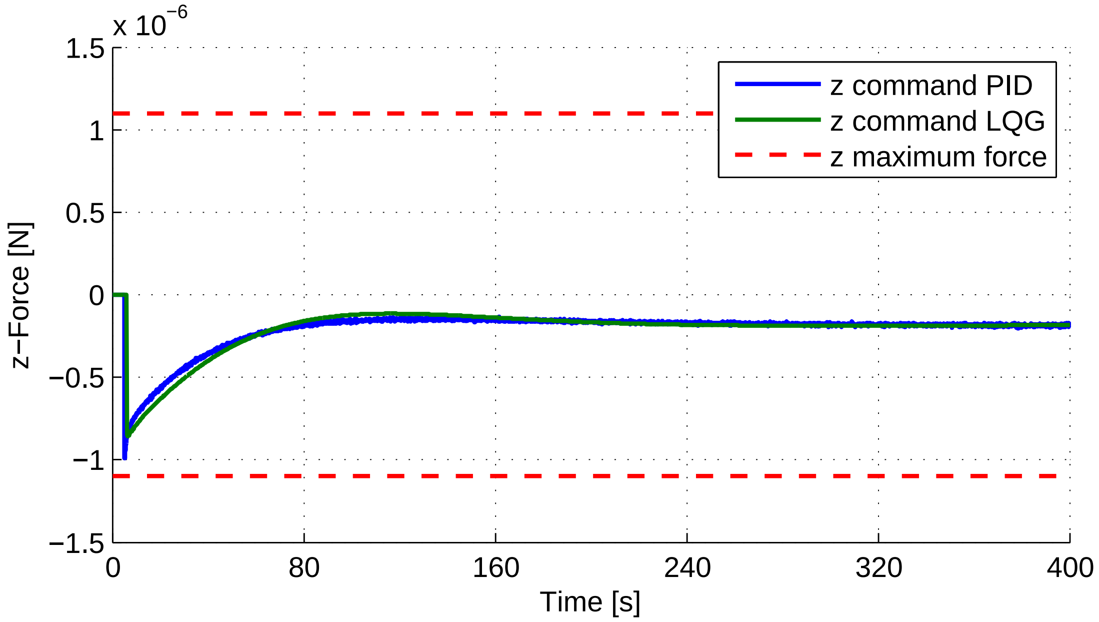


FIGURE 3.16: PID vs LQG comparison, force control signal

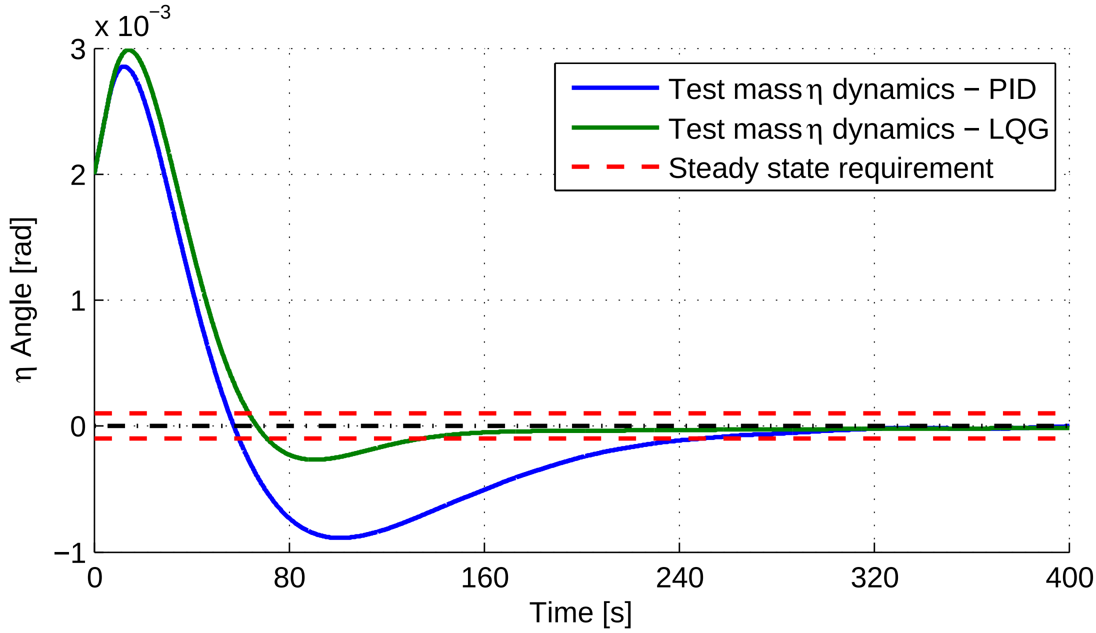


FIGURE 3.17: PID vs LQG comparison, test mass attitude

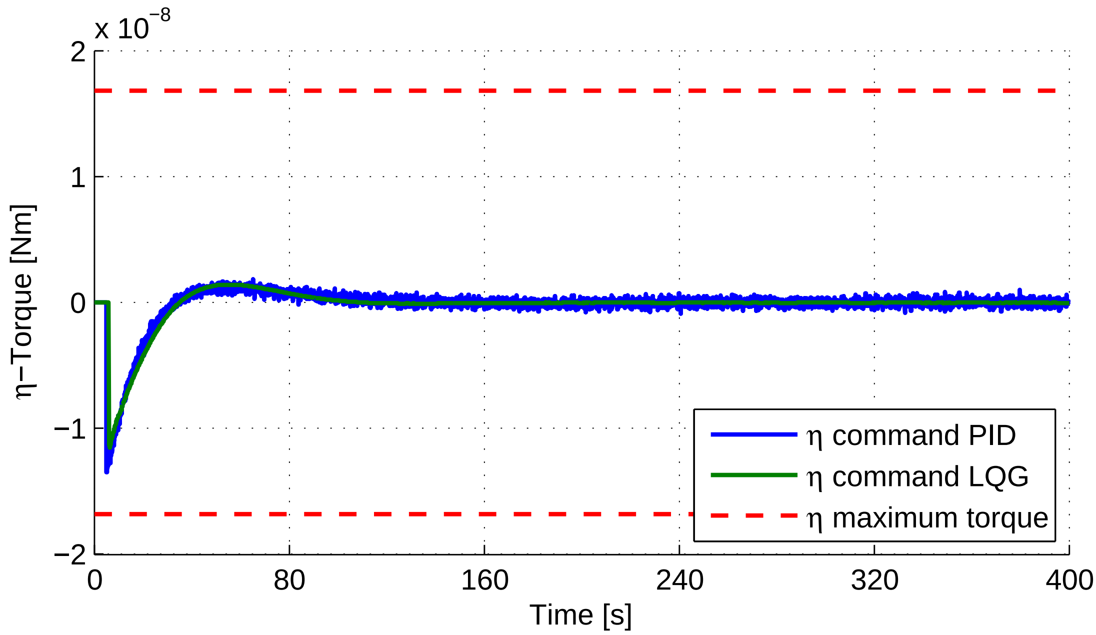


FIGURE 3.18: PID vs LQG comparison, torque control signal

# Chapter 4

# Design and Analysis of Nonlinear Control Methods

In this chapter, the design process of a nonlinear controller for the system is illustrated. First, the reasons that suggest the exploitation of a nonlinear law are presented, together with the idea of what kind of control law should be employed. Then, the development of the actuation algorithm needed to implement the control law is presented. Finally, the resulting nonlinear controller is illustrated together with its performance.

## 4.1 Motivation and Strategy

The ideal controller should, as quickly as possible, stop the test mass drift after release (i.e. reduce the TM velocity from the initial value to 0). The key feature of such a controller should be the application of the highest possible electrostatic force, which will result in the shortest breaking time and the smallest possible maximum overshoot. Ideally the controller shall counteract the residual release velocity applying always the maximum force, and stop as soon as the mass velocity is zero. It is clear that this kind of control cannot be achieved by using a linear law, as no linear law abruptly changes the command signal between different values. For this reason, the design of a nonlinear control law has been investigated. The control law that reduces the velocity to zero in the minimum possible time is simply a bang-bang velocity controller:

$$\dot{v} = -u_{\max} sign\left(v\right) \tag{4.1}$$

This first-order nonlinear control law can be shown to be always stable (Theorem 4.4, [12]). For the specific system case, however, the equation of motion has some additional terms. Focusing on the velocity, and neglecting the stiffness contribution, which is much smaller than both the DC disturbances and the actuation force[1], the following equation is derived:

$$\dot{v} = -u_{\max} sign\,(v) + d \tag{4.2}$$

For the stability to hold, the term on the right hand side must switch sign at the velocity ($v$) zero crossing, which means that the $u_{max}$ quantity must be greater than the DC disturbance.

- $\begin{cases} v = 0 - \delta v \\ |u_{\max}| + d > 0 \end{cases}$
- $\begin{cases} v = 0 + \delta v \\ -|u_{\max}| + d < 0 \end{cases}$

Assuming a positive sign for the $d$ term, the first condition is always met. On the other hand, the second one requires $|u_{\max}| > d$ (the same conclusion could be derived by assuming negative $d$ and thus automatically veryfing the second condition but not the first). In the case where the maximum available actuation was smaller than the DC disturbance, there is no possibility to stop the velocity, therefore leading to instability of the system.
The fact that the $u_{max}$ value for our system is position dependent introduces some additional complications for this kind of reasoning; however, the main point is unchanged: if enough electrostatic actuation authority is available, then the control law $\dot{v} = -u_{\max} sign\,(v) + d$ exploits (by definition) the maximum possible command, and is therefore the best control law to stop the TM velocity as fast as possible, with minimum overshoot.

## 4.2 Development of Maximum Force Actuation Algorithm

In order to implement the control law presented in the section above, knowledge of the value of the maximum actuation authority $u_{max}$ is required. Due to the nature of the employed electrostatic actuation, the limit on electrode voltages (±130.1 V) turn into a position-dependent limit on the maximum forces and torques that can be generated. The actuation algorithm in use [7] exploits position readings to compute, using a first order Taylor series approximation of the analytical force equation as described in [13], for each set of electrodes, the voltages resulting in the required force and torque commands. What is needed to implement the nonlinear control law is an actuation algorithm that, based

[1] $\left|\Omega_{11}^2 x_{\max}\right| \cong 1 \cdot 10^{-9} \frac{m}{s^2} \ll d = 2.4 \cdot 10^{-8} \frac{m}{s^2}$

on position readings and torque command, computes the voltages resulting in maximum actuated force, and the value of the maximum force itself. The torque command is a required input because the same set of electrodes are used for both force and torque generation, therefore the computation of the voltage commands for each electrode set must take into consideration both force and torque commands (or, in this case, the torque command and the maximization of force).Such an actuation algorithm has been developed, and is outlined below. For more details on the derivation process, refer to Appendix D.1.

### 4.2.1 Concept of Maximum Force Actuation Algorithm

Assuming the required goal to be the maximization of positive actuated force for a given torque input, the algorithm is derived by solving the following problem for the four voltages:

$$F_x = \max\left[\frac{1}{2}\sum_{i=1}^{4} a_i V_i^2\right]_{V_i} \tag{4.3}$$

$$F_\varphi = \frac{1}{2}\sum_{i=1}^{4} b_i V_i^2 \tag{4.4}$$

$$V_{TM} = \frac{1}{2}\sum_{i=1}^{4} c_i V_i \tag{4.5}$$

A mathematically correct way to solve this problem would involve zeroing the derivative of the force with respect to the voltages. Such an approach however, can be shown to be impractical (it involves finding roots of $6^{th}$ order polynomials, for which no closed form solution exist), and not suitable for on-board implementation. Therefore, the equation system is analyzed with a more practical approach, taking advantage of the nature of the coefficients signs. The a, b and c coefficients are capacitances and their derivatives (see equations 2.3 and 2.4) expressed according to the adopted capacitance model [7].

$$Fx = \frac{1}{2}\left(|a_1|\, V_1^2 + |a_2|\, V_2^2 - |a_3|\, V_3^2 - |a_4|\, V_4^2\right) \tag{4.6}$$

$$F_\varphi = \frac{1}{2}\left(|b_1|\, V_1^2 - |b_2|\, V_2^2 + |b_3|\, V_3^2 - |b_4|\, V_4^2\right) \tag{4.7}$$

$$V_{TM} = c_1V_1 + c_2V_2 + c_3V_3 + c_4V_4 = 0 \tag{4.8}$$

This particular form of the equations can be used to develop a preliminary force-maximizing strategy. The ideal approach is to maximize $V_1$ and $V_2$, while zeroing $V_3$ and $V_4$. However, doing so while still satisfying the third equation, would result in some position-dependent output torque different from the command torque. It is therefore

necessary to have at least one other voltage different from zero.
By looking at the $V_3$ and $V_4$ coefficients, it becomes clear that, while both contribute to a negative force, $V_3$ provides positive torque contribution, while $V_4$ provides a negative one. Following this consideration, the additional non-zero voltage can be chosen on the basis of the input torque sign: the $V_3$ voltage is chosen when requiring a positive torque; the $V_4$ voltage when requiring a negative torque.
Having chosen the triplet of voltages for which we want to solve the problem described by equations 4.6 to 4.8, it is assumed that, being $a_1$ and $a_2$ both positive, the maximum force will be obtained when either $V_1$ or $V_2$ assumes the maximum allowed magnitude (130.1 V).
To find, e.g., the maximum positive force for a given positive torque, the algorithm is then the solution to the above problem, for the special case:

- $V_4 = 0$;
- Either $|V_1|$ or $|V_2| = 130.1$ V;
- $F_\varphi \geq 0$, given.

### 4.2.2 Torque Limitation

The above described actuation algorithm is implemented as an expansion of the existing improved one [7]. Its goal is providing the highest possible force of the required sign, for the measured test mass position and attitude, while at the same time producing the commanded torque. The main difference with respect to the algorithm described in [7] is that in the new one, at least one voltage always assumes maximum magnitude. For a given test mass displacement, a higher force is produced the lower the torque command is. This happens because to produce a torque, an electrode which gives negative force contribution is always activated. For this reason, to better exploit the new algorithm, the requested torque should be limited to a low value while a maximum force is commanded. This particular feature should be taken into consideration when designing the control strategy, in terms of test mass attitude control gains.
An evaluation of the minimum torque command required to avoid the maximum overshoot, for different release attitudes and rates has been carried out, and its details can be found in Appendix D.2. The result has been that for an initial attitude and rates as defined in table 2.1, the maximum overshoot can easily be avoided. A final torque limit of 5 nNm was chosen. This is now considered as a requirement in the TM attitude controller design, while operating with the nonlinear controller.

## 4.3 Design of Nonlinear Controller

A different nonlinear control strategy is applied to the linear and to the rotational degree of freedom.

The force control strategy is composed of two parts:

- The nonlinear velocity breaking controller (eq 4.2), which guarantees the most effective breaking of the test mass within hardware limits;
- A linear controller, to control the test mass from the position where the breaking has been completed back to the zero position.

The torque controller strategy consists of the same linear control law, calculated using two different set of gains depending on the force control:

- A high gain controller, designed for nominal maximum torque limit, to be used when the force controller is operating with its linear control law;
- A low gain controller, designed for the reduced torque limit, to be used when the force controller is operating with its velocity breaking control law.

Two different control laws are required because during velocity breaking the commanded torque needs to be limited to the 5 nNm value, while during linear force control such limit is unjustified and therefore the appropriate DOF limit is assumed.
The velocity breaking law has been slightly modified in order to:

- Avoid control chattering due to uncertainties and noise in the velocity estimate: a velocity threshold has been defined, such that a velocity estimate below it causes the control to be handed over to the linear law;
- Avoid slowing the test mass path trajectory to the zero position: the velocity breaking is activated only if the signs of measured displacement and velocity are the same, meaning the mass is drifting away from the nominal position. This way, a high velocity towards the nominal position is not necessarily counteracted, but handled by the linear controller, allowing for a faster settling of the dynamic.

The diagrams in figures 4.1 and 4.2 show the control switching logic respectively for force and torque controllers. Due to the various switching involved (in command sign, control laws and gain sets) in the defined controller, it was labeled as the “Variable Gains Switching” (VGS) controller, or shorter “Switching” controller. A particular feature of

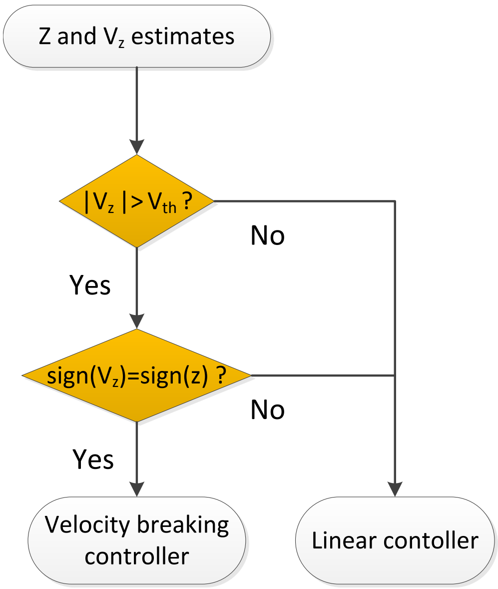


Figure 4.1: Nonlinear force control switching logic

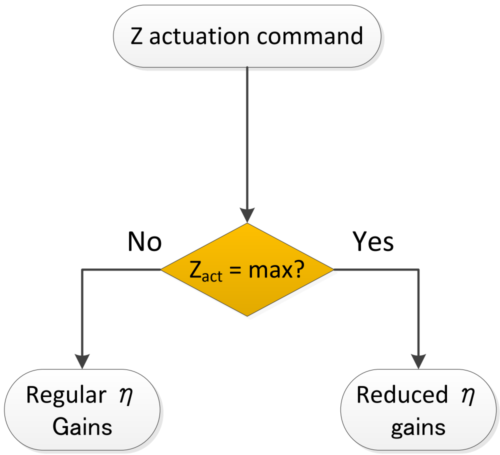


Figure 4.2: Nonlinear torque control switching logic

the nonlinear velocity breaking controller is the absence of a magnitude command (the output of the breaking controller is a +/- sign, the maximum force actuation algorithm then carries out the maximization of the force based on current TM position and torque command). Thus, a corresponding force command as input to the state estimator (the Kalman filter for our case) is needed. The problem has been addressed by introducing an additional output to the actuation algorithm, which carries out the calculation of the actuated force based on the actuated voltages. However, due to the use of a first order capacitance model in the calculations, large displacements lead to large errors in the calculated force and therefore large errors in the estimator input. More details on this problem can be found in Appendix D.3.

# Chapter 5

# Comparison of Best Linear versus Nonlinear Control Strategy

The performances of the LQG controller versus the Switching controller were tested in the simplified simulator (partial inertial sensor model, no spacecraft and no environment models). In this chapter, test results of the performance adopting nominal case initial conditions (as in section 2.3.5.1, essentially the LPF release conditions) are presented.
After the two controllers have been compared adopting nominal requirements, the result of further testing is presented, showing the behavior for initial conditions exceeding the requirement limits. This is done in order to assess the maximum release velocity tolerated by the system within given constraints.
The resulting values of the maximum tolerable release velocity are then compared to an energy-based evaluation of the same quantity. The comparison of simulation versus ideal results is taken as a performance index for the controller.

## 5.1 Performance Comparison

### 5.1.1 Testing of the LPF Requirements Release Conditions

In figures 5.1 through 5.4 the compared performance of the LQG controller and the VGS one are shown. The simulations are run adopting worst case initial conditions (maximum initial displacement and velocity, of the same sign) and maximum disturbance force and torque, of the same sign as initial displacement and velocity (see section 2.3.5.1).
The maximum overshoot on the translation degree of freedom (z) is reduced with respect to the linear controller (due to the increased applied force), while the one on the rotation degree of freedom is increased (due to the limit on applied torque).

For this particular test case, the nonlinear controller shows only a marginal increase in performance with respect to the best linear one. This is due to the fact that in the simulation, TM initial conditions according to the LPF release requirements were set, exactly for which the linear controller has been tuned.

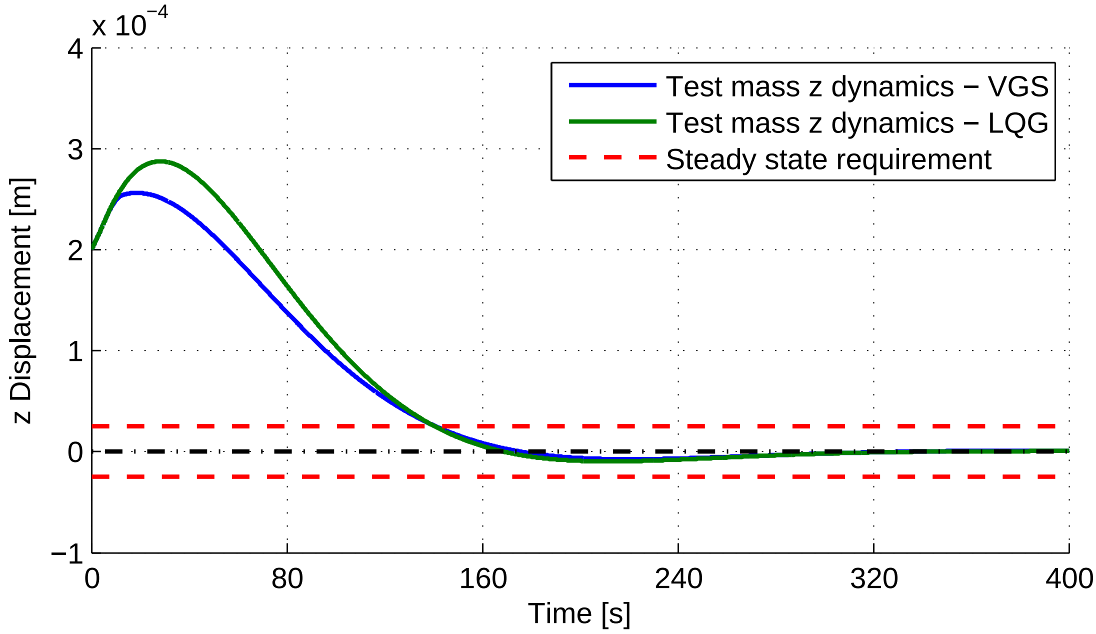


FIGURE 5.1: Controllers comparison: $z$ coordinate performance

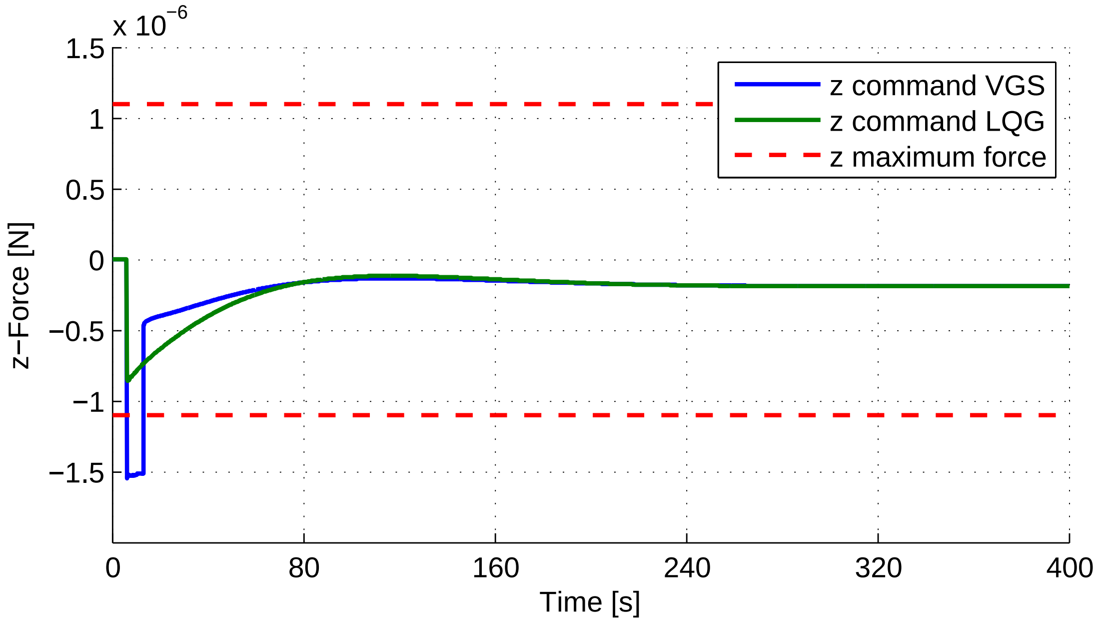


FIGURE 5.2: Controllers comparison: force control signal

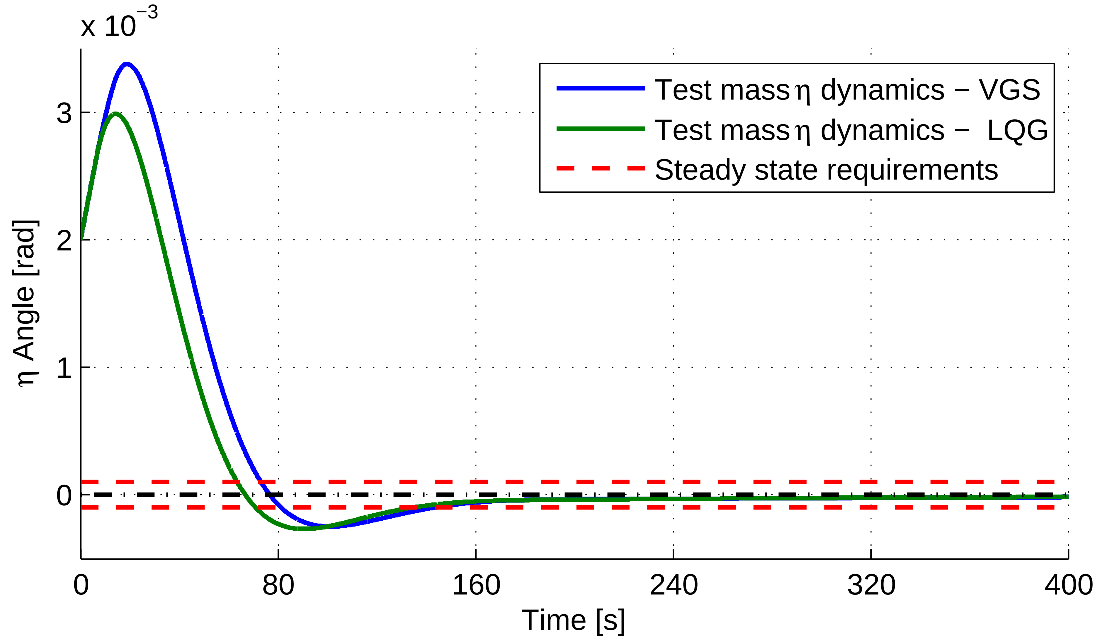


FIGURE 5.3: Controllers comparison: $\eta$ coordinate performance

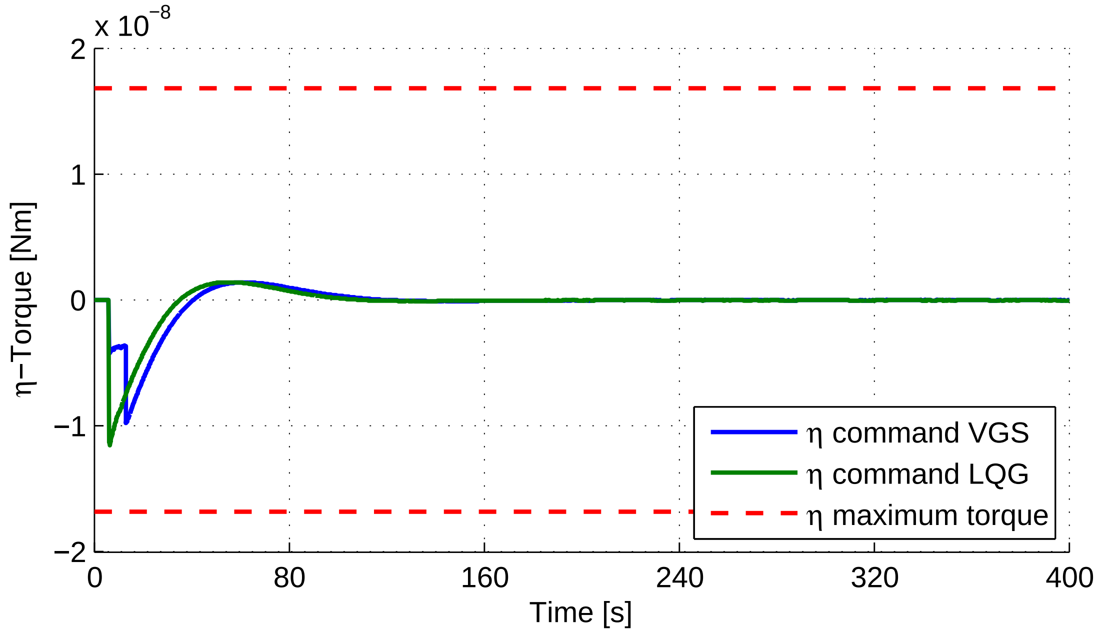


FIGURE 5.4: Controllers comparison: torque control signal

### 5.1.2 Velocity Limit Testing

Figures 5.5 through 5.8 show the results of simulations conducted to explore the limits of both controllers.

The goal of the test is to assess what is the highest release velocity that each controller can cope with while keeping the maximum displacement within the 1mm limit. Since the results of this test are to be later compared with a simplified energy based calculation of the physical limit of the system, some special conditions were adopted:

- All initial displacements are zero;
- All initial velocities are zero, except the z one;
- All disturbance forces are zero;
- All external stiffnesses are zero;
- No measurement and no actuation noise is present;
- The controller is initialized with no delay (the lack of noise allows for an essentially instantaneous convergence of the Kalman filter);

The velocity limit is considered to be reached when the maximum overshoot is greater than 1mm. For the linear control case, we consider force command greater than design limit to be a fail case as well. The reason for this distinction is that the overall design of the linear controller is such that a fixed (design) force limit should not be exceeded. The fact that reaching that particular force value does not always cause electrode saturation is irrelevant, because the whole design process assumes certain limit to be always respected, and where this assumption to fail, the correct behavior of the controller would not be guaranteed. Discarding this particular limitation of the linear controller is the main reason for the development of the nonlinear one, and in the end turns out to be a great advantage.

The plot in figure 5.6 show that the linear controller reaches force saturation for a release velocity of 15 $\mu m/s$, with the maximum overshoot being lower than 400 $\mu m$, as shown in figure 5.5.

The plot in figure 5.7 shows the nonlinear controller reaching the 1mm maximum overshoot for a release velocity of 39 $\mu m/s$. The great advantage of this controller is that its particular strategy and implementation allows for a full exploitation of the maximum electrode voltage. A drawback of the nonlinear control strategy is that the computation of the force corresponding to the applied voltages suffers from large displacement errors.

A consistent error in the command feedback to the Kalman filter causes a deviation in the state estimates, that for the DC force case is particularly slow to converge back to the real value. Figure 5.8 shows the forces generated by the maximum force actuation algorithm in the VGS control strategy, and the ones computed and fed as input to the Kalman filter. The discrepancy caused by the first order model can be easily seen. A correction meant to reduce this effect has been developed, and can be recognized as an horizontal segment of the $F_{comp}$ line. Details on the implemented correction can be found in the Appendix D.3.

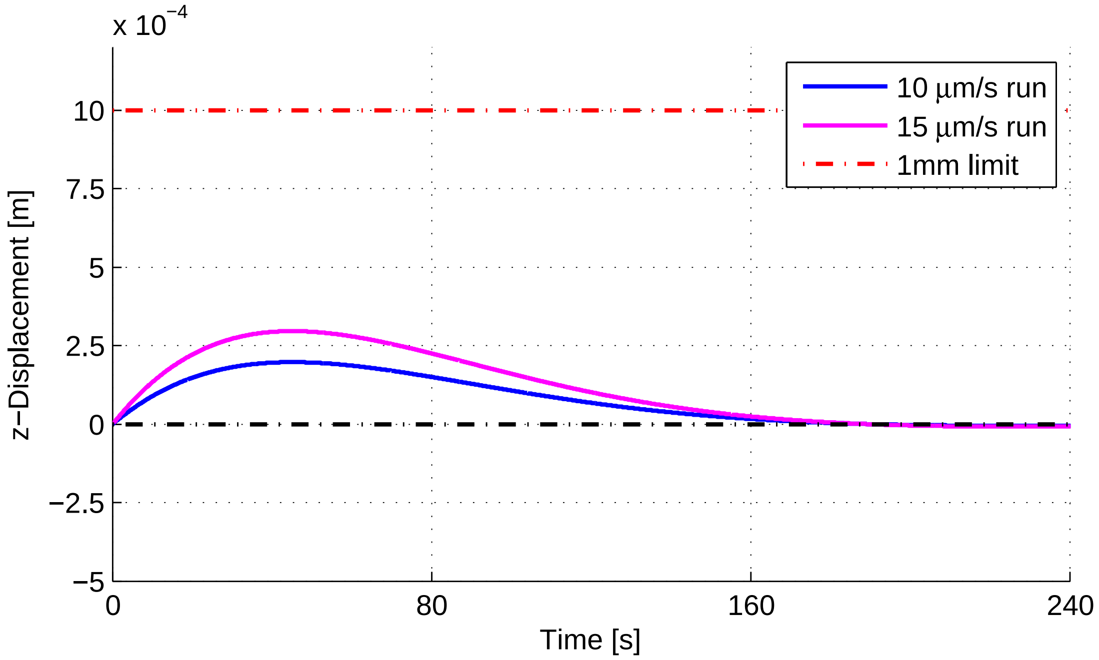


FIGURE 5.5: Displacements for LQG velocity limit tests

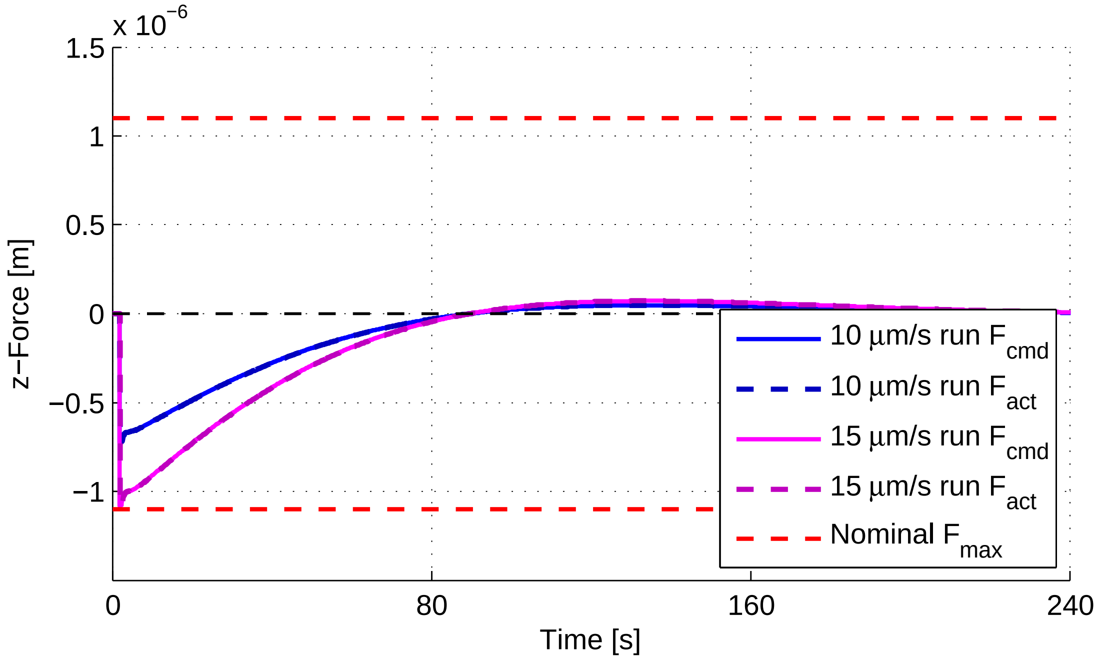


FIGURE 5.6: Force command for LQG velocity limit tests

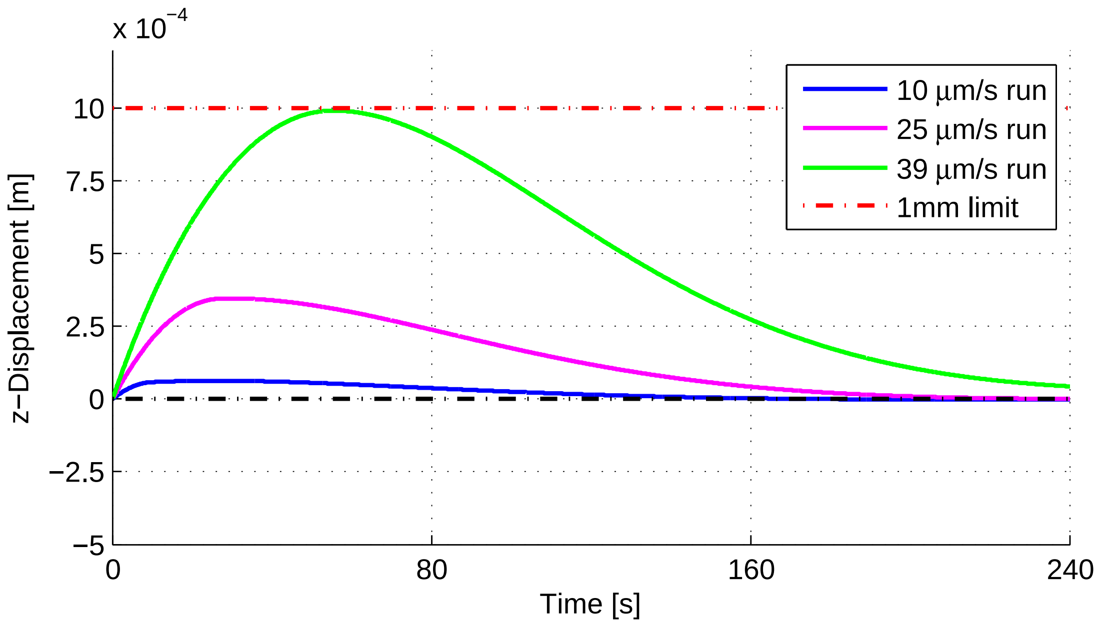


FIGURE 5.7: Displacements for VGS velocity limit tests

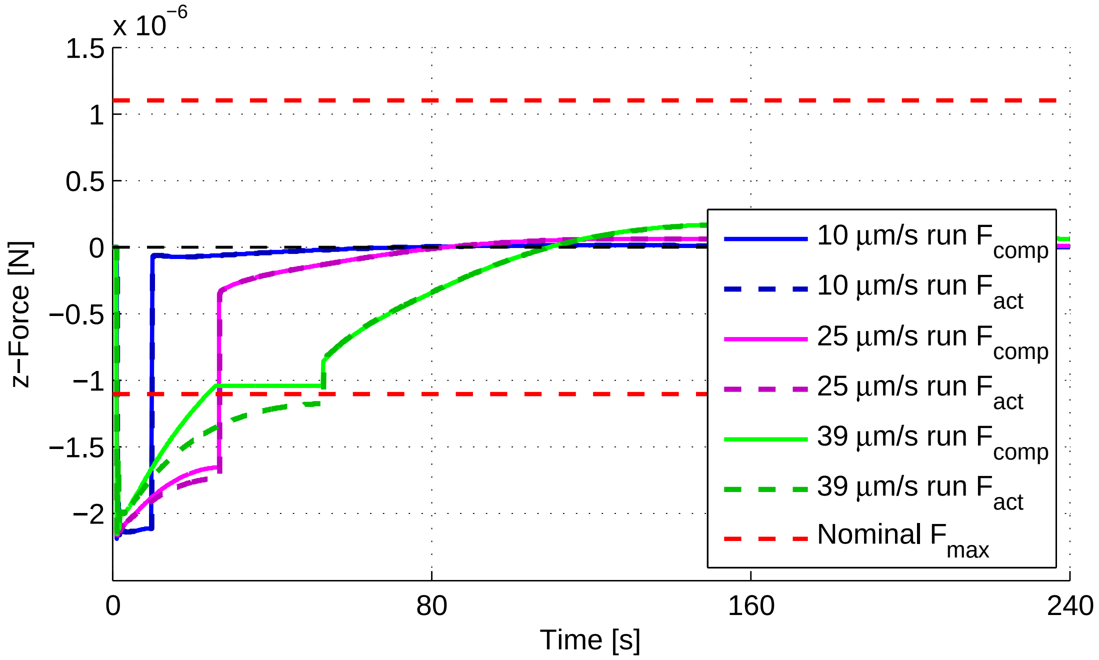


FIGURE 5.8: Force command for VGS velocity limit tests

## 5.2 Evaluation of Ideal Performance

With the goal of establishing a performance index for the capture performance of the various controllers, following the approach given in [14], an energy-based evaluation of the maximum tolerable release velocity such that the mass can be stopped within a given maximum overshoot is performed.

The general expression for the maximum force that can be generated is:

$$F_{\max} = \frac{N_x}{2}\left(\frac{\partial C_{EL,TM}}{\partial x} + \frac{\partial C_{EL,H}}{\partial x}\right) V_{\max}^2 \tag{5.1}$$

Where $N_x$ is the number of actively pulling electrodes, and $V_{max}$ is the maximum applicable voltage of 130.1 V for the specific case. The expressions for the capacitance derivatives are taken from a $6^{th}$-order IS capacitance model approximation. The case of a positive release velocity is considered, to be stopped using a negative $x$ force. No external forces are applied and the test mass is released in its nominal position. The equation that expresses conservation of energy between two time instants writes:

$$\frac{1}{2}Mv_i^2 + \int_{x_i}^{x_f} \underline{F}_{\max} \cdot \underline{dx} = \frac{1}{2}Mv_f^2 \tag{5.2}$$

Where $M$ is the test mass mass, $v_i$ is the initial (release) velocity and $v_f$ is the final velocity. By taking the final instant to be the complete breaking time, $v_f = 0$ and the r.h.s. vanishes. Substituting $\underline{dx} = \underline{v}dt$ into $\underline{F}_{\max} \cdot \underline{dx}$ the latter writes $\underline{F}_{\max} \cdot \underline{v}dt$.

Since the force is applied to reduce the velocity, the direction of the two vectors must necessarily be opposite, therefore yielding a minus sign in the scalar product:

$$\underline{F}_{\max} \cdot \underline{v}dt = -\left|F_{\max}\right|\left|vdt\right| = -\left|F_{\max}\right|\left|dx\right|$$

The highest tolerable initial velocity can then be calculated using the following formula:

$$v_i = \sqrt{\frac{2\int_0^{x_f} \frac{N_x}{2}\left(\frac{\partial C_{EL,TM}}{\partial x} + \frac{\partial C_{EL,H}}{\partial x}\right) V_{\max}^2 dx}{M}} \tag{5.3}$$

Equation 5.3 is evaluated for the case of interest ($z$), by substituting the numerical values of the capacitance model, and the following values for the remaining parameters:

- $V_{max} = 130.1V$
- $x_{max} = 1 \cdot 10^{-3}m$
- $M = 1.96kg$
- $N_x = 2$

The resulting value for the maximum tolerable velocity for a 1 mm maximum overshoot is approximately 40.4 $\mu m/s$. Increasing the value of the maximum allowable overshoot to the limit of the $6^{th}$ order model accuracy (from 1 mm to 1.7 mm) only increases the ideal maximum tolerable velocity by 20% (from $\sim 40$ $\mu m/s$ to $\sim 48$ $\mu m/s$). A plot of the maximum velocity dependence on the displacement limit is shown in figure 5.9. Since the dependence is similar to a square root, it is clear that, beyond a certain value of the displacement limit, the increase of allowable release velocity is of small importance when compared to side effects like model uncertainties.

### 5.2.1 Controller Performance Indices

The derived “ideal” limit release velocity for 1 mm displacement is used as the 100% performance level, and the ratios between simulation results and the computed value are calculated to assess the performance levels of the controllers.

- **Linear controller**, 15 $\mu m/s$ saturation limit: 37% of ideal limit;
- **Nonlinear controller**, 39 $\mu m/s$ maximum overshoot limit: 96.5% of ideal limit.

The remaining 3.5% discrepancy between the ideal limit and the nonlinear controller performance is due to imperfections of the simulation run, mainly the non-instantaneous

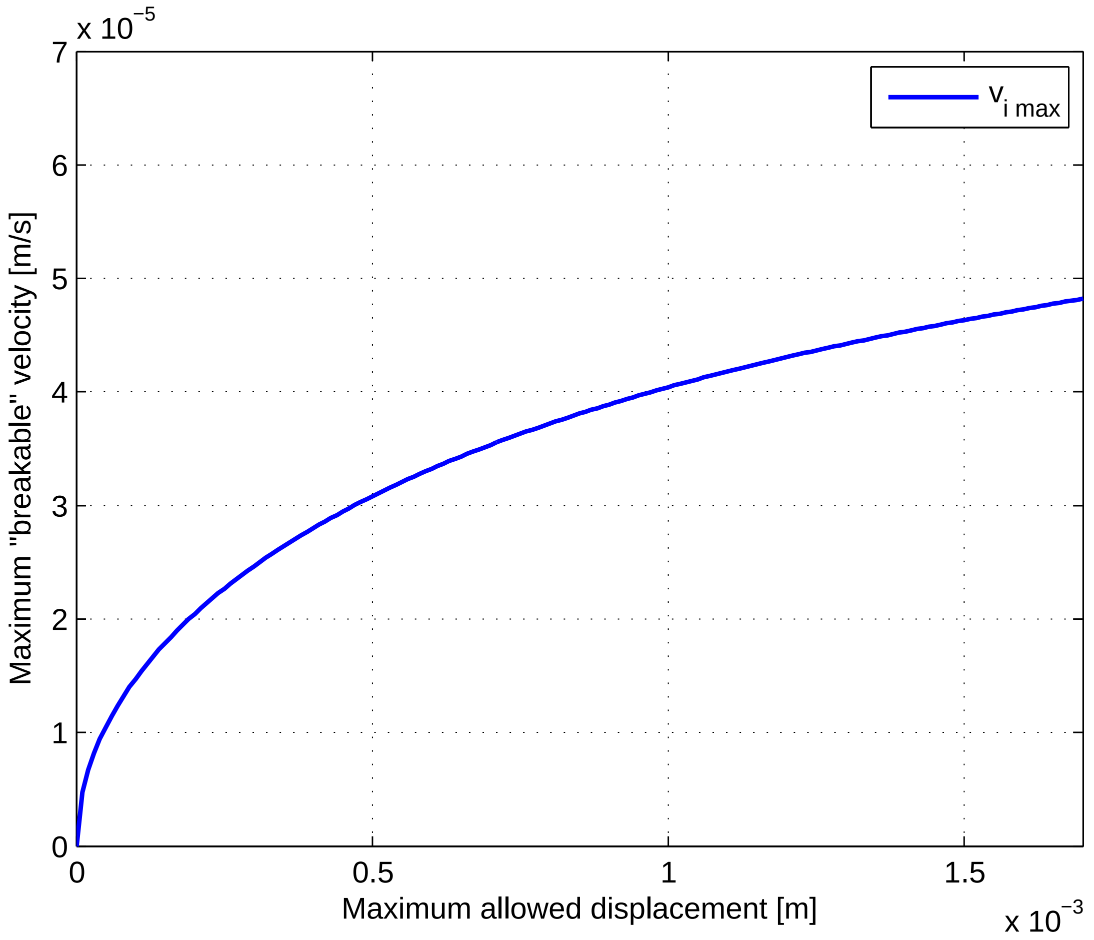


FIGURE 5.9: Maximum tolerable release velocity versus maximum displacement limit

command application (there is some fraction of a second delay before the command is applied, caused by issues in simulator implementation) and imperfection in the maximum force voltage calculation (i.e. sometimes a voltage slightly smaller than 130.1 V is applied).

For comparison purposes, a similar test has been carried out with the most recent version of the LISA Pathfinder Sliding Mode Controller. This test resulted in the TM reaching the maximum overshoot limit (1mm) for a release velocity of about 15.5 $\mu m/s$, corresponding to 38% of the ideal limit. The existing Sliding Mode design shows then performances equivalent to the selected best linear controller. However, it should be noted that the two controllers reach their limits because of different reasons:

- The linear controller meets its limit due to saturation, while still providing a relatively small overshoot;
- The Sliding Mode controller meets its limit due to reaching the prescribed overshoot limit, while still commanding a force smaller than its design saturation limits.

The low value of the linear controller maximum tolerable release velocity is caused by the fact that its tuning was carried out by assuming as worst case initial conditions the ones defined in section 2.3.5.1. An increase in release initial conditions value quickly causes the controller to saturate.

The final result of the controller performance evaluation is that when compared on a pure “initial velocity stop” ground, the new VGS controller is able to exploit the existing hardware up to 96.5% of its physical limit: 2.5 times the value achieved by the existing Sliding Mode controller.

# Chapter 6

# Overall Control Strategy

In this chapter, the control strategy for all the degrees of freedom is described. Results of the verification phase using the LISA Pathfinder End-to-End simulator are presented, together with comparison versus the existing design.

## 6.1 Description of Strategy and Justification

### 6.1.1 Strategy

The adopted control strategy is not the same for all the test mass degrees of freedom. In fact, the Nonlinear controller is adopted only for the $z/\eta$ couple, all the other degrees of freedom being controlled simply with the LQG controller. The summary of all degrees of freedom controllers' characteristics is given:

- For the x and y degree of freedom, the LQG controller is adopted. The tuning is carried out adopting a k parameter of 0.5.
- For the $\theta$ and $\phi$ degree of freedom, the LQG controller is adopted. The tuning is carried out adopting a k parameter of 0.6.
- For the z degree of freedom, the Nonlinear switching controller is adopted. When operating in the linear regime, the LQG controller is adopted. The tuning has been carried out to allow the maximum possible breaking distance while avoiding saturation. To do so, the $x_{max}$ parameter has been set to the 1.7 mm limit, and the k parameter value has been chosen as 1. Doing so results in a significantly slower linear regime with respect to the previously presented results. However, in this

design phase the exploitation of the velocity breaking controller to its maximum limits was deemed more important.

- For the $\eta$ degree of freedom, the LQG controller is adopted. Two sets of gains are implemented, and the used one is chosen on the basis of the output from the z controller. The regular set of gains is derived by tuning the controller using a k parameter of 0.6. The reduced set of gains is derived by tuning the controller using a k parameter of 1, but reducing the $u_{max}$ value to $7.23 \cdot 10^{-6} rad/sec^2$ , corresponding to the chosen torque maximum limit for force maximization.

### 6.1.2 Justification of Strategy

The reason for using different control strategy is that the realistic operative conditions are expected to be different for the three axes [15]. Moreover, the size of the electrodes is different for the various DoF, leading to different maximum forces (the smallest one being on the $z$ DoF). A more realistic assessment of the TM velocities after release with respect to the requirements specified in [8], is carried out in [15], and its main results are:

- The estimated worst case $z$ release velocity is $3.37 \mu m/s$;
- The estimated $x$ and $y$ release velocities caused by a 2 mrad plunger angle at release are 7 nm/s;
- The estimated worst case angular velocities caused by a 2 mrad plunger angle and 200 $\mu m$ misalignment are 3.6 $\mu rad/s$.

The most important result concerning the definition of the control strategy is that the release velocity along $z$ is estimated to be about 500 times larger than the ones on $x$ and $y$. When taking into account the increased complexity introduced by the nonlinear strategy, the adoption of the velocity breaking controller for those degrees of freedom is not reasonable. Similar considerations hold for the rotational degrees of freedom, where the release velocity estimates are very low, and the actuation authority available in the linear regime is more than sufficient to effectively control them.

## 6.2 Verification

The newly defined complete controller was implemented in the LISA Pathfinder End-to-End simulator, and its performance was tested and compared to the existing sliding mode and zero order actuation algorithm design, for various test cases. The results of the testing phase are summarized below.

### 6.2.1 Nominal Run

The first test case was the nominal run. The nominal conditions are defined as:

- All initial conditions as given in section 2.3.5.2;
- DC disturbances generated by spacecraft dynamics, solar pressure (undercompensated by the spacecraft in an open-loop way, with a 20% knowledge error) and an additional term (19.6 nN) acting directly on the test masses.

The time plots for the TM1 quantities of interest are presented. For each quantity, first the existing SLM design is shown, followed by the new controller case.
All displacement and velocity plots show an imperfection for times immediately following test mass release. This effect is caused by the settling of an anti-aliasing filter from which the output data is collected.

#### 6.2.1.1 Displacements and Attitudes

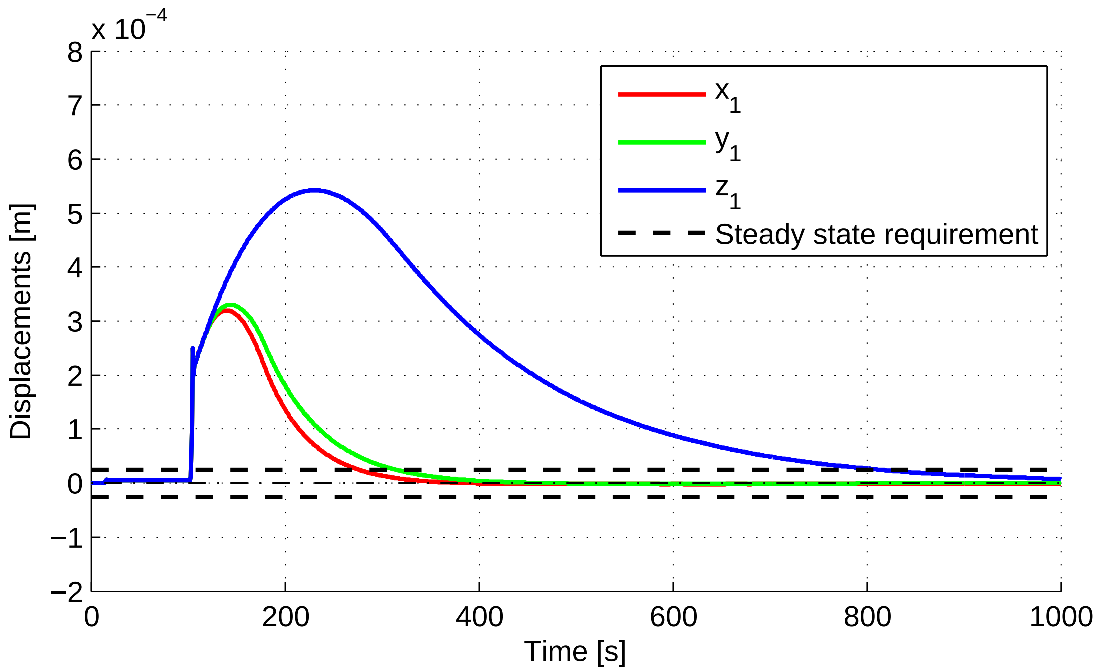


FIGURE 6.1: Sliding Mode Controller nominal run Displacements

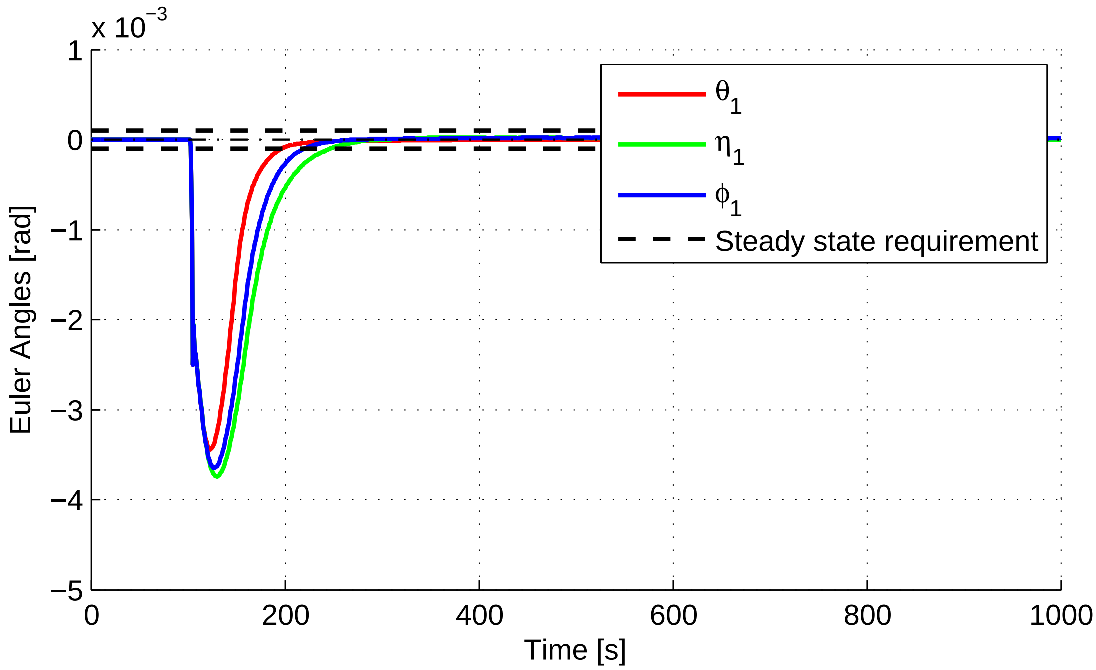


FIGURE 6.2: Sliding Mode Controller nominal run Angles

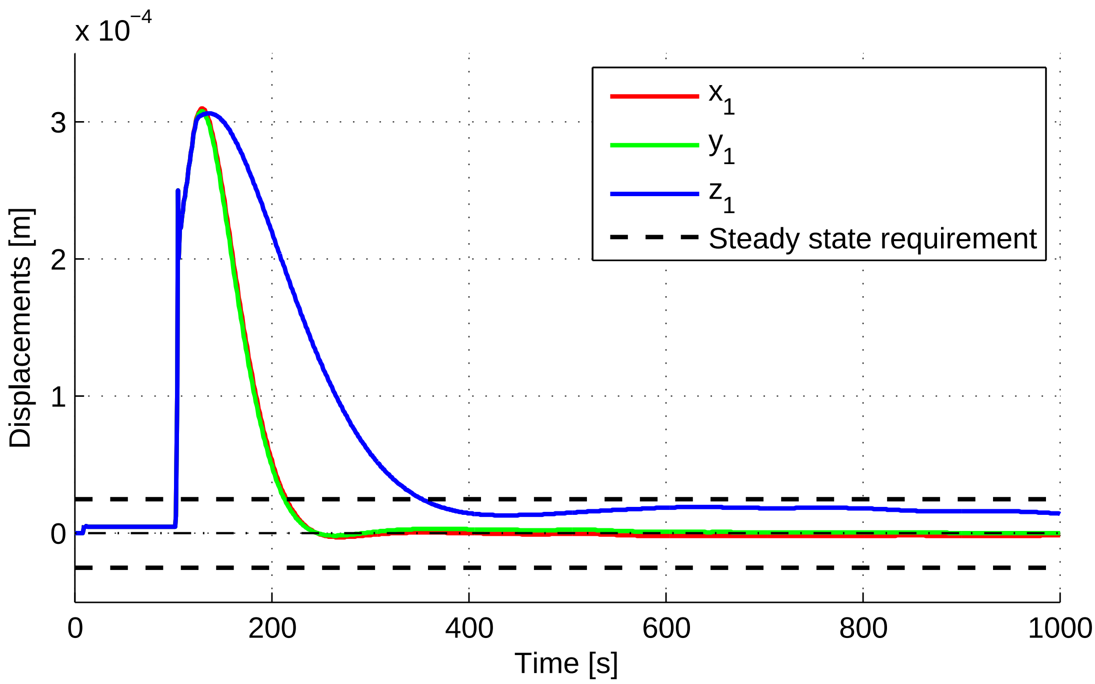


FIGURE 6.3: Switching Controller nominal run Displacements

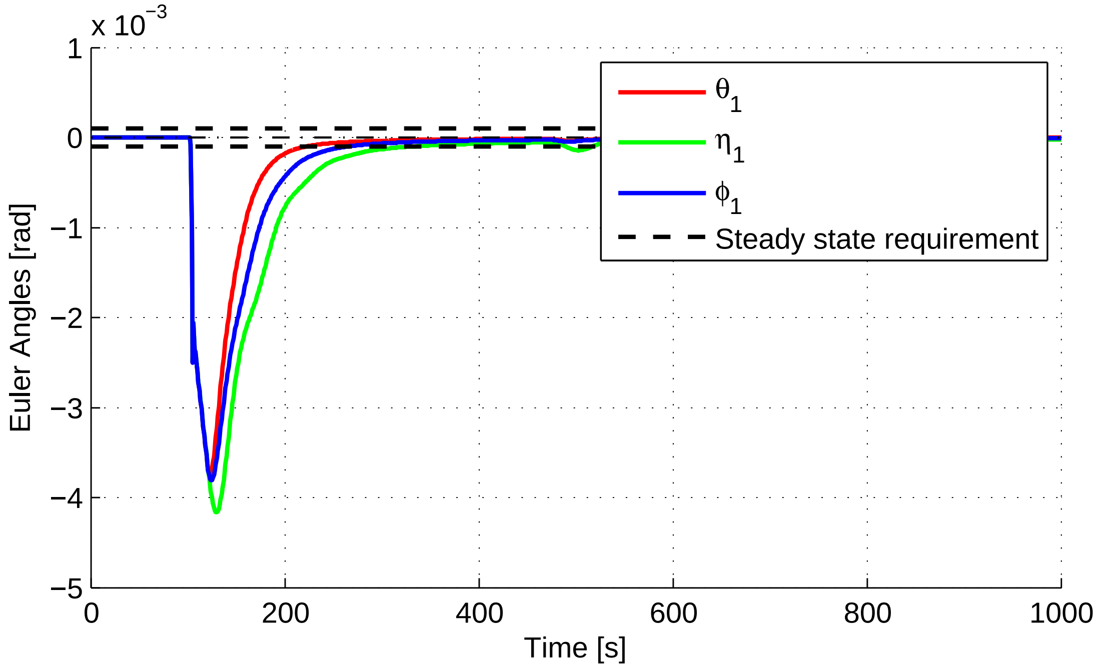


FIGURE 6.4: Switching Controller nominal run Angles

#### 6.2.1.2 Velocities and Rates

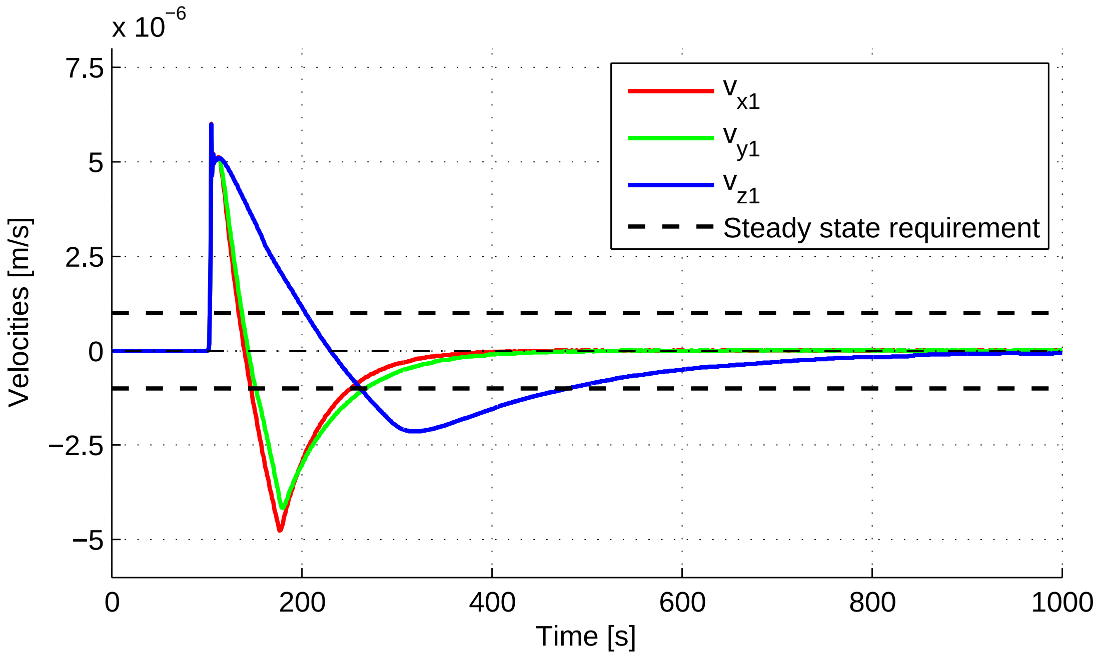


FIGURE 6.5: Sliding Mode Controller nominal run Velocities

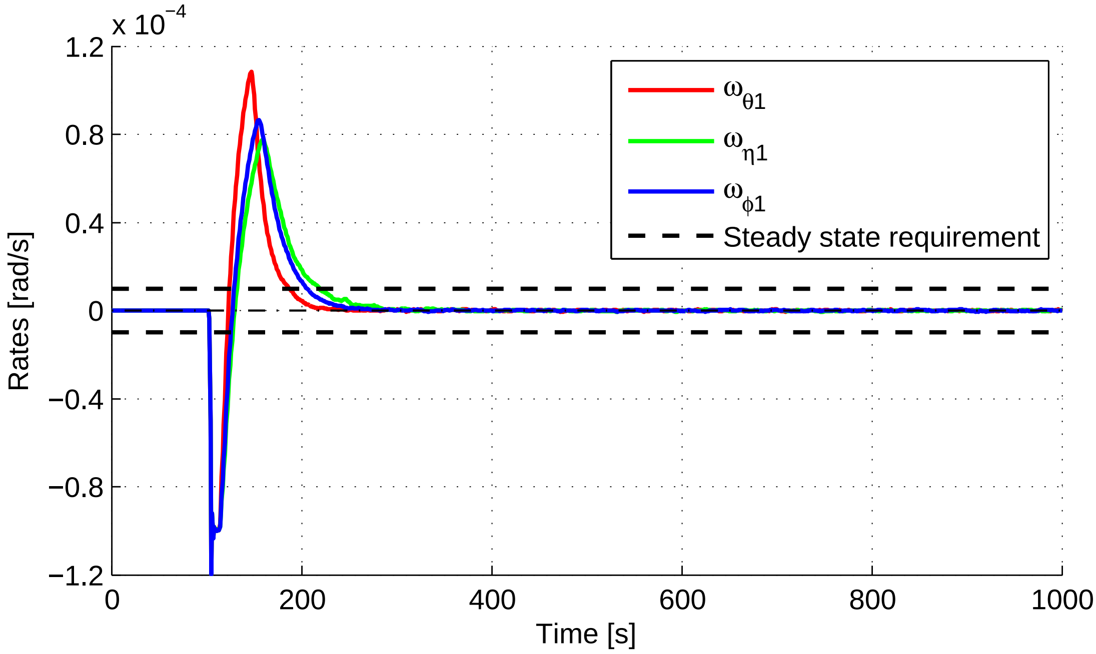


FIGURE 6.6: Sliding Mode Controller nominal run Rates

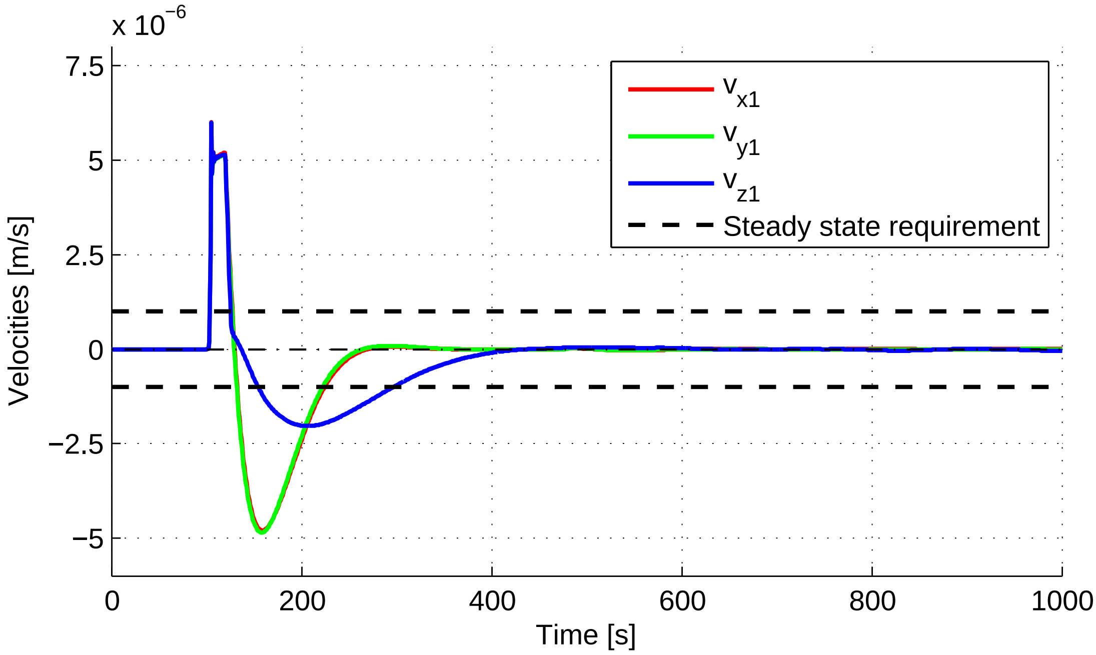


FIGURE 6.7: Switching Controller nominal run Velocities

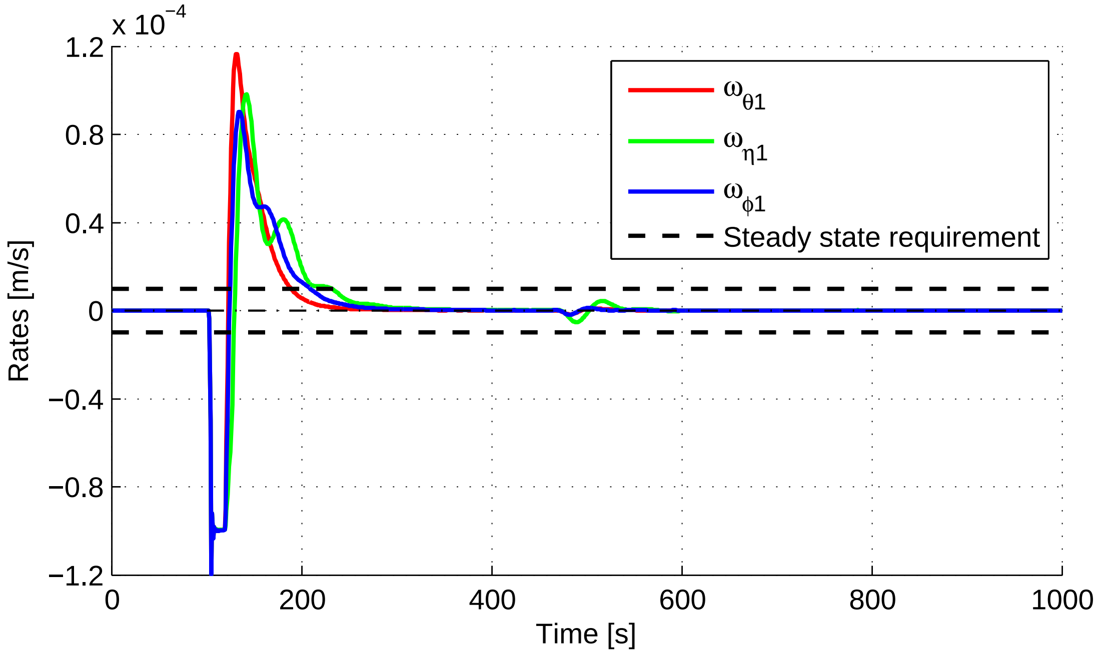


Figure 6.8: Switching Controller nominal run Rates

#### 6.2.1.3 Forces and Torques

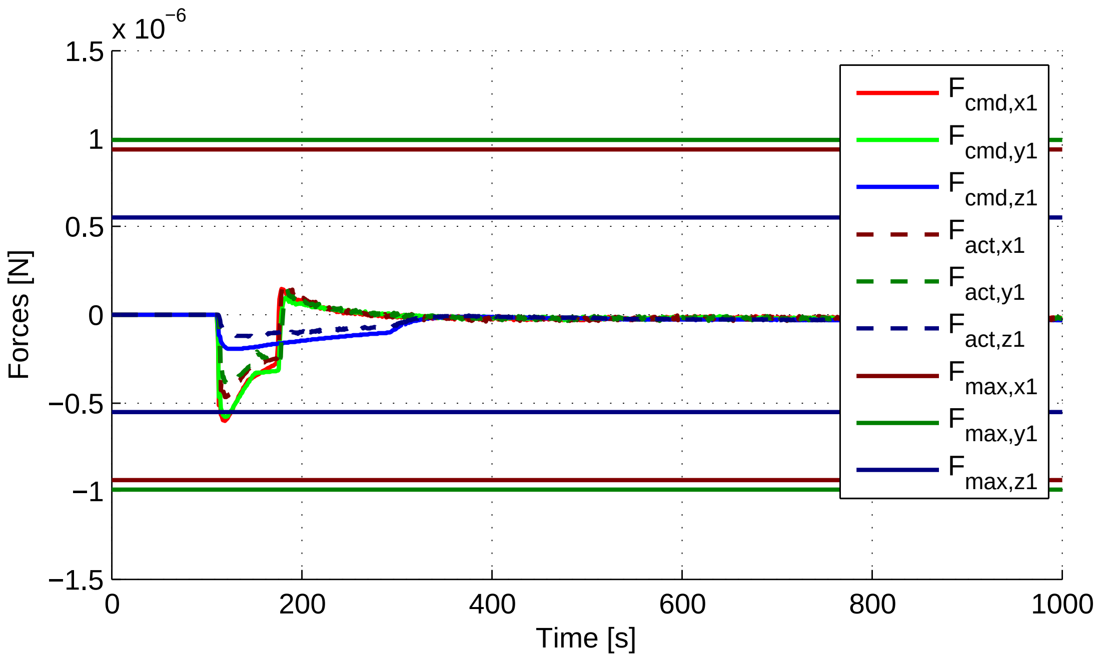


Figure 6.9: Sliding Mode Controller nominal run Forces

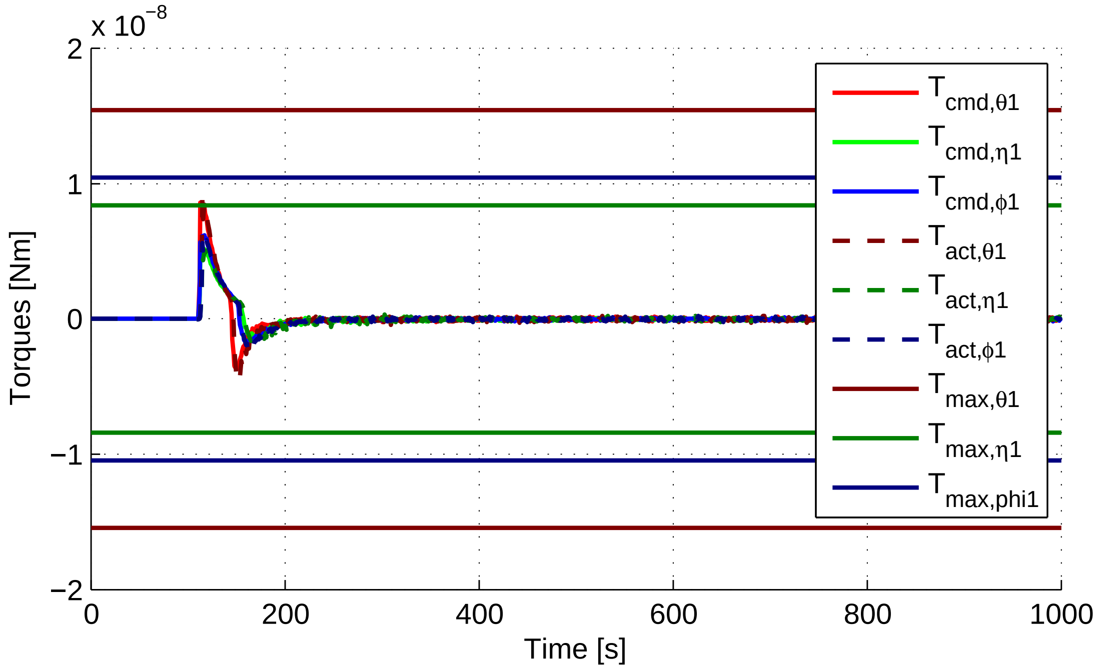


FIGURE 6.10: Sliding Mode Controller nominal run Torques

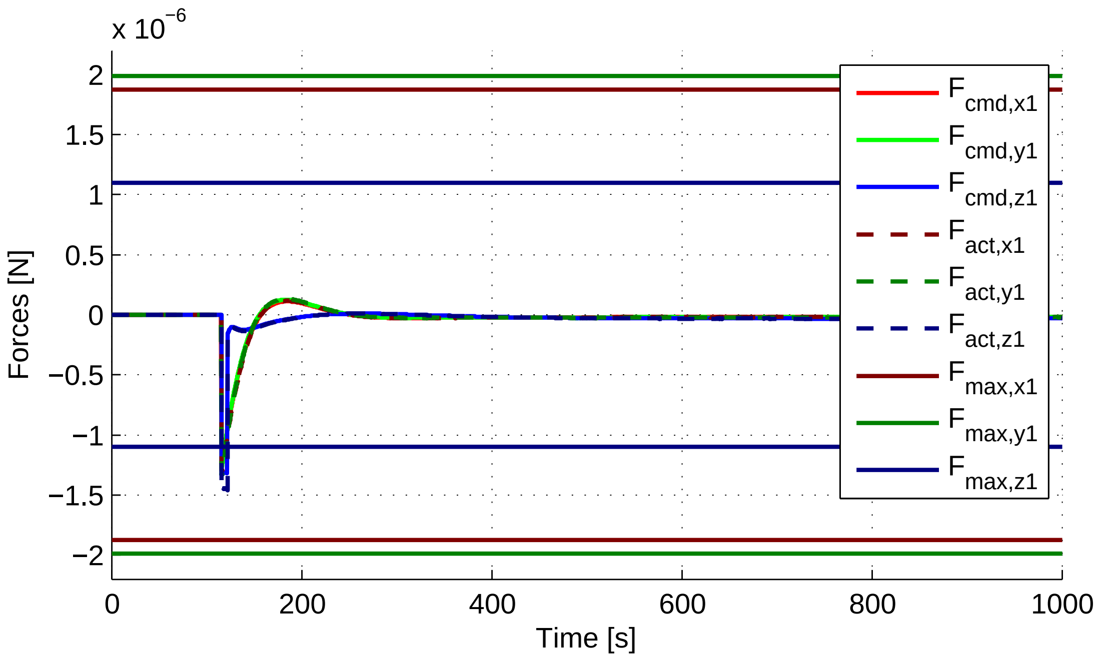


FIGURE 6.11: Switching Controller nominal run Forces

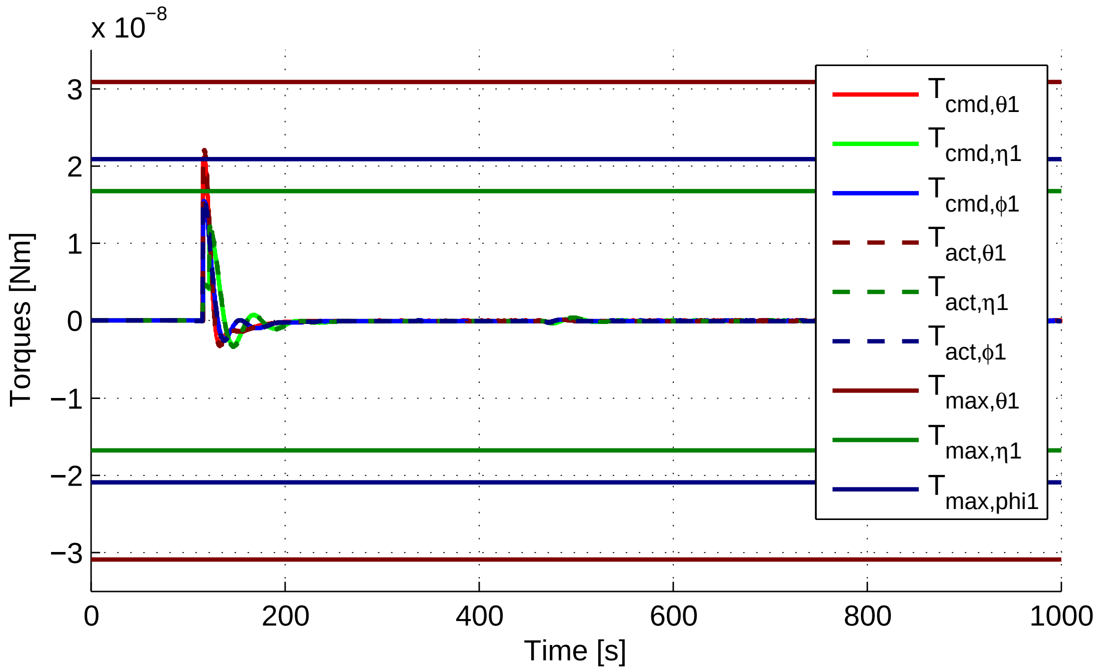


FIGURE 6.12: Switching Controller nominal run Torques

### 6.2.2 Breaking Velocity Limit - Worst Case

The second test case focused on finding the highest value of the initial z velocity for which the controllers' behavior remained inside defined limits:

- The maximum overshoot along z shall be smaller than 1.7 mm (it is shown in Appendix A.2 that beyond this value of z displacement, the $6^{th}$ order model gives unphysical results; for this reason there is no interest in results that show an overshoot above such value);
- The controller shall not cause actuator saturation; this applies equally to the Sliding Mode controller, the LQG controller and the linear regime of the Nonlinear Switching controller;
- The controller shall not become unstable.

For comparison purposes, also the LQG controller has been included in the limit testing, since it offers a much simpler design possibility. The test has been carried out adopting worst-case conditions. Initial conditions have been taken as defined in section 2.3.5.2 and the solar pressure compensation by the spacecraft has been deactivated, representing the case of maximum disturbance in the same direction of the initial displacement and velocity; i.e. the worst case for test mass 1.

Figures 6.13, 6.14 and 6.15 show the z displacements, velocities and forces for the limit runs of the three controllers. The results are summarized below:

- The Sliding Mode controller reaches the maximum overshoot limit of 1.7mm for a release velocity of 11.9 $\mu m/s$, without incurring in saturation. Since the main design goal of the Sliding Mode controller is to avoid saturation, it can be stated that it reaches its full limit.
- The Linear LQG controller incurs in saturation for a release velocity of 7 $\mu m/s$, reaching an overshoot of less than 0.5mm. This is due to the fact that its tuning was carried out for a worst case corresponding to the nominal release scenario, therefore it quickly saturates in a more demanding situation;
- The Nonlinear switching controller meets the prescribed maximum overshoot limit for a release velocity of 28.5 µm/s.

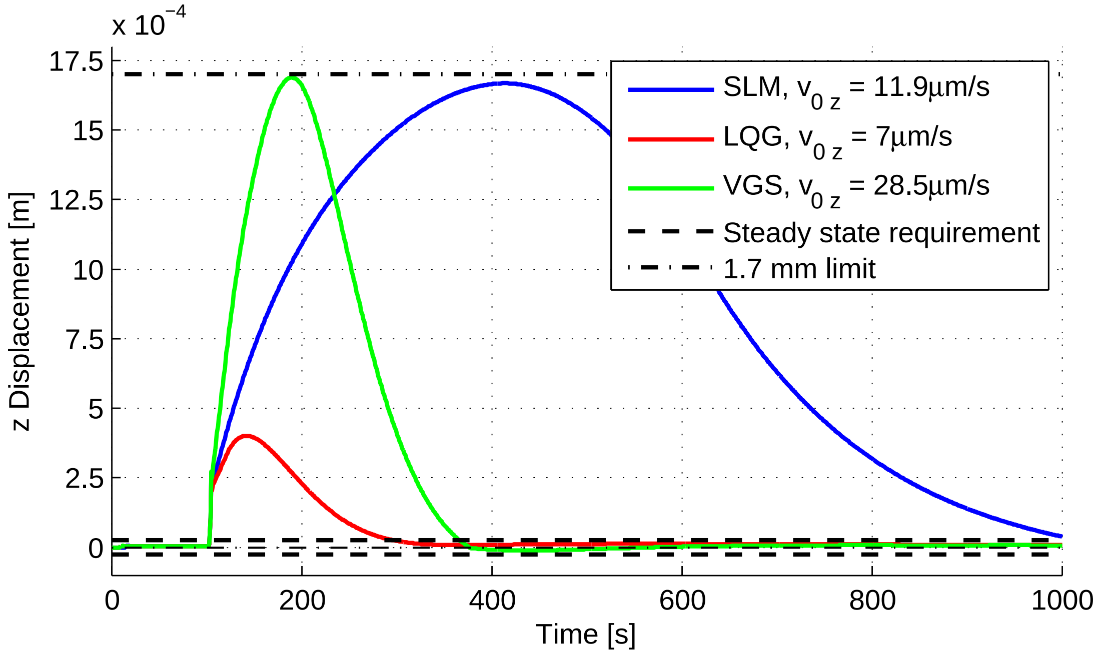


FIGURE 6.13: Worst Case release velocity limit, displacements

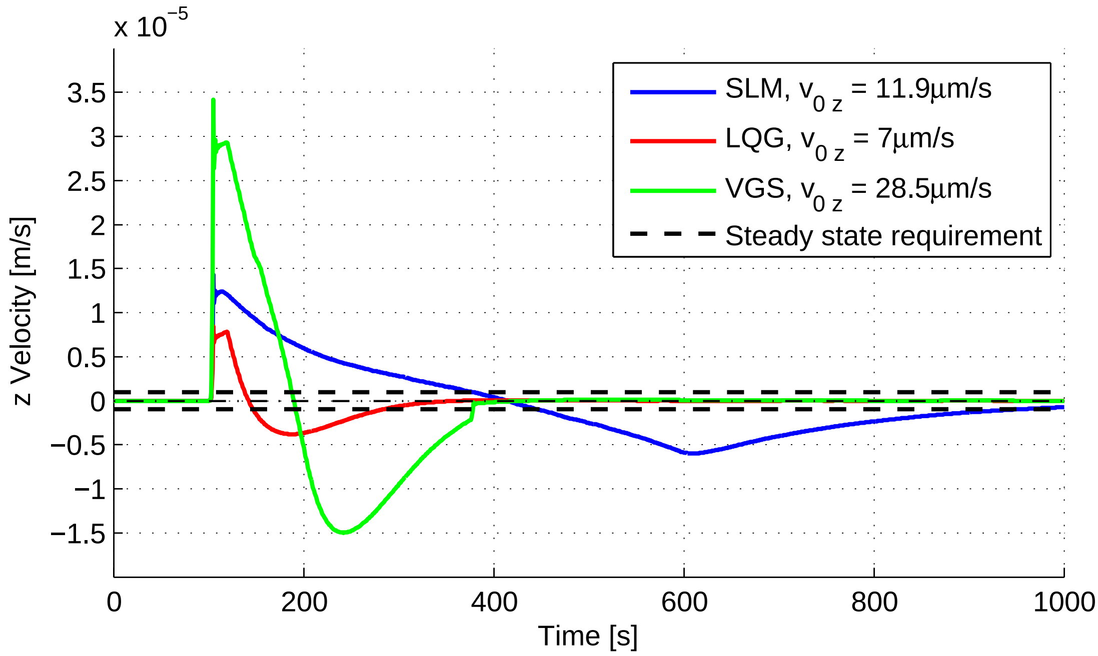


FIGURE 6.14: Worst Case release velocity limit, velocities

As can be seen in figure 6.15, the nonlinear switching controller shows issues in the generation of the maximum possible force. This is caused by the use of a first order capacitance model in the maximum force actuation algorithm, which for big displacements can lead to incorrect solution picking, causing the generation of a sub-optimal output force, and a significant torque error.

In figure 6.15 a second activation of the velocity breaking controller can be seen (shortly before the 400 s mark). This can be explained by looking at figures 6.13 and 6.14. In that particular time instant, the displacement changes sign (from positive to negative) while the velocity is still negative, with a value greater than the design threshold. The velocity breaking controller then uses the maximum force to prevent the test mass displacement from increasing, avoiding the negative overshoot that a simple linear controller would cause.

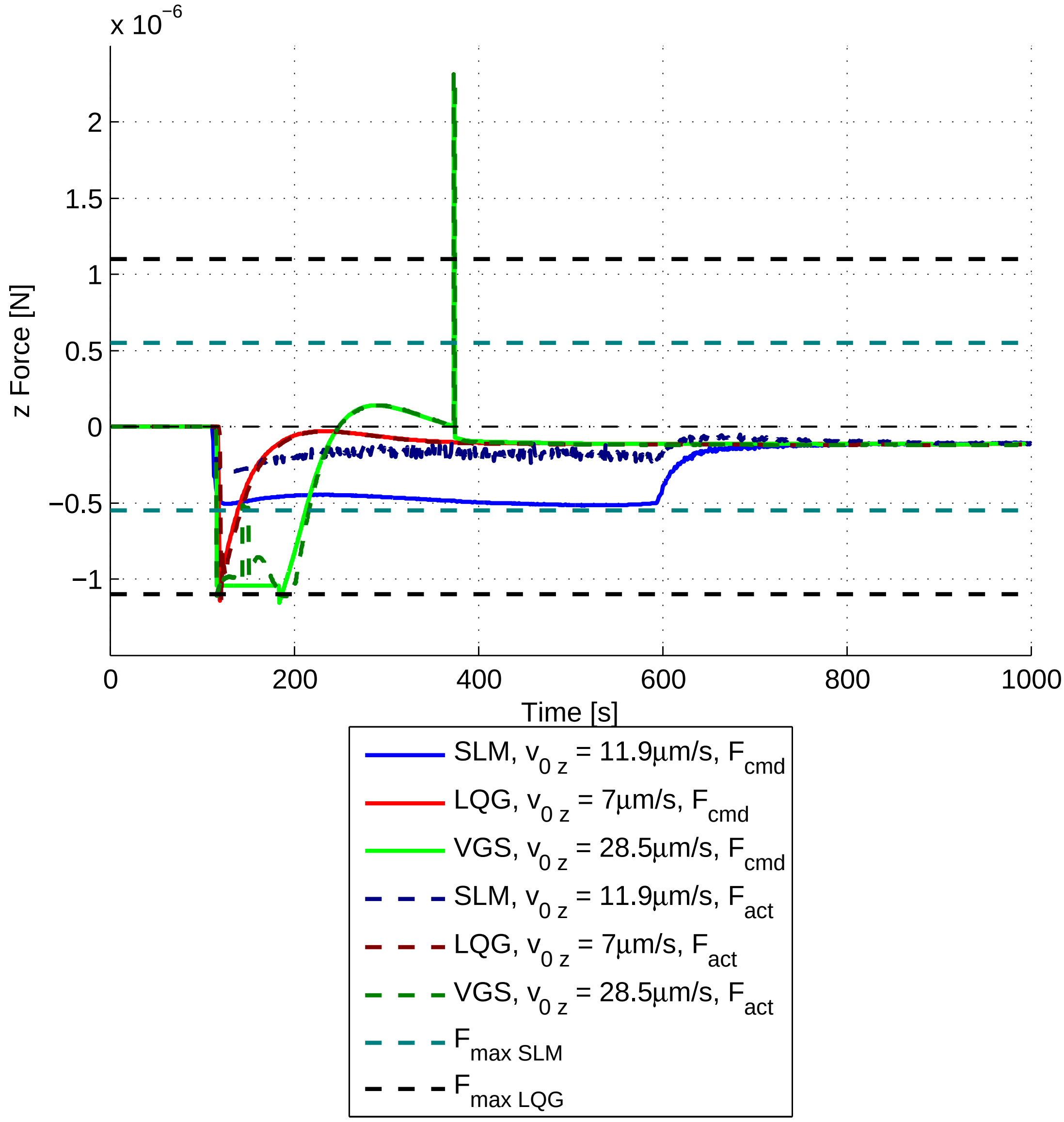


FIGURE 6.15: Worst Case release velocity limit, forces

### 6.2.3 Breaking Velocity Limit - Realistic Case

The third test case focused on finding the highest value of the initial z velocity for which the controllers behavior remained inside the limits already defined for the previous case, for the realistic release conditions derived in [15].

According to [15], all initial velocities (except for the z axis) have been set to the values defined in section 6.1.2 of the present chapter. Since no LISA Pathfinder flight model realistic test mass measurements are available yet, all initial displacements have been set according to the requirement values. Open-loop compensation of the solar radiation pressure has been employed, with a 20% underestimation error.

Figures 6.16, 6.17 and 6.18 show the z displacements, velocities and forces for the limit runs of the three controllers. The results are qualitatively equivalent to the worst case testing, with the final values of limit velocities being pushed up a bit by the more favorable conditions.

- The Sliding Mode controller reaches the maximum overshoot limit of 1.7 mm for a release velocity of 12.5 $\mu m/s$, without incurring in saturation;
- The Linear LQG controller incurs in saturation for a release velocity of 10 $\mu m/s$, reaching an overshoot of less than 0.5 mm. The same considerations of the worst case on the controller limit are valid in this case;
- The Nonlinear switching controller meets the prescribed maximum overshoot limit for a release velocity of 33 $\mu m/s$.

The very long convergence time of the Nonlinear switching controller, when operating in its linear regime, is caused by the very slow tuning that was carried out to avoid high displacements saturation.

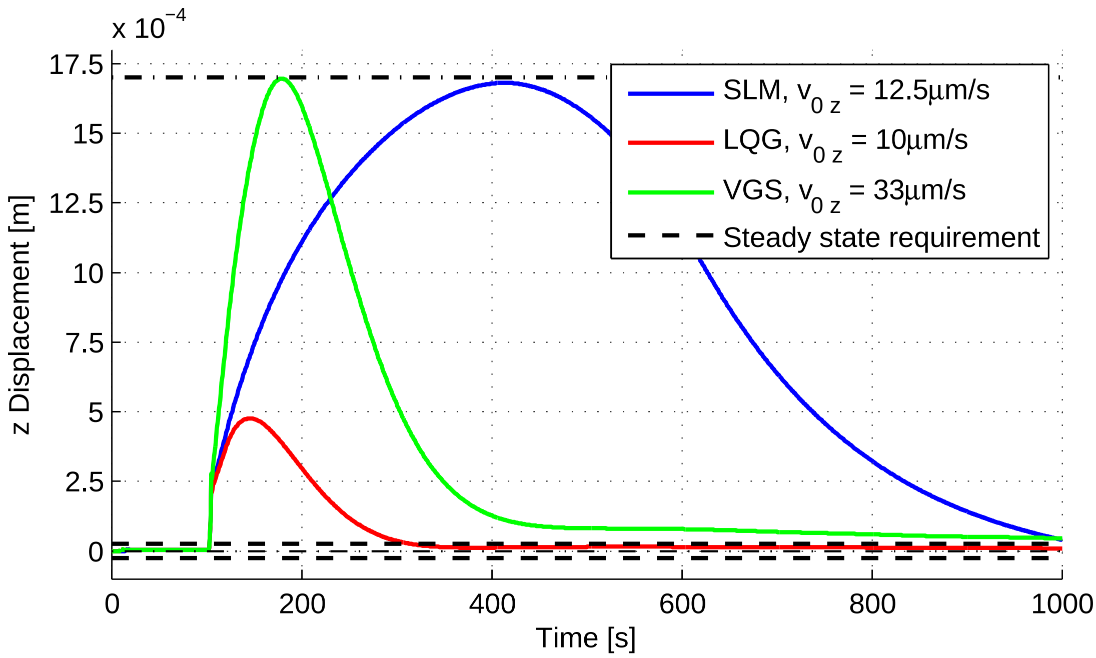


FIGURE 6.16: Realistic Case release velocity limit, displacements

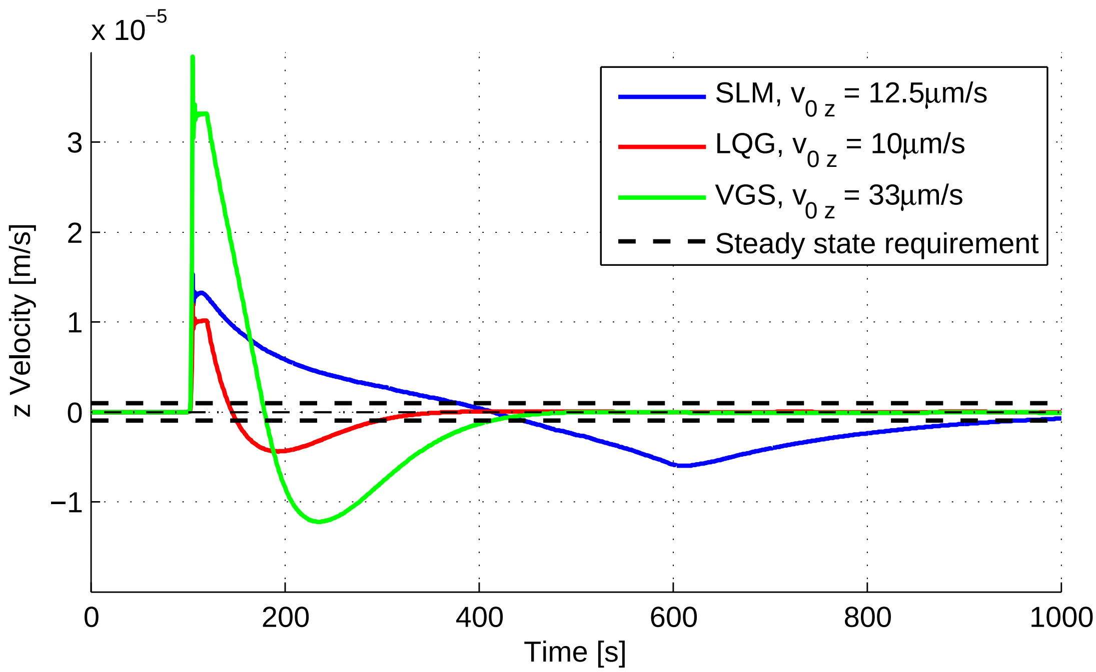


FIGURE 6.17: Realistic Case release velocity limit, velocities

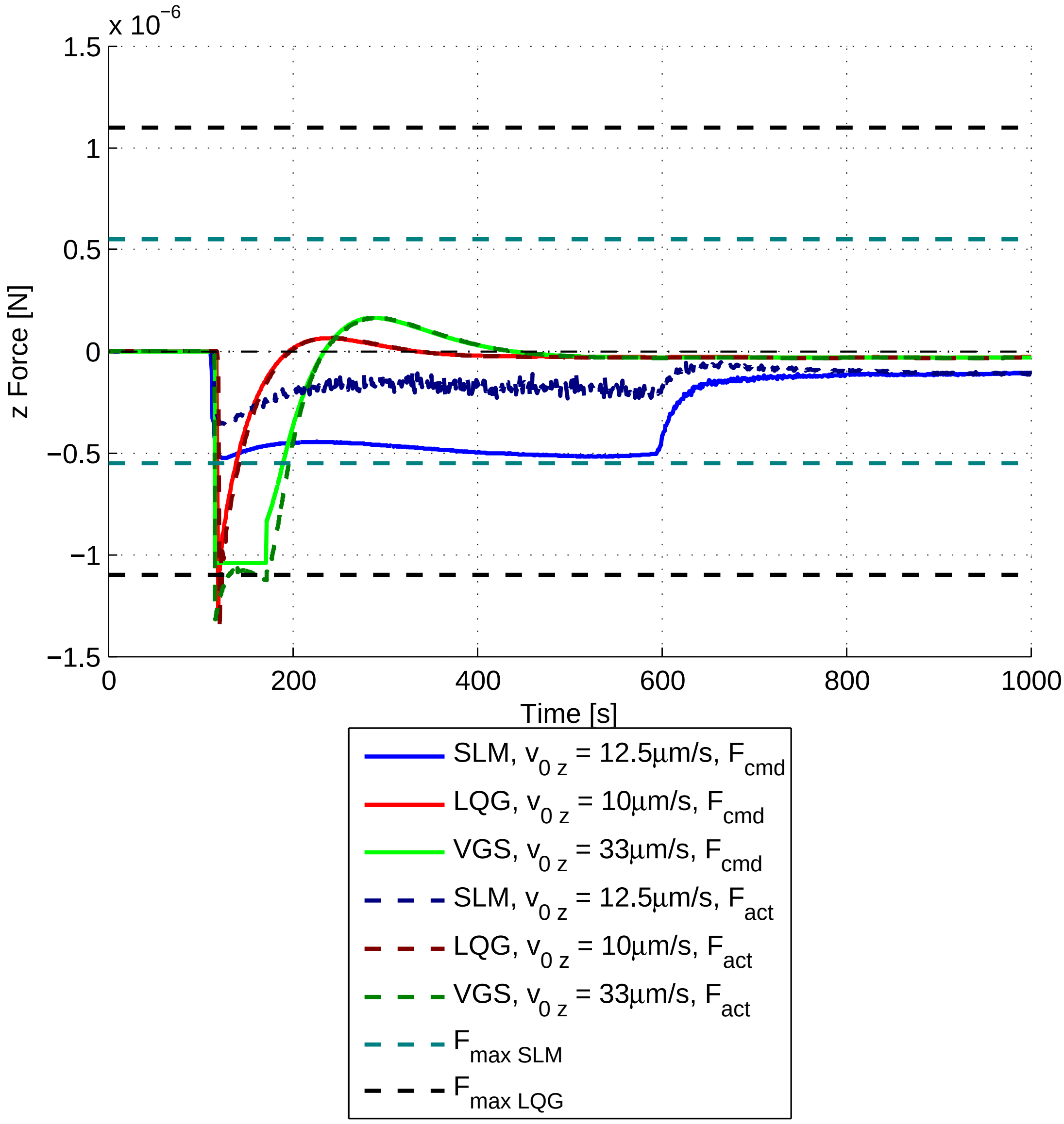


Figure 6.18: Realistic Case release velocity limit, forces

### 6.2.4 Test Mass Charge Limit

The third test case focused on finding the highest value of the TM charge for which the controllers behavior remained inside the limits already defined for the previous cases. As can be verified by looking at equations 2.4 and 2.8, the presence of a charge on the TM causes one of the assumptions behind the actuation algorithm to be not satisfied; therefore introducing an error in the actuated force. Such force error causes the controller to act incorrectly, eventually leading to either overshoot limits, saturation, or instability. Please note that, while the plots are shown only for the z degree of freedom, (due to its different behavior in the Nonlinear controller) this test does not privilege one axis with respect to the others; a prescribed limit could be met on any of the degrees of freedom.

The test has been carried out adopting nominal conditions, and increasing the value of the test mass charge. Figures 6.19, 6.20 and 6.21 show the z displacements, velocities and forces for the last successful runs of the three controllers. The results are summarized here:

- The Sliding Mode controller becomes unstable for a test mass initial voltage higher than 11 V;
- The Linear LQG controller starts saturating for a test mass initial voltage of approximately 30 V;
- The Nonlinear switching controller starts saturating (on its $x$ and $y$ axes) for a test mass voltage of approximately 30V. This is obvious since the controllers for the degrees of freedom different from $z$ and $\eta$ are just the LQG ones. Additionally, for a voltage of 30V, we start observing the $z$ velocity breaking controller being switched on and off multiple times, due to the actuation error causing an undesired increase in the $z$ velocity. For this reason, the 30V voltage level can be assumed as well the limit for the velocity breaking controller.

Figure 6.22 shows a particular of figure 6.21 to highlight the force generation errors. The influence of the test mass charge is particularly easy to recognize, as an actuated force can be seen as soon as the test mass is released (100 seconds mark) before a command signal is produced by the controllers.

The great difference in tolerable test mass voltage is probably due to the greater error introduced by the zero order actuation algorithm [2]. Further investigation should be done on the effects of a test mass voltage in the force generation using the two different algorithms [2] and [7].

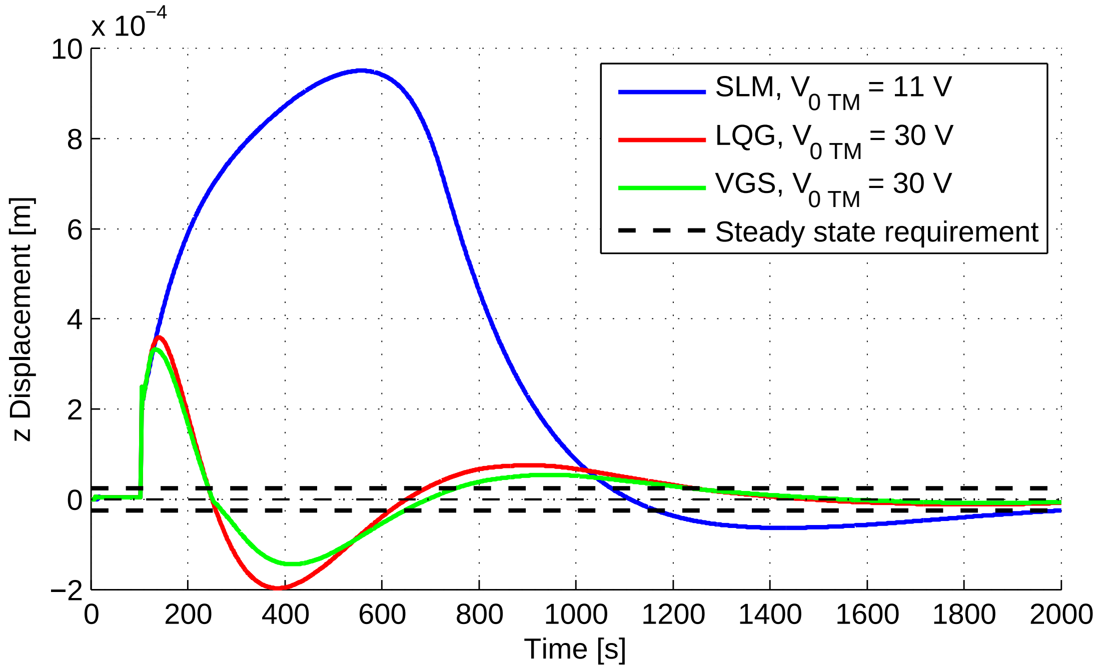


FIGURE 6.19: Test Mass charge limit, displacements

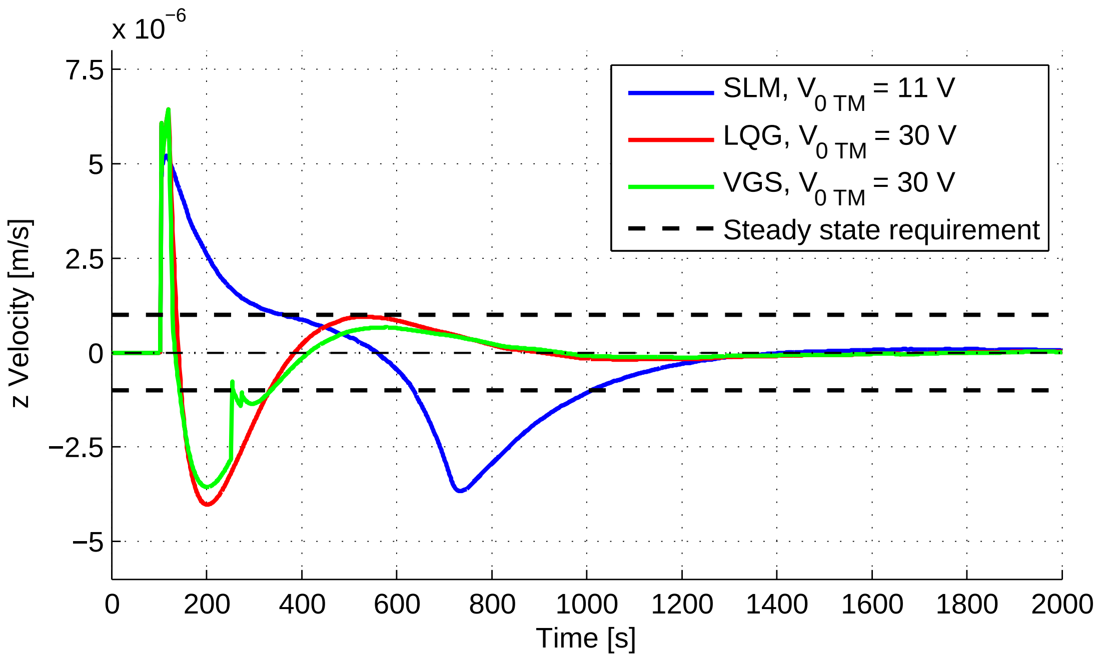


FIGURE 6.20: Test Mass charge limit, velocities

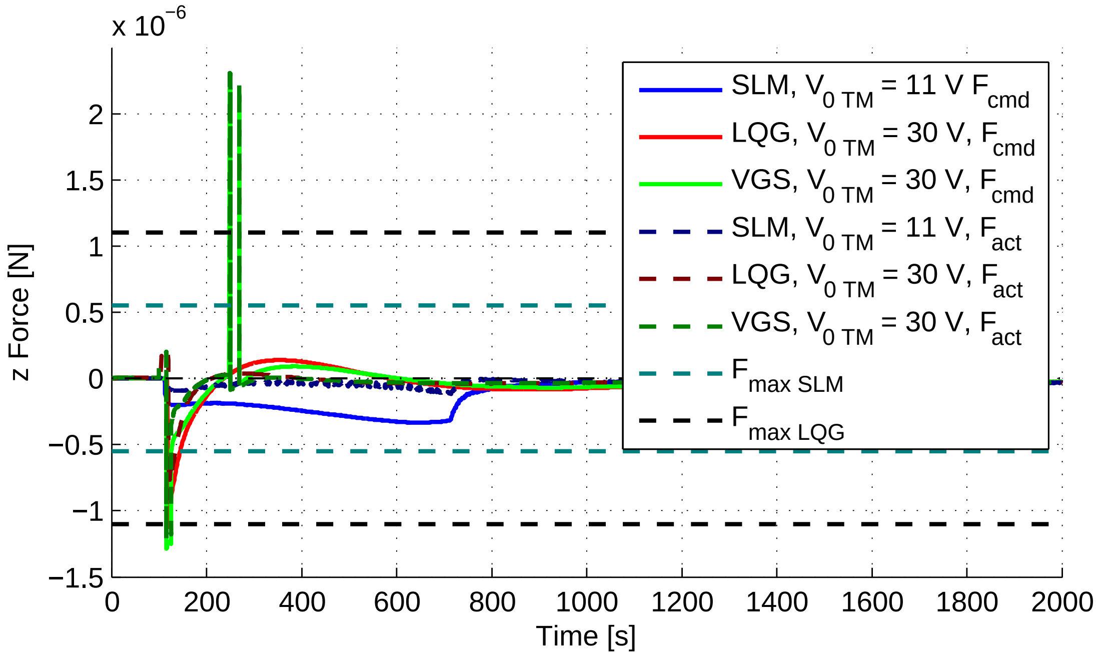


FIGURE 6.21: Test mass charge limit, forces

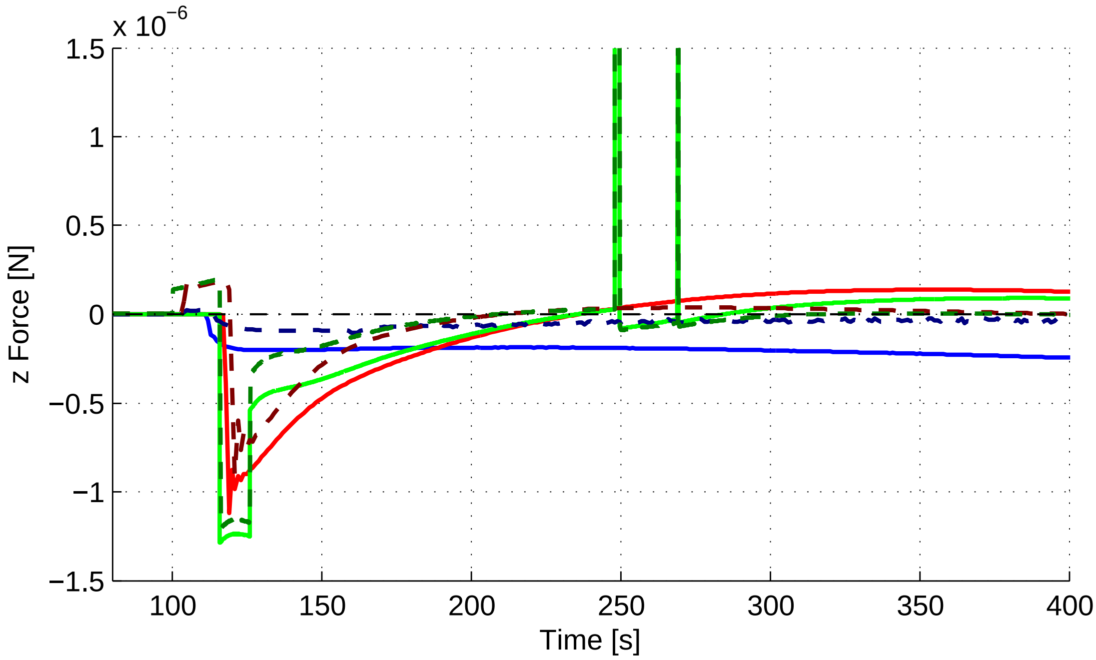


FIGURE 6.22: Test mass charge limit, forces, particular

## 6.3 Operational Limits of Investigated Control Strategies

The limits of the various controllers operating conditions, explored in the previous section, are summarized below.

The Sliding Mode controller is limited mainly by the chosen maximum overshoot value (1.7 mm for the tests of section 6.2). Its maximum tolerable release velocity for worst case conditions has been assessed to be 11.9 $\mu m/s$. Its maximum tolerable release velocity for realistic case conditions has been assessed to be 12.5 $\mu m/s$. The controller has been found to become unstable if a charge is present on the test mass, corresponding to a voltage higher than 11 V.

The LQG controller is limited mainly by saturation, due to its design point tuning. Its maximum tolerable release velocity for worst case conditions has been assessed to be 7 $\mu m/s$. Its maximum tolerable release velocity for realistic case conditions has been assessed to be 10 $\mu m/s$. The controller has been found to saturate if a charge is present on the test mass, corresponding to a voltage higher than 30 V.

The Nonlinear switching controller is limited mainly by the by the chosen maximum overshoot value (1.7 mm for the tests of section 6.2). Its maximum tolerable release velocity for worst case conditions has been assessed to be 28.5 $\mu m/s$. Its maximum tolerable release velocity for realistic case conditions has been assessed to be 33 $\mu m/s$. The controller has been found to saturate and display undesired switching behavior if a charge is present on the test mass, resulting in a voltage higher than 30 V.

# Chapter 7

# Conclusions

The presented work focused on the development of a control strategy to achieve the best possible test mass catching performances, within the constraints given by the Inertial Sensor Front End Electronics (maximum electrode voltages of 130.1 V) and the geometric characteristics of the Inertial Sensor.

In order to find such a controller, an investigation of the limits of linear control has been performed which led to a solid design of an LQG controller.
A more complex nonlinear controller was then developed to maximize the test mass release velocity breaking performance. The foundation of the new concept was a bang-bang velocity controller whose force amplitude was not defined a-priori, but computed online based on position measurements. In order to realize the newly proposed concept, the existing actuation algorithm [7] was modified to include the possibility to generate the maximum possible force of a given sign, for the measured test mass displacements and required torque command.
The resulting control strategy was shown to be able to exploit the system electrostatic actuation up to 96.5% of its physical limit: 2.5 times the value achieved by the current design.

A complete control strategy was designed for the whole system, by combining the linear LQG controller and the nonlinear test mass release velocity breaking controller, as a mean to bring the mass back to the zero position. Test runs performed with the LISA Pathfinder End-to-End simulator essentially confirmed the expected performance improvements.

Given the following release scenario, as defined in the LISA Pathfinder test mass release requirements [8]:

- 200 $\mu m$ initial linear displacements, 5 $\mu m/s$ initial linear velocities,(same signs);

- 2 $mrad$ initial rotational displacements, 100 $\mu rad/s$ initial rotational velocities, (same signs);
- Disturbance forces and torques acting with same sign as displacements and velocities;
- Solar radiation pressure acting on the spacecraft (translating into a disturbance on the test mass along the z axis) being compensated by thrusters assuming a 20% underestimation error;

The new controller maximum overshoot along the most critical axis (z) was reduced to less than half the value obtained using the existing control strategy (from approximately 650 $\mu m$ to 300 $\mu m$).

For the realistic release scenario (where the $x$ and $y$ velocities are reduced to 10 $nm/s$ and the rotational rates to 5 $\mu rad/s$) the new control strategy can cope with a release velocity along $z$ of 33 $\mu m/s$ (compared to 12.5 $\mu m/s$ of the sliding mode).

For a worst case scenario, defined as the nominal scenario with no solar pressure compensation, an improvement of the maximum release velocity from 11.9 $\mu m/s$ to 28.5 $\mu m/s$ has been achieved.

Such improvements allow for a relaxation of the maximum release velocity requirements on z by a factor of more than 5, opening the possibility to reduce hardware verification costs and difficulties.

From a more general perspective, the interesting case of finding the controller which most effectively exploits the available system hardware has been studied. From a stability point of view, the application of a bang-bang controller to first order systems represents the solution with highest possible robustness (the system cannot perform better than its maximum).

# Chapter 8

# Outlook

Further investigation could comprise the following three aspects:

- The maximum force actuation algorithm
- The estimator input errors
- The control law that takes over the control after test mass velocity breaking is complete

The most critical aspect that emerged during the development of the present control strategy has been the modification of the actuation algorithm [7] to obtain the maximum force actuation algorithm. While inverting the linear force model to obtain the required voltages provides sufficiently accurate solutions, using the calculated voltages in the linear model to calculate the corresponding forces suffers from large errors. This feature of the linear model has two negative consequences: the introduction of a significant error in the Kalman filter input, and the possibility of undesired behavior of the algorithm itself. Unfortunately, the use of a higher order model to carry out force computation has been found to be cumbersome and lacking the possibility to use one single set of expressions for all the possible combinations of command signs, typical of the first order one. Further work might focus on the research of a method to efficiently exploit a higher order force model to avoid these issues.

The second important source of imperfection in the proposed control strategy is the presence of errors in the Kalman filter inputs, which are not of pure noisy nature. Kalman filter theory assumes the inputs to be corrupted by zero-mean noise, whereas in the studied case the filter inputs are corrupted by actual errors (i.e. commanded to actuated force and measured to real position), whose influence on the overall uncertainty is greater than the noise influence. The problem has been addressed simply by treating the systematic errors as noise with suitable power within the Kalman filter framework. However, work on the origin of such errors, and possibly the inclusion of a model for them into the filter algorithm might improve estimation performances. In regard to this, addressing the force errors when re-computing the maximum forces from the obtained voltages would already greatly improve filter performances.

Finally, the control law that takes the test mass from its position at complete breaking, back to the nominal position, might be further studied. Currently, a linear controller is used, which is tuned to avoid saturation for the highest occurring final breaking distance. However, this results in a generally slow controller, more so for conditions that do not cause the mass to reach the overshoot limit. A study on an alternative concept, dealing with low initial velocities but possibly very high displacements, could further improve the overall controller performances.

# Appendix A

# System Model Features

## A.1 Test Mass Dynamics

The position vectors for both spacecraft and test mass relative to their purely gravitational motion, in an inertial frame are defined as: $\underline{r}_{TM\,NG}$ and $\underline{r}_{SC\,NG}$. They are obtained by taking the generic position vector defined in an inertial frame, and subtracting from it the position vector corresponding to pure gravitational motion. The example for the spacecraft case is then:

$$\underline{r}_{SC} - \underline{r}_{SC\,G} = \underline{r}_{SC\,NG} \tag{A.1}$$

Where the suffix G stands for "gravitational" and the suffix NG stands for "non-gravitational". As all the following derivation refers to the non-gravitational motion, the NG suffix will be omitted from now on. In figure A.1, a representation of $\underline{r}_{TM}$ and $\underline{r}_{SC}$, and all other defined position vectors is presented. It is assumed that the unperturbed gravitational motion is the same for both the test masses and for the spacecraft. While this is not strictly correct, the actual difference between the two is essentially non-existent, and therefore neglected.
The equations of motion for spacecraft and test mass with respect to their unperturbed gravitational motion, using the above described position vectors are:

$$m\ddot{\underline{r}}_{TM} = \underline{f}_{TM} \tag{A.2}$$

$$M\ddot{\underline{r}}_{SC} = \underline{f}_{SC} \tag{A.3}$$

Where $\underline{f}_{TM}$ and $\underline{f}_{SC}$ represent all non-gravitational forces which are acting on TM and spacecraft, respectively.

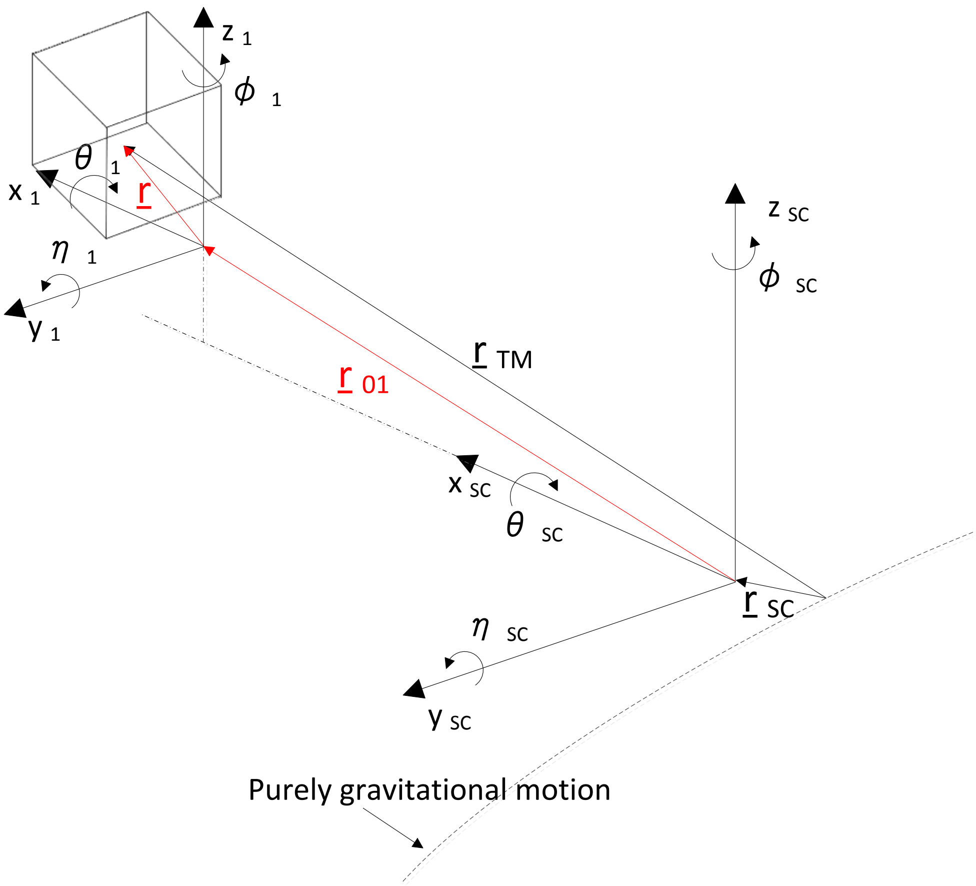


FIGURE A.1: Definition of relevant position vectors and reference frames. In black, position vectors in inertial reference frames; in red, position vectors in rotating reference frames

The $\underline{r}_{01}$ vector is defined as the position vector of the test mass housing centre (corresponding to test mass nominal position) in a spacecraft fixed reference frame centred in spacecraft centre of gravity.
The $\underline{r}$ vector is defined as the position vector of the test mass centre of gravity with respect to the housing centre (nominal position) in a spacecraft fixed reference frame centred in the housing centre.
Please note that all the spacecraft fixed reference frames rotate with angular velocity $\underline{\omega}_{SC}$. With these definitions, the following relation holds between the various vectors:

$$\underline{r} = \underline{r}_{TM} - \underline{r}_{SC} - \underline{r}_{01} \tag{A.4}$$

In order to obtain the equations describing the relative motion between test mass and spacecraft, equation A.4 is differentiated twice with respect to time to obtain:

$$\begin{aligned} \ddot{\underline{r}} + 2\underline{\omega}_{SC} \times \dot{\underline{r}} + \dot{\underline{\omega}}_{SC} \times \underline{r} + \underline{\omega}_{SC} \times (\underline{\omega}_{SC} \times \underline{r}) = ... \\ ... = \ddot{\underline{r}}_{TM} - \ddot{\underline{r}}_{SC} - \dot{\underline{\omega}}_{SC} \times \underline{r}_{01} - \underline{\omega}_{SC} \times (\underline{\omega}_{SC} \times \underline{r}_{01}) \end{aligned} \tag{A.5}$$

The angular momentum equations for spacecraft and TM writes:

$$\underline{t}_{SC} = \underline{I}_{SC}\underline{\dot{\omega}}_{SC} + \underline{\omega}_{SC} \times \underline{I}_{SC}\underline{\omega}_{SC} \tag{A.6}$$

$$\underline{t}_{TM} = \underline{I}_{TM}\underline{\dot{\omega}}_{TM} + \underline{\omega}_{TM} \times \underline{I}_{TM}\underline{\omega}_{TM} \tag{A.7}$$

Equations A.3, A.5, A.6 and A.7 form the system describing the motion of the spacecraft due to non-gravitational disturbances and of the TM with respect to its housing.

$$\begin{cases} M\underline{\ddot{r}}_{SC} = \underline{f}_{SC} \\ \underline{\ddot{r}} + 2\underline{\omega}_{SC} \times \underline{\dot{r}} + \underline{\dot{\omega}}_{SC} \times \underline{r} + \underline{\omega}_{SC} \times (\underline{\omega}_{SC} \times \underline{r}) = ... \\ \qquad ... = \underline{\ddot{r}}_{TM} - \underline{\ddot{r}}_{SC} - \underline{\dot{\omega}}_{SC} \times \underline{r}_{01} - \underline{\omega}_{SC} \times (\underline{\omega}_{SC} \times \underline{r}_{01}) \\ \underline{t}_{SC} = \underline{I}_{SC}\underline{\dot{\omega}}_{SC} + \underline{\omega}_{SC} \times \underline{I}_{SC}\underline{\omega}_{SC} \\ \underline{t}_{TM} = \underline{I}_{TM}\underline{\dot{\omega}}_{TM} + \underline{\omega}_{TM} \times \underline{I}_{TM}\underline{\omega}_{TM} \end{cases} \tag{A.8}$$

The set of equations described by A.8 can be simplified by carrying out orders of magnitude analysis of the various terms of each one. By using the requirements specified in [8] for velocities and accelerations, the maximum modulus of each term can be approximately determined. The set of simplified equations appears as follows:

$$\begin{cases} \underline{\ddot{r}}_{SC} = \dfrac{\underline{f}_{SC}}{M} \\ \underline{\ddot{r}} = \dfrac{\underline{f}_{TM}}{m} - \dfrac{\underline{f}_{SC}}{M} - \underline{\dot{\omega}}_{SC} \times \underline{r}_{01} \\ \underline{\dot{\omega}}_{SC} = \underline{I}_{SC}^{-1}\underline{t}_{SC} \\ \underline{\dot{\omega}} = \underline{I}_{TM}^{-1}\underline{t}_{TM} - \underline{I}_{SC}^{-1}\underline{t}_{SC} \end{cases} \tag{A.9}$$

Where $\omega$ stands for the relative angular velocity between TM and spacecraft, and is defined as $\underline{\omega} = \underline{\omega}_{TM} - \underline{\omega}_{SC}$.
By using the notation:

$$\underline{\tilde{r}}_{01} = \begin{bmatrix} 0 & r_3 & -r_2 \\ -r_3 & 0 & r_1 \\ r_2 & -r_1 & 0 \end{bmatrix}$$

The vector product can be written in matrix form:

$$\underline{\dot{\omega}}_{SC} \times \underline{r}_{01} = \underline{\tilde{r}}_{01} \cdot \underline{\dot{\omega}}_{SC}$$

By using accelerations as variables, the system equations can be written in matrix form:

$$\underline{a}_{SC} = \frac{\underline{f}_{SC}}{M}; \quad \underline{a}_{TM} = \frac{\underline{f}_{TM}}{m}; \quad \underline{\alpha}_{SC} = \underline{I}_{SC}^{-1}\underline{t}_{SC}; \quad \underline{\alpha}_{TM} = \underline{I}_{TM}^{-1}\underline{t}_{TM}$$

$$\begin{Bmatrix} \ddot{\underline{r}}_{SC} \\ \dot{\underline{\omega}}_{SC} \\ \ddot{\underline{r}} \\ \dot{\underline{\omega}} \end{Bmatrix} = \begin{bmatrix} I & 0 & 0 & 0 \\ 0 & I & 0 & 0 \\ -I & -\tilde{\underline{r}}_{01} & I & 0 \\ 0 & -I & 0 & I \end{bmatrix} \begin{Bmatrix} \underline{a}_{SC} \\ \underline{\alpha}_{SC} \\ \underline{a}_{TM} \\ \underline{\alpha}_{TM} \end{Bmatrix}$$

The accelerations can be split between command and disturbance contribution for the spacecraft; command, disturbance and stiffness for the TM:

- $\begin{Bmatrix} \underline{a}_{SC} \\ \underline{\alpha}_{SC} \end{Bmatrix} = \underline{u}_T + \underline{d}_{SC}$ where $\underline{u}_T$ stands for thruster command and $\underline{d}_{SC}$ for external disturbances on the spacecraft;
- $\begin{Bmatrix} \underline{a}_{TM} \\ \underline{\alpha}_{TM} \end{Bmatrix} = \underline{u}_{ES} + \underline{d}_{TM} - \Omega^2 \begin{Bmatrix} \underline{r} \\ \underline{\varphi} \end{Bmatrix}$ where $\underline{u}_{ES}$ stands for electrostatic suspension command, $\underline{d}_{TM}$ for external disturbances on the test mass, and the last term accounts for forces dependent on test mass position.

Adopting this structure, the system is described by the following matrix representation:

$$\begin{Bmatrix} \ddot{\underline{r}}_{SC} \\ \dot{\underline{\omega}}_{SC} \\ \ddot{\underline{r}} \\ \dot{\underline{\omega}} \end{Bmatrix} = \begin{bmatrix} 0 & 0 \\ 0 & -\Omega^2 \end{bmatrix} \begin{Bmatrix} \underline{r}_{SC} \\ \underline{\varphi}_{SC} \\ \underline{r} \\ \underline{\varphi} \end{Bmatrix} + \begin{bmatrix} I & 0 & 0 & 0 \\ 0 & I & 0 & 0 \\ -I & -\tilde{\underline{r}}_{01} & I & 0 \\ 0 & -I & 0 & I \end{bmatrix} \left[ \begin{pmatrix} \underline{u}_T \\ \underline{u}_{ES} \end{pmatrix} + \begin{pmatrix} \underline{d}_{SC} \\ \underline{d}_{TM} \end{pmatrix} \right] \tag{A.10}$$

The first six equations are then entirely uncoupled.

The last six equations are coupled to the first six through thruster commands and spacecraft disturbances, and among themselves by effect of the stiffness matrix off-diagonal elements. These elements however, are modeled to be about 2 orders of magnitude smaller than diagonal ones, therefore allowing the matrix to be approximated as diagonal.
The equation for the test mass x degree of freedom writes:

$$\begin{aligned} \ddot{x}_1 = -\Omega_{11}^2 x_1 - u_{T\,x_{SC}} - d_{SC\,x_{SC}} + z_1(u_{T\,\theta_{SC}} + d_{SC\,\theta_{SC}}) \\ - y_1(u_{T\,\varphi_{SC}} + d_{SC\,\varphi_{SC}}) + u_{ES\,x_1} + d_{TM\,x_1} \end{aligned} \tag{A.11}$$

By assuming the spacecraft disturbances to be compensated using thruster action, to a level where they are negligible with respect to TM external disturbances, the equation becomes:

$$\ddot{x} = -\Omega_{11}^2 x + u_{ES\,x} + d_{TM\,x} \tag{A.12}$$

This last shape of the equation of motion simply expresses the dynamics of a forced spring.

## A.2 Adopted Model Limits

While carrying out the verification test runs for the various controllers, an ultimate limit on the displacements had to be defined, in order to find out how far the tests could be pushed while still providing meaningful results. A first definition of such a limit was the constraint that the test mass shall not touch the housing or the retracted plungers. Such a case allowed for wide displacements ranges (up to $\pm 2.4$ mm of pure $z$ displacement). However, anomalies in the model behavior suggested further investigation. It was found out that, for displacements smaller than the ones allowed by the contact limitation, the $6^{th}$ order model started providing unphysical results. For this reason, an evaluation of its validity limits has been carried out.
The displacement limit for validity has been defined as that value of the coordinate for which, the magnitude of a restoring force generated by fixed electrode voltages (e.g. positive displacement, negative force) stops decreasing and starts increasing. Such a behavior is nonphysical, and signals an anomaly in the model.
While this limit is of interest to us only for the $z$ axis, the evaluation has been carried out for $x$ and $y$ as well. Plots of the force versus the displacements are shown in figure A.2 and table A.1 summarizes the resulting limits.

| | Gap size | Model validity limits |
|---|---|---|
| $x$ | 4 mm | 2mm |
| $y$ | 2.9 mm | 1.4 mm |
| $z$ | 3.5 mm | 1.7mm |

Table A.1: $6^{th}$ order model displacement limits

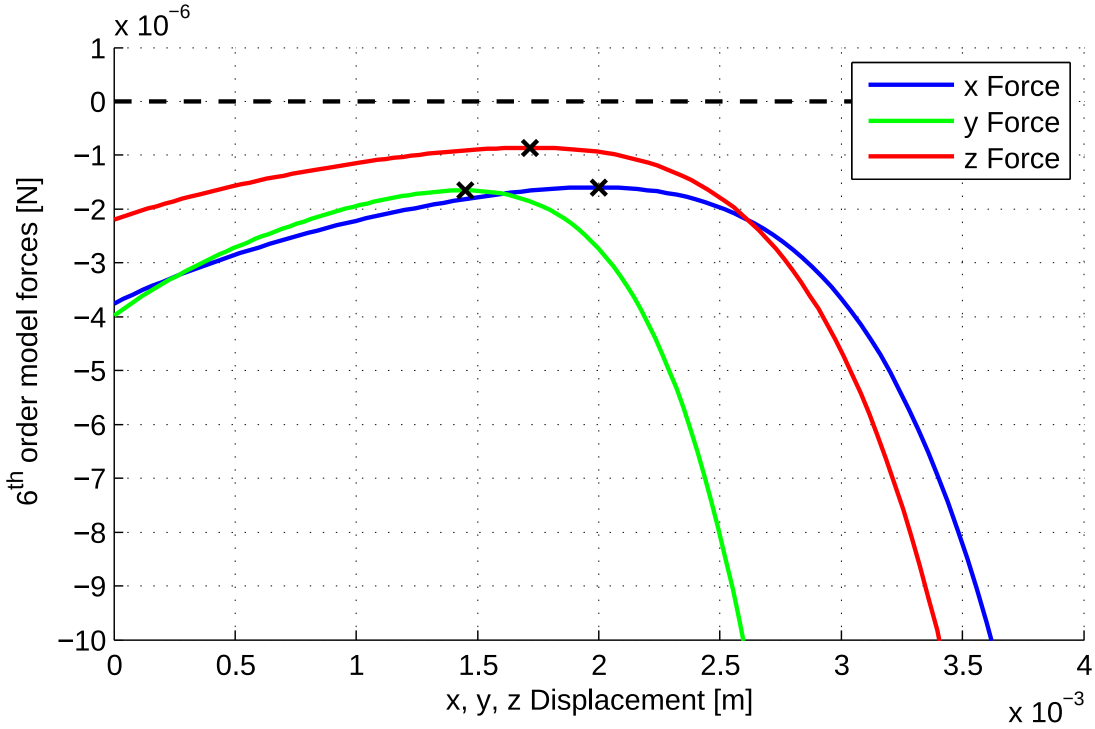


Figure A.2: $6^{th}$ order forces showing model validity limits

# Appendix B

# PID Controller Gains Derivation

In this appendix, a set of gains is derived for a PID controller, with the goal of exploiting a certain given fraction of the total available (known) command, for a certain condition, which is assumed to be the most demanding one.
For the specific case, the gains have been derived such that when in the worst-case initial conditions, the controller uses a set fraction of the total available actuation authority, thus avoiding saturation of the actuators. The equations of motion for one DOF (the x coordinate in the example) write:

$$\ddot{x} = -\Omega_{11}^2 x + u + d \tag{B.1}$$

$$u = K_P e + K_D \dot{e} + K_I \int_0^t e d\tau \tag{B.2}$$

$$e = r - x \tag{B.3}$$

$$x_{t=0} = x_0 \, ; \, \dot{x}_{t=0} = \dot{x}_0 \tag{B.4}$$

The Laplace transform of the controlled system free response (zero reference signal and nonzero initial conditions) is:

$$X(s) = \frac{s^2 x_0 + s\left(\dot{x}_0 + K_D x_0\right) + d}{s^3 + K_D s^2 + s\left(K_P + \Omega_{11}^2\right) + K_I} \tag{B.5}$$

Or, looking at the forced system (zero initial conditions, nonzero reference signal) the controlled system transfer function:

$$\frac{X\left(s\right)}{R\left(s\right)} = \frac{s^2 K_D + s K_P + K_I}{s^3 + K_D s^2 + s\left(K_P + \Omega_{11}^2\right) + K_I} \tag{B.6}$$

The system has three poles, and the denominator can be written as the product of a real pole and a complex conjugate pair:

$$\left(s + {}^{1}\!/_{\tau}\right)\left(s^2 + 2\xi\omega_n s + \omega_n^2\right) = s^3 + s^2\left({}^{1}\!/_{\tau} + 2\xi\omega_n\right) + s\left(\frac{2\xi\omega_n}{\tau} + \omega_n^2\right) + \frac{\omega_n^2}{\tau} \tag{B.7}$$

Where $\tau$ is the first order characteristic time, $\omega_n$ is the second order dynamics natural frequency and $\xi$ is its damping ratio.
By expanding and comparing this to the former writing of the denominator, the gains can be written as:

$$K_D = {}^{1}\!/_{\tau} + 2\xi\omega_n \tag{B.8}$$

$$K_P + \Omega_{11}^2 = \frac{2\xi\omega_n}{\tau} + \omega_n^2 \tag{B.9}$$

$$K_I = \frac{\omega_n^2}{\tau} \tag{B.10}$$

Two distinct characteristic dynamics have been identified: a first order and a second order one. Their characteristic times are related by a suitably defined parameter:

$$n = \frac{\tau}{{}^{4}\!/_{\xi\omega_n}} \leftrightarrow \tau = \frac{4n}{\xi\omega_n} \tag{B.11}$$

The parameter n represents the ratio between the first order characteristic time $\tau$ (exponential decay time) and the second order settling time which in the scope of this thesis is defined as $4/\xi\omega_n$[1]. Setting the value of n determines the speed at which the first order dynamic of the system is completed, with respect to the second order one. For a first approximation, requiring the two dynamics to have the same characteristic time was considered reasonable. The n was found to have limited influence over the overall system settling time, therefore requiring some trial and error to find a satisfactory value. Adopted values are in the range of 0.2 to 2.

The condition that the system must use a set fraction of the maximum available actuation when facing the worst case initial conditions writes:

$$u\,(0) = K_P x_0 + K_D \dot{x}_0 = u_c \tag{B.12}$$

Where $u_c$ is the chosen portion of total available actuation authority.
By substituting the expressions for the gains, and replacing $\tau$ with the expression in

[1]The formula for the settling time is not unique: Tay, Mareels and Moore (1997) defined settling time as "the time required for the response curve to reach and stay within a range of certain percentage (usually 5% or 2%) of the final value." [16]. Depending on the chosen threshold, a different constant for the numerator arises. For example, in [10] a 1% threshold is chosen, resulting in $\frac{4.6}{\omega_n}$, while for 2% one would obtain 3.9. Since the exact value of the coefficient is arbitrary, for the derivation the simple value of 4 has been adopted.

B.11, the following equation is obtained:

$$\omega_n^2 \left(1 + \frac{\xi^2}{2n}\right) x_0 + \xi\omega_n \left(2 + \frac{1}{4n}\right) \dot{x}_0 - \Omega_{11}^2 x_0 - u_c = 0 \tag{B.13}$$

By requiring the second order dynamic to have a set damping ratio (1 was chosen for minimum overshoot) equation B.13 is a second order polynomial in the natural frequency, therefore it can be solved the resulting $\omega_n$ value can be substituted back in the gains expressions to obtain the controller.

$$\omega_n = \frac{-\frac{\xi\dot{x}_0}{2}\left(2 + \frac{1}{4n}\right) \pm \sqrt{\frac{\xi^2\dot{x}_0^2}{4}\left(2 + \frac{1}{4n}\right)^2 + \left(x_0\Omega_{11}^2 + u_c\right)\left(1 + \frac{\xi^2}{2n}\right) x_0}}{\left(1 + \frac{\xi^2}{2n}\right) x_0} \tag{B.14}$$

The correct solution to obtain a positive value of the natural frequency is the one with the plus sign. The values of n chosen in the final PID controller shown in chapter 3, including the filter, are:

- $n = 0.3$ for the $z$ DoF controller
- $n = 0.2$ for the $\eta$ DoF controller

# Appendix C

# State Estimators Design

The derivation for the two state estimators that were considered during the development of the new control strategy is reported here, together with the main results of their comparison.

## C.1 Reduced State Observer

Following standard textbook approach [10], a brief derivation of a reduced state observer for the studied system is presented.

The state vector is divided in a state $x_1$ which is measured, and states $x_2$ and $x_3$ which are not measured. The $\underline{r}$ vector is defined as:

$$\underline{r} = [x_2, x_3]^T \tag{C.1}$$

and the system equations can be written as:

$$\underline{\dot{x}} = \begin{bmatrix} \dot{x}_1 \\ \underline{\dot{r}} \end{bmatrix} = \begin{bmatrix} A_{11} & \underline{A}_{12} \\ \underline{A}_{21} & \underline{A}_{22} \end{bmatrix} \begin{bmatrix} x_1 \\ \underline{r} \end{bmatrix} + \begin{bmatrix} B_1 \\ \underline{B}_2 \end{bmatrix} u \tag{C.2}$$

With

$$A_{11} = [0] \ ; \ \underline{A}_{12} = \begin{bmatrix} 1 & 0 \end{bmatrix} \ ; \ \underline{A}_{21} = \begin{bmatrix} -\omega^2 \\ 0 \end{bmatrix} \ ; \ \underline{A}_{22} = \begin{bmatrix} 0 & 1 \\ 0 & 0 \end{bmatrix} \tag{C.3}$$

$$B_1 = [0] \ ; \ \underline{B}_2 = \begin{bmatrix} 1 \\ 0 \end{bmatrix} \tag{C.4}$$

The goal of the reduced state observer is to provide an estimate of the non-measured states, which is called $\underline{\tilde{r}}$. The dynamics of the reduced state observer is then described by the following equations:

$$\underline{\dot{\rho}} = \left(\underline{A}_{22} - \underline{L}\cdot\underline{A}_{12}\right)\underline{\rho} + \left(\underline{B}_2 - \underline{L}\cdot\underline{B}_1\right)\cdot u + \left(\left(\underline{A}_{22} - \underline{L}\cdot\underline{A}_{12}\right)\cdot\underline{L} + \underline{A}_{21} - \underline{L}\cdot A_{11}\right)y \quad \text{(C.5)}$$

$$\underline{\tilde{r}} = \underline{\rho} + \underline{L}\cdot y \quad \text{(C.6)}$$

Where $\underline{\rho}$ stands for the observer state vector. It is important to remark that the observer state vector $\underline{\rho}$ does not correspond to the reduced system state vector $\underline{\tilde{r}}$.

The observer estimate error vector is defined as:

$$\underline{\dot{\varepsilon}} = \left(\underline{A}_{22} - \underline{L}\cdot\underline{A}_{12}\right)\cdot\underline{\varepsilon} \quad \text{(C.7)}$$

The dynamic matrix of the reduced observer, as well as of its error, corresponds to $(\underline{A}_{22} - \underline{L}\cdot\underline{A}_{12})$. The eigenvalues of such matrix determine the system poles, and therefore its dynamics. By requiring given observer dynamics characteristics, we can determine the observer gains.

The poles of the system are the roots of the characteristic equation:

$$\det\left(sI - \left(\underline{A}_{22} - \underline{L}\cdot\underline{A}_{12}\right)\right) = 0 \quad \text{(C.8)}$$

By assuming $\underline{L} = \begin{bmatrix} l_1 & l_2 \end{bmatrix}^T$, equation C.8 can be written in scalar form:

$$s^2 + l_1 s + l_2 = 0 \quad \text{(C.9)}$$

And, by comparing that shape with the more familiar one:

$$s^2 + 2\xi\omega_n s + \omega_n^2 = 0 \quad \text{(C.10)}$$

The elements of the gain vector can be determined by imposing certain features of the system dynamics. In particular,focusing on the dynamics damping ratio and settling time:

- $\xi = 1$ for well damped dynamics;
- $T_s = \dfrac{4}{\xi\omega_n}$ to be chosen as system design parameter.

The gains are then calculated as:

$$l_1 = \frac{8}{T_s}\,;\; l_2 = \frac{16}{(T_s\xi)^2} \quad \text{(C.11)}$$

Imposing a short observer settling time (making the system faster) results in a noisier state estimate. On the other hand, making the system slower allows for more noise rejection, at the cost of a longer estimation convergence time. For our purposes, a settling time of 10 seconds has been chosen. This results in a rather fast observer (the slowest state estimate to reach steady state takes about 30 seconds) that however does not show great noise rejection properties, especially on the third state estimate. The torque disturbance estimate is, as a matter of fact, almost entirely noise. Due to the great difference in orders of magnitude between the torque disturbance and the actuated torque, this will not result in a significant issue for the controller.

## C.2 Kalman Filter Design

Fundamentals of Kalman filtering can be found in several optimal estimation textbooks. Therefore, only a description of what a Kalman filter is, and how to derive one that suits our application is presented. The following derivation is largely based on [1].

The discrete-time representation of the studied linear system writes:

$$\begin{aligned} x_k &= F_{k-1}x_{k-1} + G_{k-1}u_{k-1} + w_{k-1} \\ y_k &= H_k x_k + v_k \end{aligned} \tag{C.12}$$

In the simple Kalman filter case, the noise processes $\{w_k\}$ and $\{v_k\}$ are white, zero-mean, uncorrelated and of known covariance matrices $Q_k$ and $R_k$ respectively.

$$\begin{aligned} E\left[w_k w_j^T\right] &= Q_k \delta_{k-j} \\ E\left[v_k v_j^T\right] &= R_k \delta_{k-j} \\ E\left[v_k w_j^T\right] &= 0 \end{aligned} \tag{C.13}$$

For the studied case, however, this is not entirely true. The electrostatic actuation and sensing noise, in fact, are given as colored noise, with known (from requirements) power spectral densities. The first filter will still be designed assuming white noise, verifying a posteriori whether its performance is satisfactory, or it is necessary to adopt a more complex filter (e.g. by using state augmentation).

The use of purely white noise can be justified by observing that the noise spectrum is indeed flat over a wide range of frequencies, and rises considerably (colored behavior) for frequencies in the millihertz range, its effect becoming substantial for timescales of thousands of seconds, much greater than the approximate settling times for test mass release and catch phase.

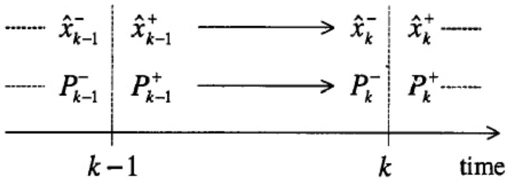


FIGURE C.1: Timeline for a priori and a posteriori estimates and error covariances [1]

The Kalman filter algorithm is essentially a repeating update of system state estimation, and error covariance matrix estimation, by exploiting known features of the system (its discrete-time matrix representation, and noise processes covariance matrices) and noisy measurements of the system output. Two types of estimation are defined, for both system state, and error covariance matrix:

- The *a posteriori* estimation
- The *a priori* estimation

The *a posteriori* estimate is calculated when all measurements including time k are available.
The *a priori* estimate is calculated when all measurements up to, but not including, time k are available.
Figure C.1 shows the concept of a priori (minus superscript) and a posteriori (plus superscript) estimates for timesteps k-1 and k. The filter is initialized at time 0 with some estimate of the initial system state $\hat{x}_0^+$.
From this initialization step, the a-priori state estimate for timestep $k = 1$ is computed using the following formula:

$$\hat{x}_1^- = F_0\hat{x}_0^+ + G_0u_0 \tag{C.14}$$

The general relation between the a priori estimate for timestep $k$ and a posteriori for timestep $k-1$, called time update equation, is:

$$\hat{x}_k^- = F_k\hat{x}_{k-1}^+ + G_{k-1}u_{k-1} \tag{C.15}$$

Which essentially states that, having the a posteriori state estimate for timestep $k-1$, the state estimate can be updated based on our knowledge of the system dynamics. No additional information coming from the measurements is introduced in this step.

The same must be done for the state estimation error covariance matrix, and its time update equation is:

$$P_1^- = F_0P_0^+F_0^T + Q_0 \tag{C.16}$$

The general form of which, is:

$$P_k^- = F_{k-1}P_{k-1}^+F_{k-1}^T + Q_{k-1} \tag{C.17}$$

Again, no information coming from measurements is introduced in this step.

The estimates at time k are then updated, based on the measurements at time k (measurement update equation), transitioning from the a priori estimates to the a posteriori ones. The equations used in doing so so are:

$$K_k = P_k^- H_k^T \left(H_k P_k^- H_k^T + R_k\right)^{-1} \tag{C.18}$$

$$\hat{x}_k^+ = \hat{x}_k^- + K_k \left(y_k - H_k \hat{x}_k^-\right) \tag{C.19}$$

$$P_k^+ = \left(I - K_k H_k\right) P_k^- \tag{C.20}$$

### C.2.1 Final Filter Equations

Finally, all the above equations are combined in the algorithm which essentially is the Kalman filter for the studied system. Since the studied linear system is a time invariant one, all the system matrices have no time-index k. The algorithm then appears as follows.
The dynamic system of interest is given by the equations:

$$x_k = Fx_{k-1} + Gu_{k-1} + w_{k-1} \tag{C.21}$$

$$y_k = Hx_k + v_k \tag{C.22}$$

$$E\left[w_k w_j^T\right] = Q_k \delta_{k-j} \tag{C.23}$$

$$E\left[v_k v_j^T\right] = R_k \delta_{k-j} \tag{C.24}$$

$$E\left[v_k w_j^T\right] = 0 \tag{C.25}$$

The Kalman filter is initialized as follows:

$$\underline{\hat{x}}_0^+ = E\left(x_0\right) \tag{C.26}$$

$$P_0^+ = E\left[\left(x_0 - \hat{x}_0^+\right)\left(x_0 - \hat{x}_0^+\right)^T\right] \tag{C.27}$$

The filter itself is made up of the following equations, which are computed in the reported order for each timestep $k$:

1. $P_k^- = FP_{k-1}^+F^T + Q$
2. $\hat{x}_k^- = F\hat{x}_{k-1}^+ + Gu_{k-1}$

3. $K_k = P_k^- H^T \left(H P_k^- H^T + R\right)^{-1}$

4. $\hat{x}_k^+ = \hat{x}_k^- + K_k \left(y_k - H\hat{x}_k^-\right)$

5. $P_k^+ = \left(I - K_k H\right) P_k^-$

The filter initialization values are taken as:

- $\hat{x}_0^+ = \begin{bmatrix} 0 \\ 0 \\ 0 \end{bmatrix}$ (since no knowledge of the initial state is available);
- $P_0^+ = \begin{bmatrix} 1 & 0 & 0 \\ 0 & 1 & 0 \\ 0 & 0 & 1 \end{bmatrix}$

The state estimation error covariance matrix initial condition $P_0^+$ is worth some explanation. It is essentially a representation of how much our estimate of the initial state is correct. If we thought our estimate to be close to reality, we could set it to a very small value. On the other hand, if we have absolutely no knowledge of the initial state, and hence our estimate is a complete guess, strictly speaking the elements of the $P_0^+$ diagonal should be infinite. However, it can be shown ([11], chap. 4 "Initial covariance matrix") that the initial condition on the error covariance matrix has almost no influence on the filter performances (as long as its elements are different from zero). In our case, setting the diagonal elements to proper values (for example, the maximum possible value of $E\left[\left(x_0 - \hat{x}_0^+\right)\left(x_0 - \hat{x}_0^+\right)^T\right]$) or setting them to 1, produces no appreciable difference in the filter performances.

### C.2.2 Implementation Remarks

The actual implementation of the Kalman filter must be carried out carefully, since one might lose all advantages connected to its use.
Due to the time-variant nature of the filter, when initialized, it will perform a swift adaptation to the system state (very low noise rejection) in the first time steps, and then quickly transition to a slower, higher noise-rejecting filter. This transition, and the resulting "speed" of the steady state filter, is entirely determined by the system and noise model that we use for designing it; it has no connection whatsoever with the incoming inputs and produced outputs. The most immediate consequence to such a behavior is that, if initialized and fed (for some reasons) with wrong inputs, it will quickly settle to a wrong estimate of the system state, and then be very slow to converge

to the actual one when correct inputs are available. Such a problem showed up in the simulator implementation of the filter, due to the fact that the sensor model output was produced with a delay smaller than a second, causing the first few inputs to the filter to be detrimental for state estimate. It was dealt with by delaying by 1 second the filter activation so that the correct readings were available at sensor output.
Another point in the filter implementation is the correct matching of measured position and incoming command. For the filter to perform as expected, a correctly matching pair of $y_k$ and $u_{k-1}$ must be fed to the algorithm at every time step. In the simplified simulator, a delay of 0.2 seconds in real to measured position was detected, and one of 0.1 seconds from commanded to actuated force.

### C.2.3 Weight Matrices Derivation

To build the Kalman filter for the studied system the following building blocks are needed:

- The system fundamental matrix: $F$
- The system input matrix: $G$
- The system output matrix: $H$
- The process and measurement noise covariance matrices: $Q$ and $R$

The first three matrices are obtained through standard continuous system discretization [10], adopting a first order approximation for the exponential matrix:

$$F = e^{AT} \cong I + AT \tag{C.28}$$

$$Gu_k = \int_{t_k}^{t_k+T} e^{At} Bu\left(t\right) dt = \int_0^T e^{At} Bu\left(t_k\right) dt \cong T\left(I + \frac{AT}{2}\right) Bu\left(t_k\right) \tag{C.29}$$

$$H = C \tag{C.30}$$

In principle, the $R$ and $Q$ matrices should represent the measurement and process noise covariance matrices. However, more generally, they should represent the expected value of the square of the difference between the real and the assumed system. If one would have a “strictly noisy” measurement, and a “strictly noisy” command, then $Q$ and $R$ would correspond exactly to the measurement and process noise covariance matrices. However, in the present application, noisy and approximated measurement and command are used. For this reason, $Q$ and $R$ take into consideration both the uncertainty introduced by the noise, and by the measurement or actuation error.

### C.2.4 Derivation of the Q Matrix

Starting from the continuous representation of the system, the continuous-time process noise covariance matrix is obtained:

$$\underline{w} = \begin{bmatrix} 0 \\ w \\ 0 \end{bmatrix} \tag{C.31}$$

$$Q_{cont} = E\left[\underline{w} \cdot \underline{w}^T\right] = \begin{bmatrix} 0 & 0 & 0 \\ 0 & \sigma_w^2 & 0 \\ 0 & 0 & 0 \end{bmatrix} \tag{C.32}$$

The discrete-time process noise covariance matrix $Q$ can then be determined from the continuous one and the system fundamental matrix:

$$Q_k = \int_0^{T_s} F(\tau)\, Q_{cont} F^T(\tau)\, d\tau \tag{C.33}$$

For the studied case, the resulting $Q$ matrix is:

$$Q = \sigma_w^2 \int_0^{T_s} \begin{bmatrix} \tau^2 & \tau + \frac{-\omega^2\tau^3}{2} & 0 \\ \tau + \frac{-\omega^2\tau^3}{2} & 1 + \frac{-\omega^2\tau^3}{2} & 0 \\ 0 & 0 & 0 \end{bmatrix} d\tau \tag{C.34}$$

Some orders of magnitude simplifications are possible:

$$\tau \cong 10^{-2} \tag{C.35}$$

$$\omega^2 \cong 10^{-7} \tag{C.36}$$

$$\tau \gg \omega^2\tau^3 \tag{C.37}$$

Finally obtaining:

$$Q = \sigma_w^2 \begin{bmatrix} \frac{T_s^3}{3} & \frac{T_s^2}{2} & 0 \\ \frac{T_s^2}{2} & T_s & 0 \\ 0 & 0 & 0 \end{bmatrix} \tag{C.38}$$

The $\sigma_w^2$ value should represent the variance of the noise. However, for the system at hand, which contains command errors as well as noise, it is more useful to imagine it as representing the magnitude of the system uncertainties, and is computed as the expected value of the squared error between real and assumed model. It can be then thought of as composed of two different contributions:

- The noise uncertainty

- The command error uncertainty

The latter is then treated as a zero mean uncorrelated quantity, i.e. additional noise. The magnitude of these two contributions is assessed below.

#### C.2.4.1 Assessment of Noise Uncertainty

By assuming zero-mean process noise, the approximated variances for each degree of freedom are computed, by integrating the respective power spectrums between 0 and a threshold frequency where the computation is truncated.

$$\sigma^2_{wnoise} = \int_0^{f_{th}} H_{act}(s)^2 ds \tag{C.39}$$

Where H(s) is defined in [17], DF-CON-014 as the noise shape filter characteristic transfer function. This threshold has been chosen as 0.1Hz, driven from the examination of the Bode plot of the noise shape filter used to model the noise (see figure C.2). Further increase of the threshold resulted in negligible increase of the resulting variances.

The results are:

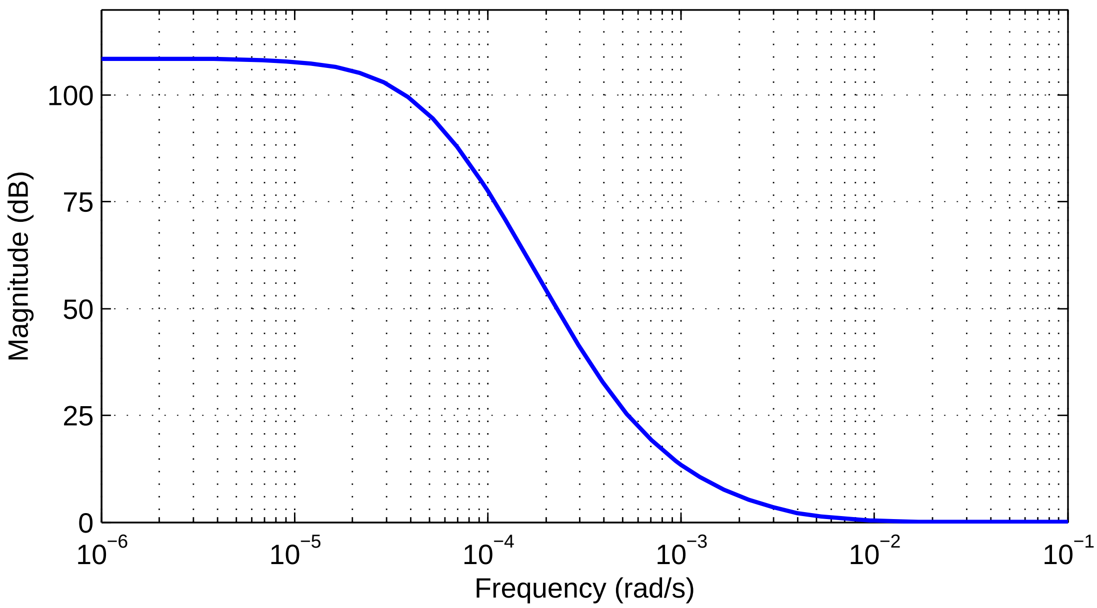


Figure C.2: Magnitude Bode plot for the actuation noise shape filter

| | $\sigma^2_{wnoise}$ |
|---|---|
| $x$ | $1.641 \cdot 10^{-20} \frac{m^2}{s^4}$ |
| $y$ | $6.247 \cdot 10^{-20} \frac{m^2}{s^4}$ |
| $z$ | $2.605 \cdot 10^{-19} \frac{m^2}{s^4}$ |
| $\theta$ | $1.216 \cdot 10^{-17} \frac{rad^2}{s^4}$ |
| $\eta$ | $4.863 \cdot 10^{-17} \frac{rad^2}{s^4}$ |
| $\phi$ | $1.66 \cdot 10^{-18} \frac{rad^2}{s^4}$ |

Table C.1: Process noise variances

#### C.2.4.2 Assessment of Command Error Uncertainty

Since the implemented actuation algorithm is based on a first-order capacitance model, we assume a 10% error in the commanded to actuated force and torque will be present.

$$u_{real} = (1 \pm 0.1)\, u_{cmd} \tag{C.40}$$

For this reason, the absolute value of the actuation error will always (while the linearization holds) be smaller than 10% of the maximum actuation authority:

$$u_{err} = u_{real} - u_{cmd} = \pm 0.1 u_{cmd} \leq \pm 0.1 u_{\max} \tag{C.41}$$

To evaluate the influence of such an error on our model, we conservatively assume that the error between our model (commanded force/torque) and the real one (actuated force/torque) will always be the maximum value: 10% of the maximum actuation authority for the particular degree of freedom:

$$|u_{err}| = 0.1 u_{\max} \tag{C.42}$$

Since the error is in this case assumed to be a constant, the expected value of its square will be just its squared value.

$$E\left[u_{err}^2\right] = 0.01 u_{\max}^2 \tag{C.43}$$

The results of this evaluation, for each degree of freedom, are:

| | 10% max actuation | $\sigma^2_{wcmderr}$ |
|---|---|---|
| $x$ | $9.6 \cdot 10^{-8} \frac{m}{s^2}$ | $9.22 \cdot 10^{-15} \frac{m^2}{s^4}$ |
| $y$ | $1 \cdot 10^{-7} \frac{m}{s^2}$ | $1 \cdot 10^{-14} \frac{m^2}{s^4}$ |
| $z$ | $5.6 \cdot 10^{-8} \frac{m}{s^2}$ | $3.14 \cdot 10^{-15} \frac{m^2}{s^4}$ |
| $\theta$ | $4.99 \cdot 10^{-6} \frac{rad}{s^2}$ | $2.5 \cdot 10^{-12} \frac{rad^2}{s^4}$ |
| $\eta$ | $2.43 \cdot 10^{-6} \frac{rad}{s^2}$ | $6 \cdot 10^{-12} \frac{rad^2}{s^4}$ |
| $\phi$ | $3.03 \cdot 10^{-6} \frac{rad}{s^2}$ | $9.2 \cdot 10^{-12} \frac{rad^2}{s^4}$ |

Table C.2: Command error variances

#### C.2.4.3 Final Q Matrices

As can be easily verified just by looking at the above tables, the uncertainty of our model due to the command error dominates the one due to the noise by 5 to 6 orders of magnitude. For this reason, for filter tuning, a $Q$ matrix where $\sigma^2_w = \sigma^2_{wcmderr}$ was adopted.

| | $\sigma^2_w$ |
|---|---|
| $x$ | $9.22 \cdot 10^{-15} \frac{m^2}{s^4}$ |
| $y$ | $1 \cdot 10^{-14} \frac{m^2}{s^4}$ |
| $z$ | $3.14 \cdot 10^{-15} \frac{m^2}{s^4}$ |
| $\theta$ | $2.5 \cdot 10^{-12} \frac{rad^2}{s^4}$ |
| $\eta$ | $6 \cdot 10^{-12} \frac{rad^2}{s^4}$ |
| $\phi$ | $9.2 \cdot 10^{-12} \frac{rad^2}{s^4}$ |

Table C.3: Final Q matrix variances values

### C.2.5 Derivation of the R matrix

Since the measurement for our system is a scalar quantity, the R matrix will be a simple scalar as well. In general, $R = \sigma^2_v$, where $\sigma^2_v$ represents the expected value of the difference between the real and the assumed model. However, just like the $Q$ matrix case, the system model is characterized by a noisy, approximated, measurement. For this reason, it is needed to again evaluate the contributions of two sources of uncertainties: noise and measurement error.

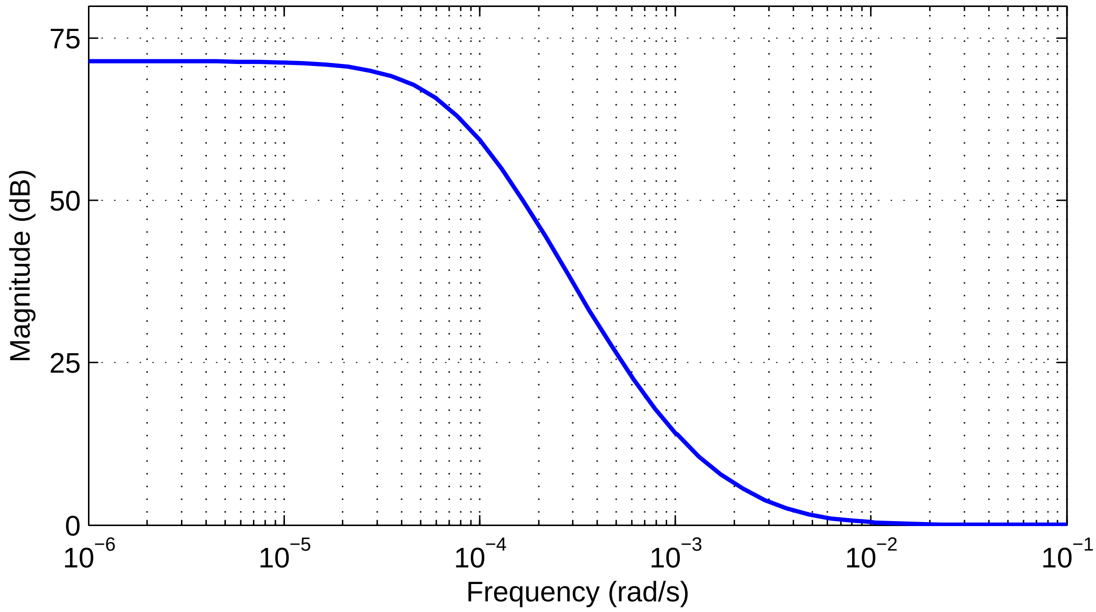


FIGURE C.3: Magnitude Bode plot for the sensing noise shape filter

#### C.2.5.1 Assessment of Noise Uncertainty

By assuming zero-mean process noise, the approximated variances for each degree of freedom are computed, by integrating the respective power spectrums between 0 and a threshold frequency where the computation is truncated.

$$\sigma^2_{wnoise} = \int_0^{f_{th}} H_{sens}(s)^2 ds \tag{C.44}$$

Where H(s) is defined in [17] DF-CON-019 as the noise shape filter characteristic transfer function.

This threshold has been chosen as 0.1Hz, driven from the examination of the Bode plot of the noise shape filter used to model the noise(see figure C.3). Further increase of the threshold resulted in negligible increase of the resulting variances. The results are:

| | $\sigma^2_{vnoise}$ |
|---|---|
| $x$ | $1.679 \cdot 10^{-13} m^2$ |
| $y$ | $1.380 \cdot 10^{-13} m^2$ |
| $z$ | $3.690 \cdot 10^{-13} m^2$ |
| $\theta$ | $5.720 \cdot 10^{-9} rad^2$ |
| $\eta$ | $1.589 \cdot 10^{-8} rad^2$ |
| $\phi$ | $1.345 \cdot 10^{-8} rad^2$ |

TABLE C.4: Measurement noise variances

#### C.2.5.2 Assessment of Measurement Error Uncertainty

Assuming a 10% error on position measurement, a reasonably conservative estimate of the worst case measurement error is needed.

$$x_{meas} = (1 \pm 0.1)\, x_{real} \tag{C.45}$$

While for the command error case, assuming 10% of the maximum actuation was an appropriate estimate of the real error (it is desirable to exploit the maximum possible actuation), assuming 10% of the maximum overshoot is not reasonable, since the main goal of the controller design is to avoid high overshoots. A reasonable worst-case displacement is assumed to be 1.5 times the worst-case initial displacement condition for every degree of freedom. The worst-case measurement error is then computed based on that assumption.

$$x_{\max} \cong 1.5 x_{0\max} \tag{C.46}$$

$$x_{err} = x_{real} - x_{meas} = \pm 0.1 x_{real} \leq \pm 0.1 x_{\max} \tag{C.47}$$

$$|x_{err}| = 0.1 x_{\max} = 0.15 x_{0\max} \tag{C.48}$$

$$E\left[x_{err}^2\right] = 0.0255 x_{0\max}^2 \tag{C.49}$$

The results are:

| | 15% initial displacement | $\sigma^2_{vmeaserr}$ |
|---|---|---|
| $x$ | $3 \cdot 10^{-5} m$ | $9 \cdot 10^{-10} m^2$ |
| $y$ | $3 \cdot 10^{-5} m$ | $9 \cdot 10^{-10} m^2$ |
| $z$ | $3 \cdot 10^{-5} m$ | $9 \cdot 10^{-10} m^2$ |
| $\theta$ | $3 \cdot 10^{-5} rad$ | $9 \cdot 10^{-8} rad^2$ |
| $\eta$ | $3 \cdot 10^{-5} rad$ | $9 \cdot 10^{-8} rad^2$ |
| $\phi$ | $3 \cdot 10^{-5} rad$ | $9 \cdot 10^{-8} rad^2$ |

TABLE C.5: Measurement error variances

#### C.2.5.3 Final R Matrices

As can be verified by looking at the above tables, the uncertainty due to the measurement error dominates the one due to the noise by 3 orders of magnitude for the translation degrees of freedom, while it is much closer for the rotational ones. It is therefore necessary to further proceed by developing a summation of contributions for the rotational degrees of freedom, based on a worst case error scenario. The sum of the maximum measurement error and the average noise one is considered, and is taken as the worst case maximum error between our model and reality. The computation of the $\sigma_v^2$ parameter is then carried out using the following formula:

$$\sigma_v^2 = \left(\sqrt{\sigma_{vmeaserr}^2} + \sqrt{\sigma_{vnoise}^2}\right)^2 \tag{C.50}$$

The results for the final R matrices are:

| | $\sigma_v^2$ |
|---|---|
| $x$ | $9 \cdot 10^{-10} m^2$ |
| $y$ | $9 \cdot 10^{-10} m^2$ |
| $z$ | $9 \cdot 10^{-10} m^2$ |
| $\theta$ | $1.4 \cdot 10^{-7} rad^2$ |
| $\eta$ | $1.8 \cdot 10^{-7} rad^2$ |
| $\phi$ | $1.7 \cdot 10^{-7} rad^2$ |

Table C.6: Final R matrix variances

## C.3 Estimator Selection

Both designed state estimators were tested with no feedback command, to test their performances and assess which one should be chosen for controller design. The simulations were run without introducing the control signal, in order to assess the pure estimation capabilities of both designs. Figures C.4 through C.13 show the results of the comparison. All the estimates show a deviation from the correct values for times greater than 40 to 60 seconds depending on the case. This is caused by the position-dependent sensor error, which keeps increasing over time due to the absence of a control signal. Only the Kalman filter estimate is shown for the displacement, since the reduced observer does not compute it.

### C.3.1 Test mass position and attitude estimates

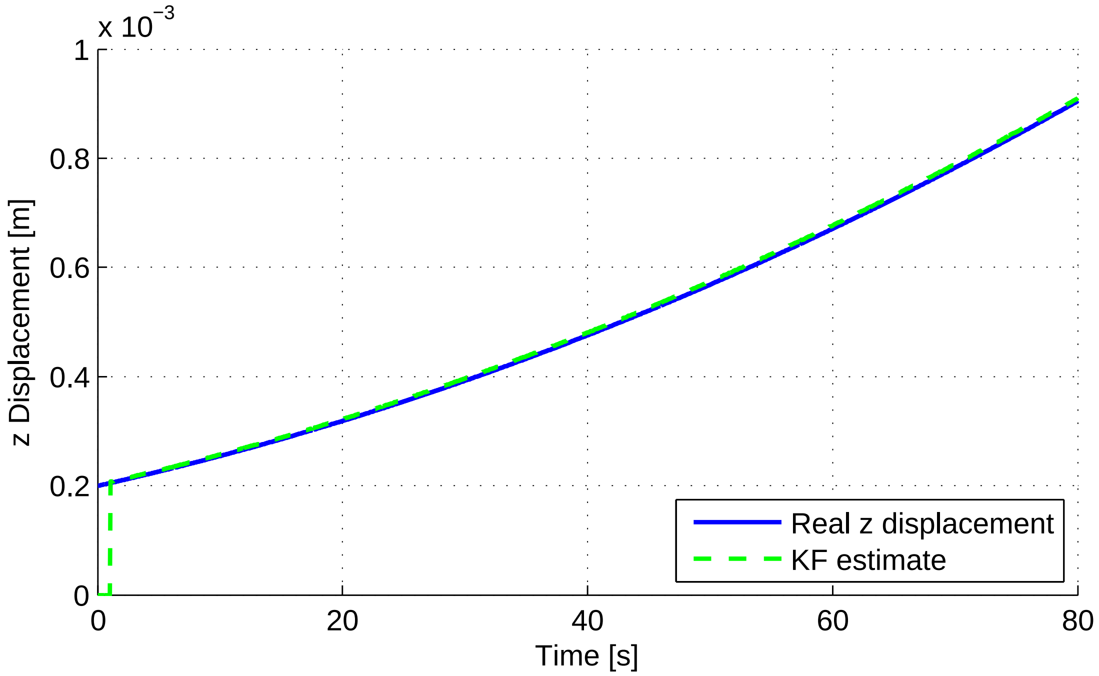


FIGURE C.4: z displacement, KF estimate

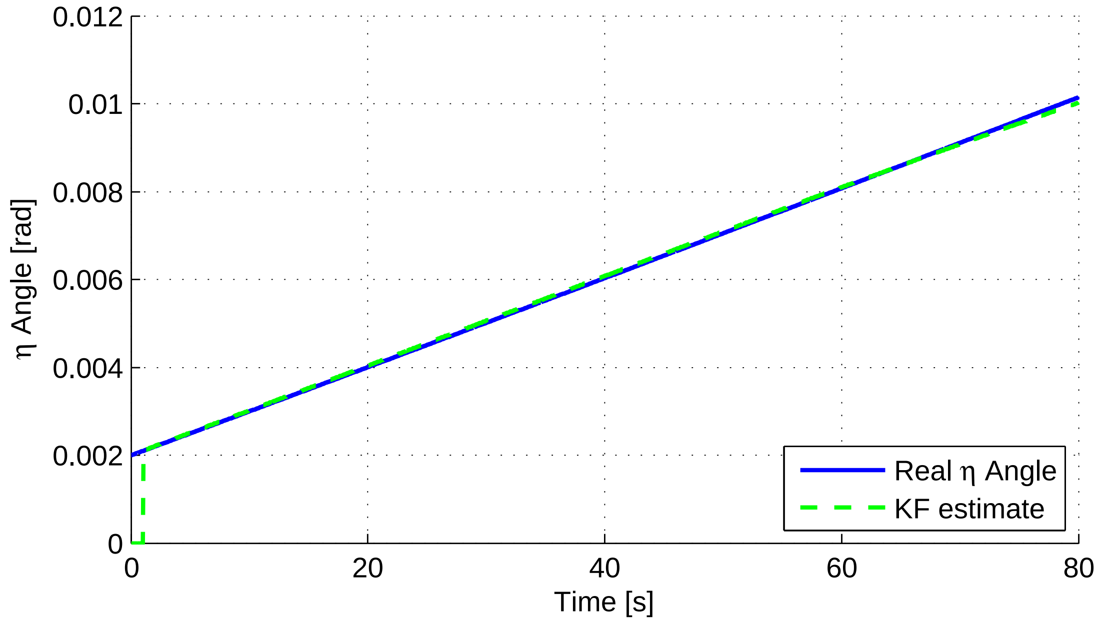


FIGURE C.5: $\eta$ angle, KF estimate

### C.3.2 Test mass velocity and rate estimates

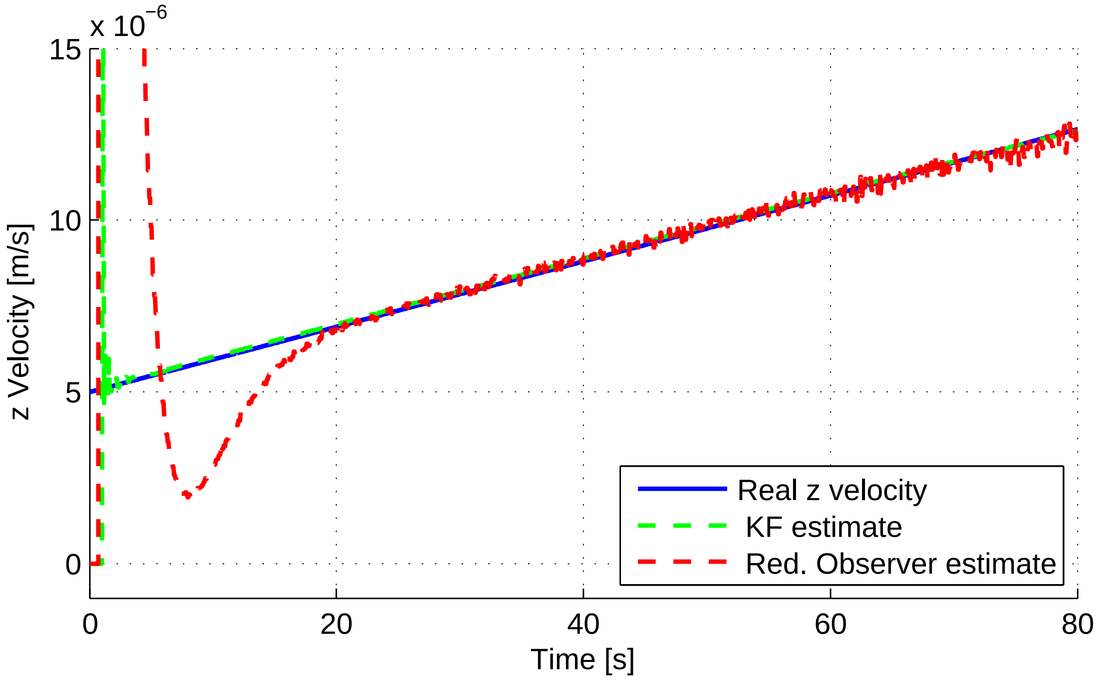


FIGURE C.6: KF and Observer velocity estimates

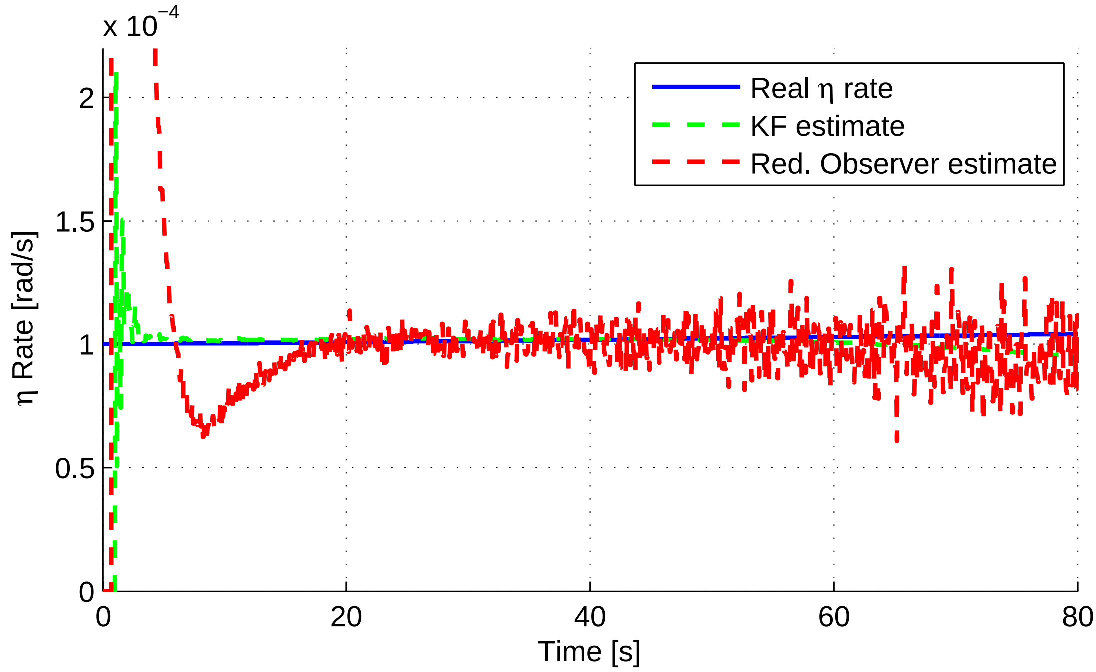


FIGURE C.7: KF and Observer rate estimates

### C.3.3 Test mass velocity and rate estimate errors

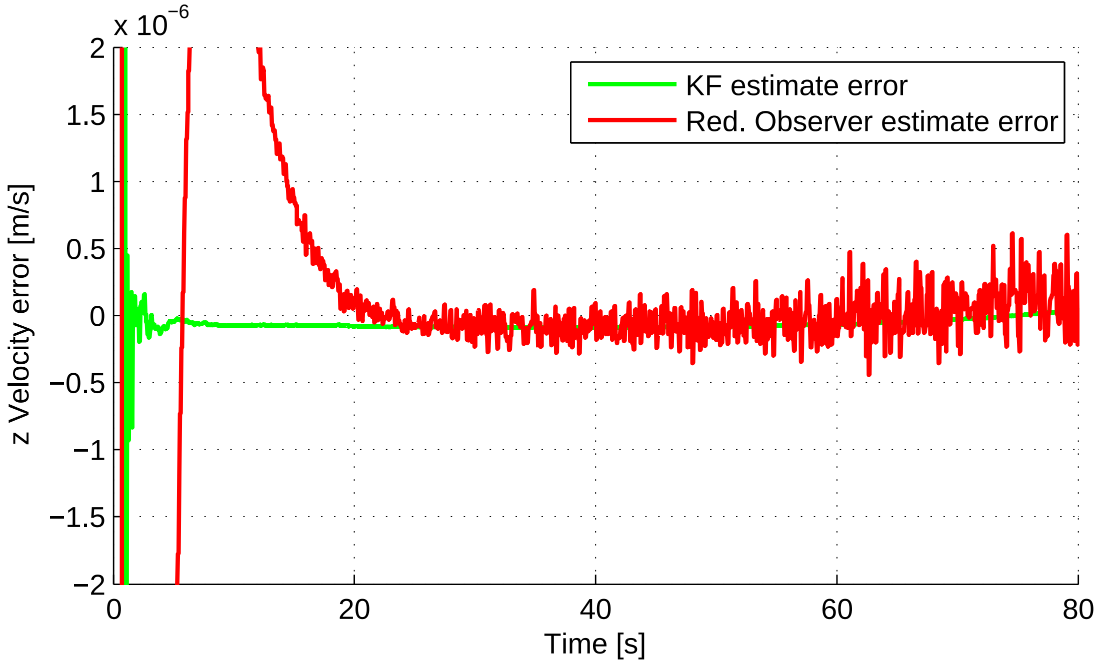


FIGURE C.8: KF and Observer velocity estimates error

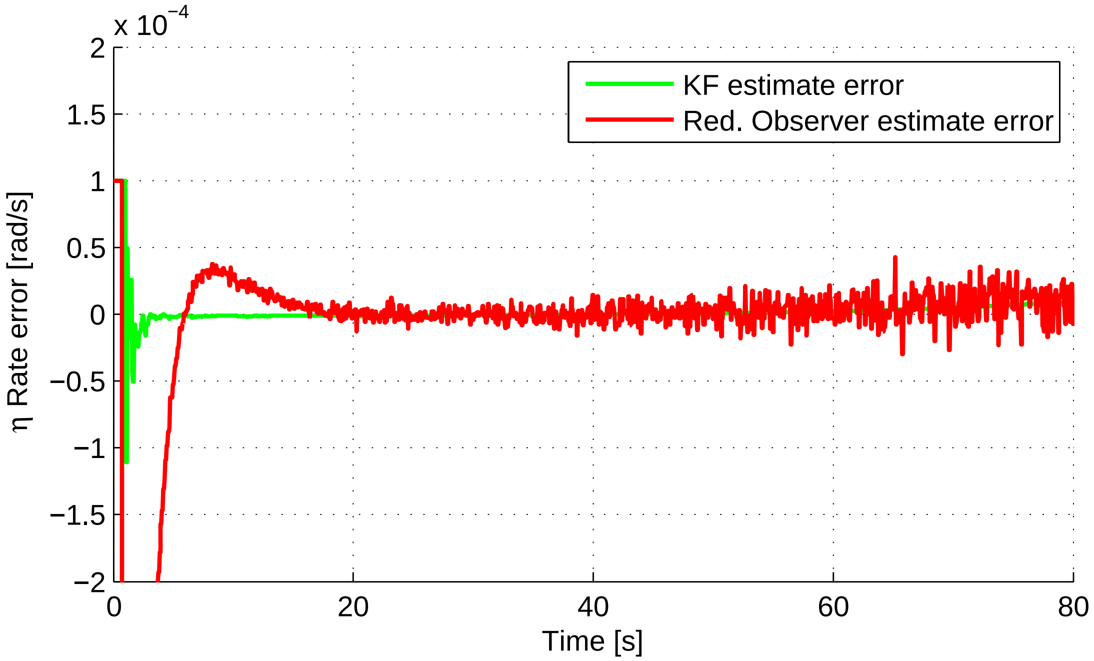


FIGURE C.9: KF and Observer rate estimates error

### C.3.4 Disturbance forces and torques estimates

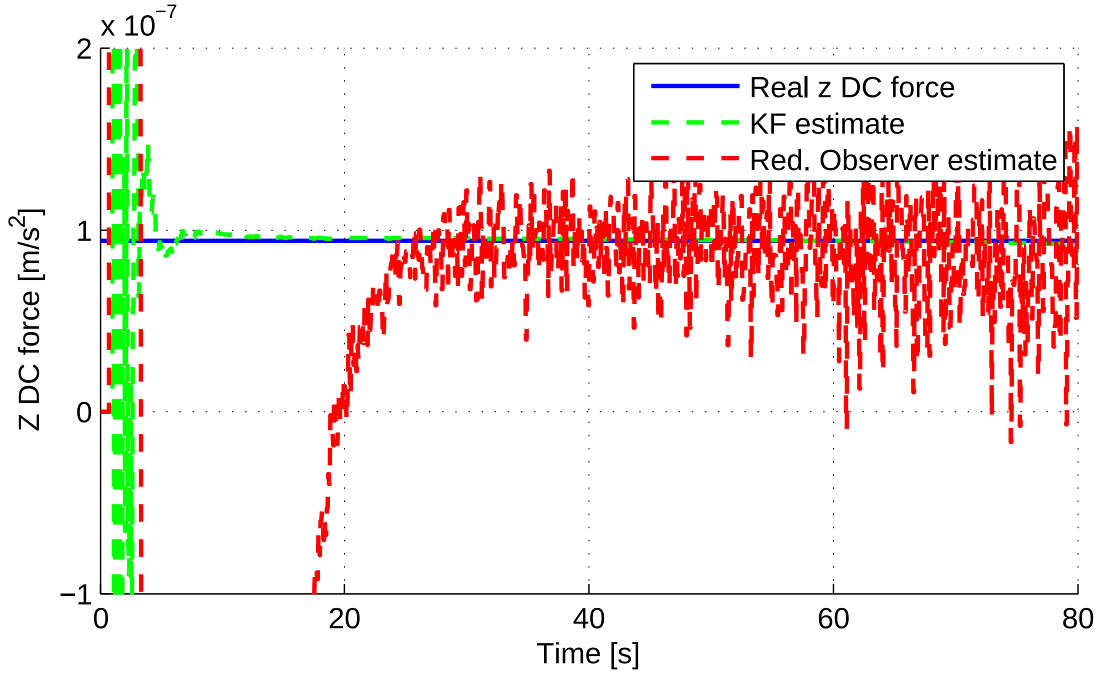


FIGURE C.10: KF and Observer DC force estimates

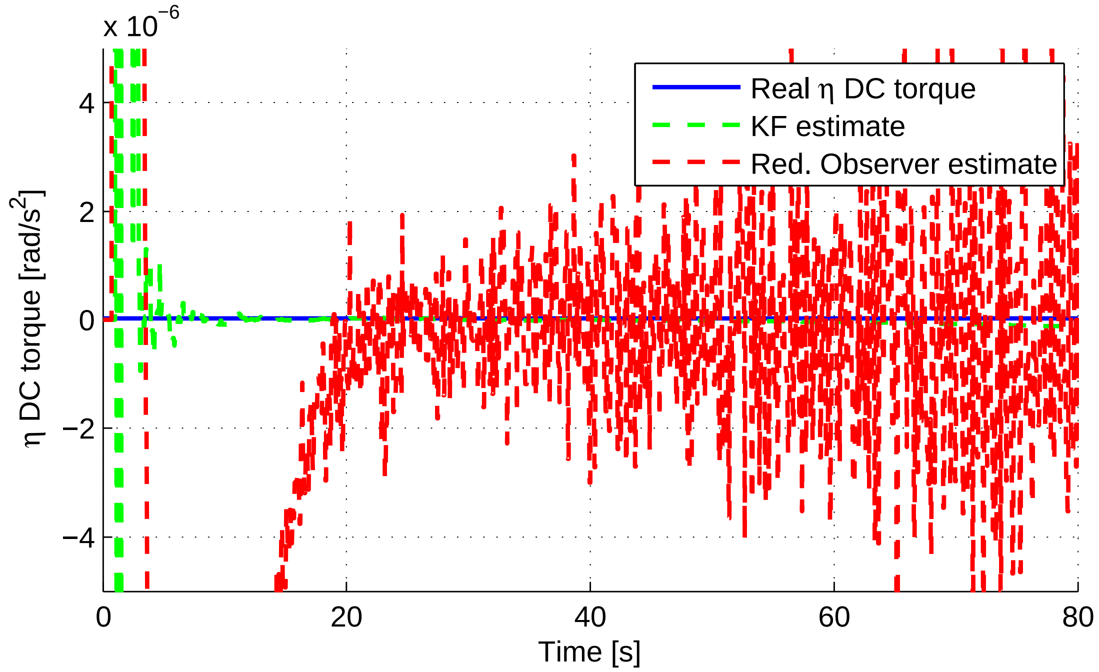


FIGURE C.11: KF and Observer DC torque estimates

### C.3.5 Disturbance forces and torques estimates errors

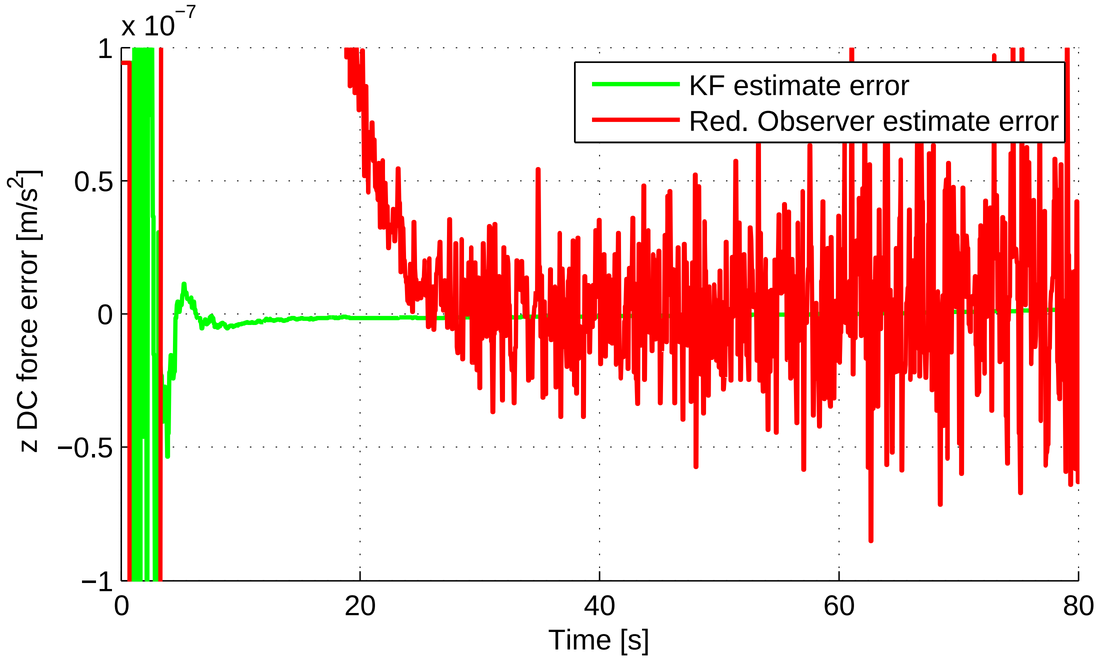


FIGURE C.12: KF and Observer DC force estimates errors

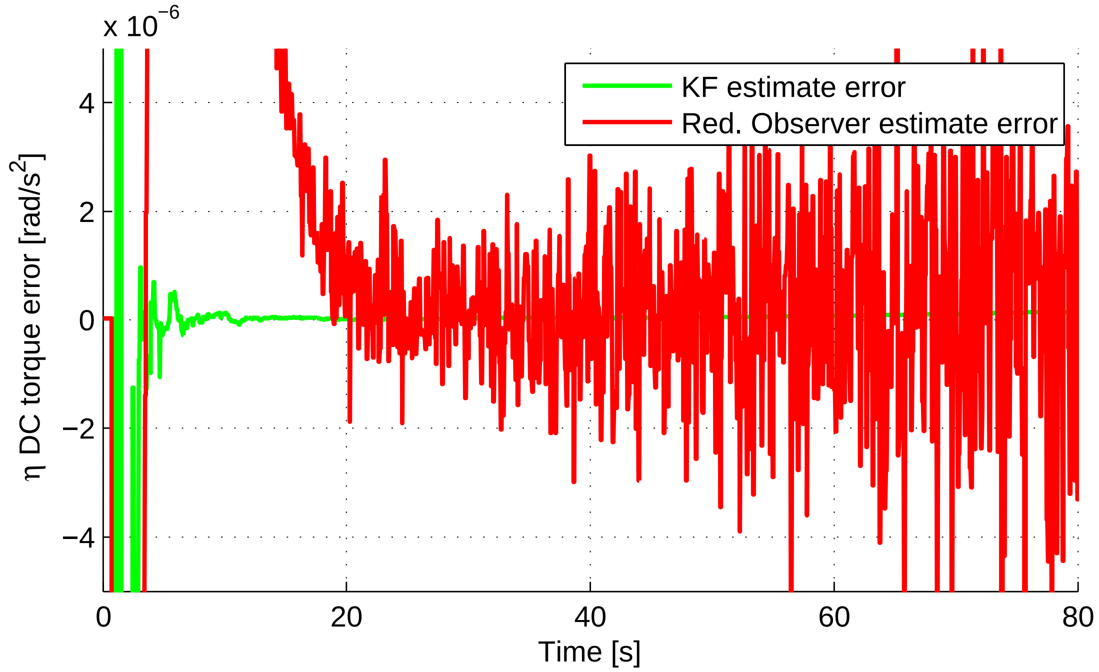


FIGURE C.13: KF and Observer DC torque estimates errors

As can be seen from the plots, the KF position estimate is essentially coincident with the measured position.
The KF velocity estimates converge to their respective correct velocity values in less than 10 seconds, while the Observer ones take about 20 seconds (two times the design settling time).
The KF disturbance forces and torques estimation takes about 10 seconds to converge, while the observer one takes about 20.
Just by comparison of the estimates plots, it is clear that the Kalman filter performance is better than the reduced states observer one, both in terms of convergence speed, and noise rejection.
When applying a command signal, however, both estimators performances are deteriorated by the commanded-to-actuated error. This deterioration affects mainly the DC forces estimation, and fades away in time. This effect is dependent on the magnitude ratio between the actuation error, and the disturbance effect to be estimated. The situation for the studied case is depicted in table C.7.

| | Translational cases [N] | Rotational cases [Nm] |
|---|---|---|
| Greatest actuation error | $F_z \cong 1.1 \cdot 10^{-6}$ | $T_\eta \cong 1.7 \cdot 10^{-7}$ |
| Greatest disturbance | $F_{Dz} \cong 1.9 \cdot 10^{-7}$ | $T_{D\theta} \cong 2.3 \cdot 10^{-11}$ |

Table C.7: Command Errors against Disturbances Comparison

By assuming the actuation error to be 5%, (which may still be an optimistic estimate) simple magnitude considerations are enough to conclude that, while translational degrees of freedom we should present no particular issues, a correct torque disturbance estimation requires an essentially perfect command torque application (which is not available). Even a 1% error in applied torque would be 100 times bigger than the disturbance torque we are willing to estimate, thus justifying the poor torque estimation performances of both the reduced state observer and the Kalman filter.

# Appendix D

# Maximum Force Actuation Algorithm

## D.1 Derivation of Maximum Force Actuation Algorithm

In this section, the derivation of the implemented maximum force actuation algorithm is presented. The final expression of the solution is omitted as it does not contribute to the problem understanding.

The general system of equations for force, torque and test mass voltage is [7]:

$$F_x = \frac{1}{2}\sum_{i=1}^{4} a_i V_i^2 \tag{D.1}$$

$$F_\varphi = \frac{1}{2}\sum_{i=1}^{4} b_i V_i^2 \tag{D.2}$$

$$V_{TM} = \sum_{i=1}^{4} c_i V_i = 0 \tag{D.3}$$

The case where a positive force and positive torque are commanded is considered. The overall concept can then be generalized by substituting the "number" (1 2 3) identification of the electrodes with the "role" (Force+Torque, Force, Torque).
As in the normal actuation algorithm, the $V_4$ electrode voltage is assumed to be zero. The equations are then:

$$F_x = \frac{1}{2}(a_1 V_1^2 + a_2 V_2^2 + a_3 V_3^2) \tag{D.4}$$

$$F_\varphi = \frac{1}{2}(b_1 V_1^2 + b_2 V_2^2 + b_3 V_3^2) \tag{D.5}$$

$$V_{TM} = c_1V_1 + c_2V_2 + c_3V_3 = 0 \tag{D.6}$$

$$V_4 = 0 \tag{D.7}$$

In this system, the torque is an input, and one of the electrode voltages $V_1$ and $V_2$ will be fixed to the maximum value of 130.1 V to get a maximum force (see section 4.2). It is therefore necessary to solve for the remaining one between $V_1$ and $V_2$, for $V_3$ and for the force $F_x$.

The zero TM potential equation is used to substitute $V_3$ with a combination of $V_2$ and $V_1$:

$$V_3 = -\frac{c_1V_1 + c_2V_2}{c_3} \tag{D.8}$$

Substituting D.8 into D.5, after some expansion and collecting of terms:

$$V_1^2\left(b_1 + b_3\frac{c_1^2}{c_3^2}\right) + 2b_3\frac{c_1c_2}{c_3^2}V_1V_2 + V_2^2\left(b_2 + b_3\frac{c_2^2}{c_3^2}\right) - 2F_\varphi = 0 \tag{D.9}$$

Equation D.9 is a second order polynomial in both $V_1$ and $V_2$ (F+T and F voltage), which can be solved for either one of them, when fixing the remaining one. By doing so, 4 possible solutions are obtained (2 solutions for $V_1$ when fixing $V_2$ and vice versa):

$$\begin{cases} V_1 = 130.1\,\mathrm{V} \\ V_2 = \dfrac{-b_3\dfrac{c_1c_2}{c_3^2}V_1 \pm \sqrt{\left(b_3\dfrac{c_1c_2}{c_3^2}V_1\right)^2 - \left(b_2 + b_3\dfrac{c_2^2}{c_3^2}\right)\left[V_1^2\left(b_1 + b_3\dfrac{c_1^2}{c_3^2}\right) - 2F_\varphi\right]}}{\left(b_2 + b_3\dfrac{c_2^2}{c_3^2}\right)} \end{cases} \tag{D.10}$$

And

$$\begin{cases} V_1 = \dfrac{-b_3\dfrac{c_1c_2}{c_3^2}V_2 \pm \sqrt{\left(b_3\dfrac{c_1c_2}{c_3^2}V_2\right)^2 - \left(b_1 + b_3\dfrac{c_1^2}{c_3^2}\right)\left[V_2^2\left(b_2 + b_3\dfrac{c_2^2}{c_3^2}\right) - 2F_\varphi\right]}}{\left(b_1 + b_3\dfrac{c_1^2}{c_3^2}\right)} \\ V_2 = 130.1\,\mathrm{V} \end{cases} \tag{D.11}$$

These solutions contain combinations of the various b and c coefficients inside square roots and in the denominator. The b and c coefficients are polynomial expressions of the relevant coordinates, whose order depends on the adopted capacitance model. This implies the need for investigating the existence of real solutions, and particular care for special cases where singularities may happen. While it has been shown that a real solution always exists for cases of interest, and the singularities can be clearly identified and avoided by adopting a proper alternative expression for the solution, the complete solution has been found impractical to implement for several reasons:

- Identification of singularities suffers from numerical issues
- The calculation has to be carried out adopting long expressions for the coefficients
- The calculation can not be generalized with respect to the force/torque command sign combination: different sets of coefficients have to be calculated depending on the input commands

A linearization in the displacements of the voltage solutions (eq D.10 and D.11), adopting a first order capacitance model for the coefficients, has then been carried out, implemented and tested.

The linearized implementation was found to produce an output force almost equivalent to the one obtained using the complete voltage solutions, while introducing significantly higher torque errors when a maximum force of the same sign of the displacement is required.

Figures D.1 D.2 and D.3 show the output force and torque plots, calculated using the $6^{th}$ order model, for the full solutions using a $4^{th}$ order capacitance model, and the linearized solutions using a $1^{st}$ order capacitance model. The plots have been generated requiring a negative maximum force and a 5 nNm torque, for varying $z$ and zero $x$ and $\eta$. Figure D.1 shows that the force generated by the voltages is essentially equivalent for the two implementations. Figure D.2 shows the generated torque for positive displacement and negative force is again essentially equivalent for the two implementations. Figure D.3 finally shows that the linearized implementation suffers from very large errors in the generated torque when the displacement and required force sign are the same. This case is however never encountered in the proposed control strategy, as requiring a maximum force of the same sign as the measured displacement means to break a velocity that reduces the displacement itself ($\dot{v} = -u_{\max} sign\,(v)$). The switching logic avoids such a scenario and therefore it can be stated that, for correct controller behaviour, the torque errors shown in figure D.3 are never encountered.

In the end, the linearized version of the solutions was chosen. The driving considerations for this choice were:

- The small difference in terms of generated force and torque with respect to the ones obtained using the complete solutions, when a reasonable combination of force/displacement signs was considered;
- The vastly superior implementation flexibility of the linearized approach.

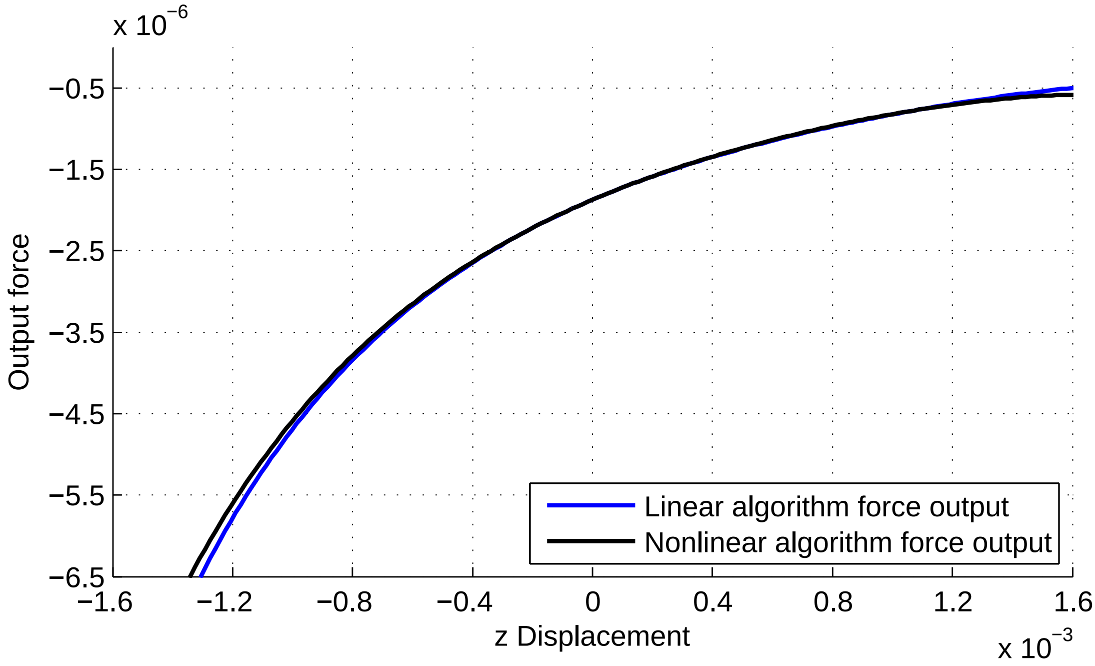


FIGURE D.1: Generated forces for complete and linearized maximum force actuation algorithm implementations

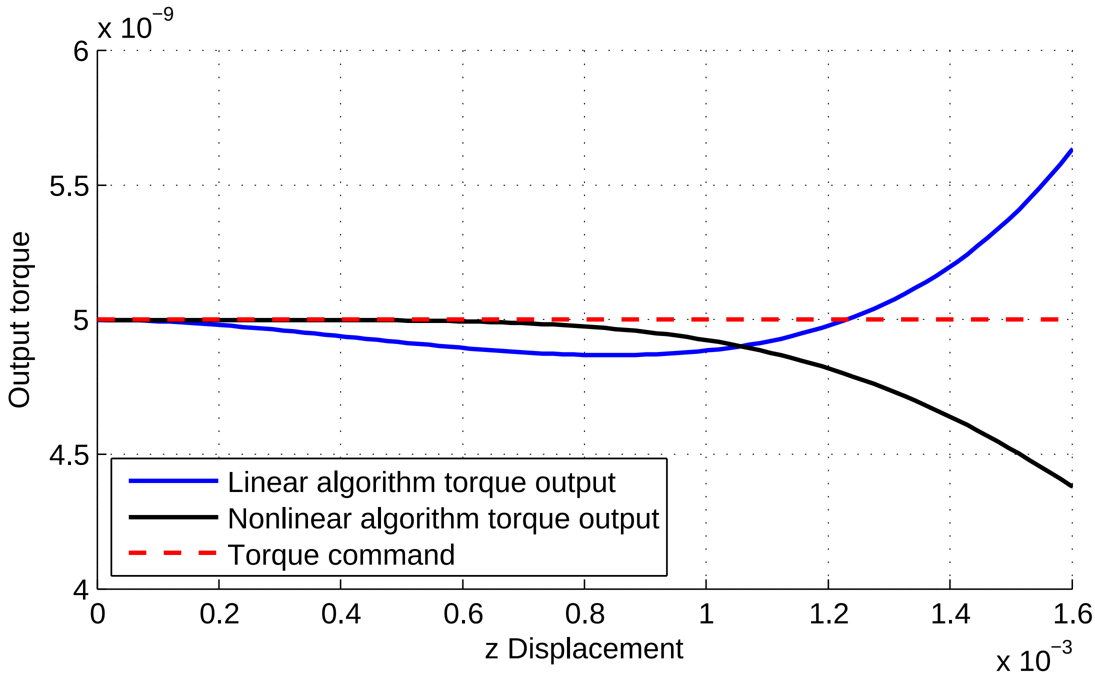


FIGURE D.2: Generated torques for complete and linearized maximum force actuation algorithm implementations, positive z displacement

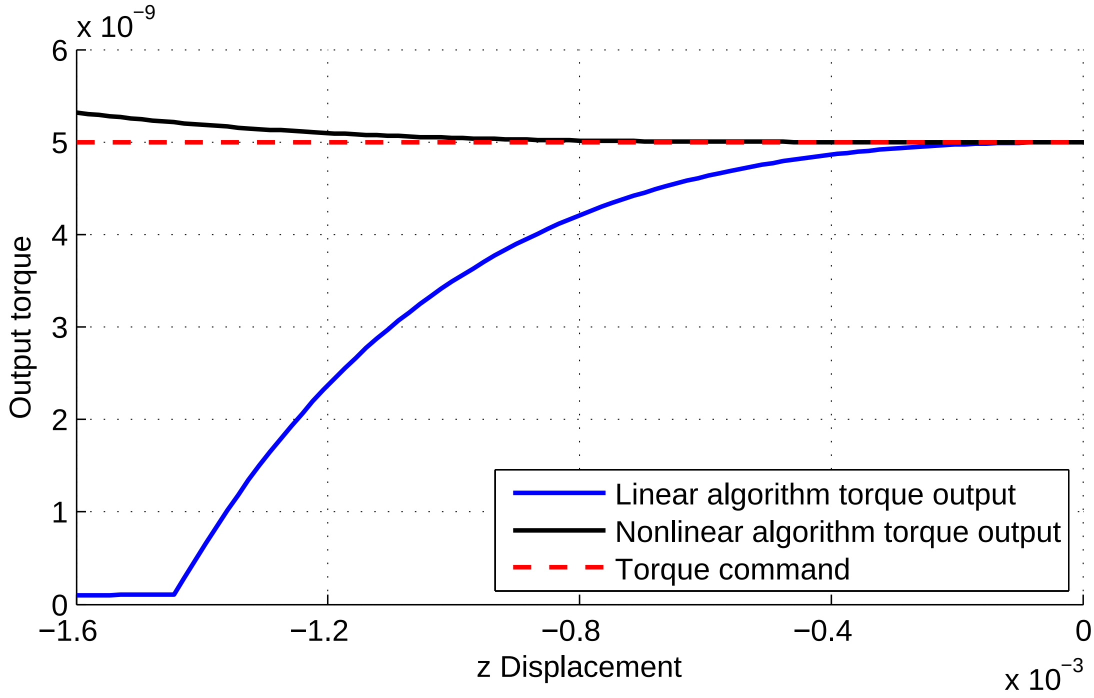


FIGURE D.3: Generated torques for complete and linearized maximum force actuation algorithm implementations, negative z displacement

When finally all the solutions (in terms of voltage triplets $V_1$ $V_2$ $V_3$) have been computed, a check is performed, to exclude every triplet that contains one or more voltages outside the saturation limits.

The force associated with the remaining voltage triplets is then computed using a first order capacitance model.

The highest computed force is picked as final solution.

The correct voltage triplet, yielding the maximum possible actuated force for the particular displacements combination, while producing the required torque, is the one used to compute the force picked at the previous step.

This procedure allows to know both the value of the maximum force that can be generated for given conditions, and the voltages needed to produce it. A schematic representation of the procedure is given in figure D.4.

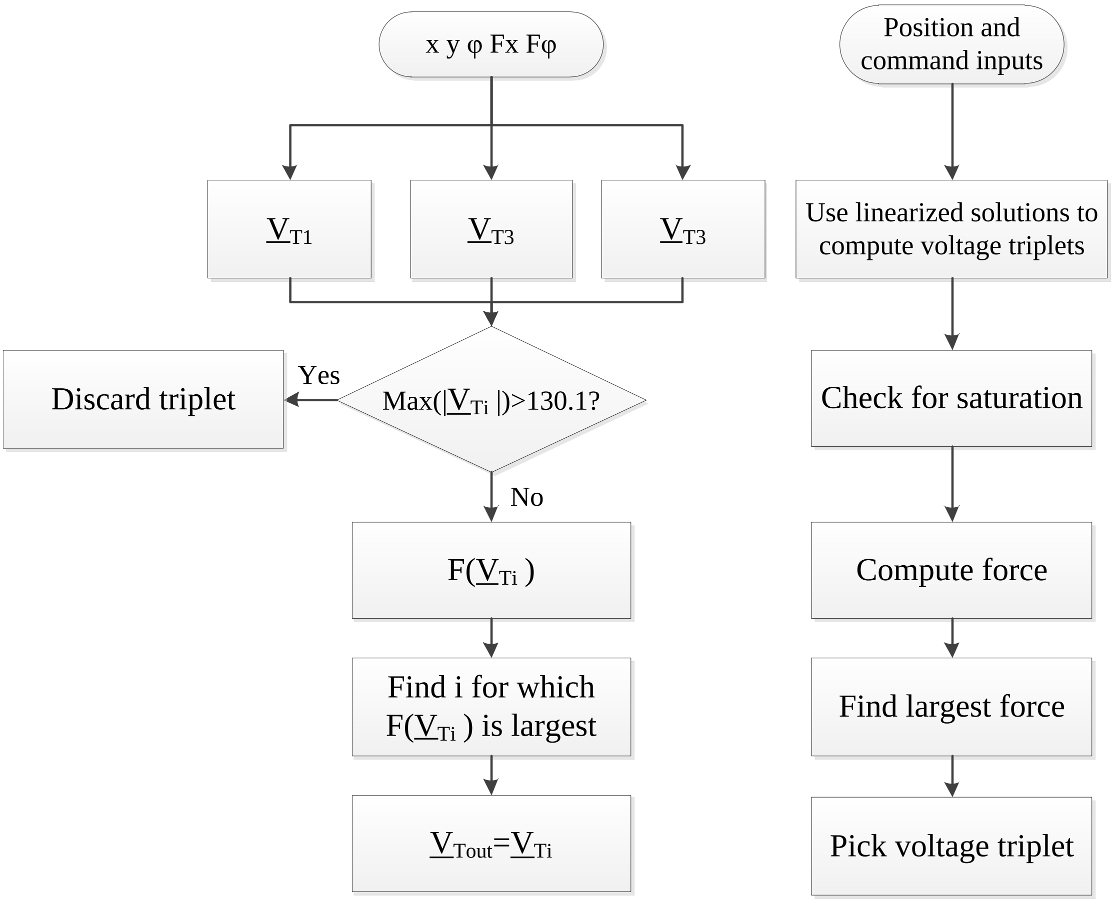


FIGURE D.4: Schematic diagram of the maximum force actuation algorithm logic

## D.2 Evaluation of Minimum Torque Limit

In this section, a simplified evaluation of the minimum torque required to avoid the maximum angular overshoot, for a given initial rotation and rotational rate is carried out.

In order to be able to gain advantage from the force maximization concept, it is needed to limit the torque input to a low level, such that the major portion of the available electrostatic actuation authority will be used in producing force.
An assessment of the minimum needed torque actuation is developed, by giving the condition that, at maximum overshoot conditions (which is defined as the maximum accepted displacement) the test mass attitude rate must be zero:

$$q_{\max} = q\left(t_{\max} + t_{drift}\right) \tag{D.12}$$

$$v\left(t_{\max} + t_{drift}\right) = 0 \tag{D.13}$$

The equations of motion for the rotational degree of freedom write:

$$q\left(t_{\max}+t_{drift}\right)=q_0+v_0\left(t_{\max}+t_{drift}\right)+\frac{1}{2}a_{DC}t_{drift}^2+\frac{1}{2}a_{eff}t_{\max}^2 \tag{D.14}$$

$$v\left(t_{\max}+t_{drift}\right)=v_0+a_{DC}t_{drift}+a_{eff}t_{\max} \tag{D.15}$$

Where:

- $t_{drift}$ is the test mass free drifting time (after release and before start of control)
- $t_{max}$ is the amount of time, measured starting from $t_{drift}$, that it takes to reach the maximum overshoot conditions
- $q_0$ and $v_0$ are, respectively, position and velocity initial conditions
- $a_DC$ is the test mass disturbance acceleration
- $a_eff$ is the test mass effective acceleration, defined as $a_{DC}+a_{CMD}$

From orders of magnitude considerations:

- $a_{CMD}\cong 10^{-5}\frac{rad}{s^2}$
- $a_{DC}\cong 10^{-8}\frac{rad}{s^2}$

Neglecting in both equations the terms that multiply $a_{DC}$, the following set of equations is obtained:

$$q\left(t_{\max}+t_{drift}\right)=q_0+v_0\left(t_{\max}+t_{drift}\right)+\frac{1}{2}a_{eff}t_{\max}^2\leq q_{\max} \tag{D.16}$$

$$v\left(t_{\max}+t_{drift}\right)=v_0+a_{eff}t_{\max}=0 \tag{D.17}$$

By isolating $t_{max}$ in equation D.17, and substituting it in equation D.16, the latter becomes:

$$q_0+v_0\left(-\frac{v_0}{a_{eff}}+t_{drift}\right)+\frac{1}{2}a_{eff}\left(\frac{v_0}{a_{eff}}\right)^2\leq q_{\max} \tag{D.18}$$

After some algebra, the inequality for the acceleration becomes:

$$a_{eff}\geq\frac{v_0^2}{2\left(q_{\max}-\left(q_0+v_0t_{drift}\right)\right)} \tag{D.19}$$

Then, applying the definition of $a_{eff}$:

$$a_{CMD}\geq\frac{v_0^2}{2\left(q_{\max}-\left(q_0+v_0t_{drift}\right)\right)}-a_{DC} \tag{D.20}$$

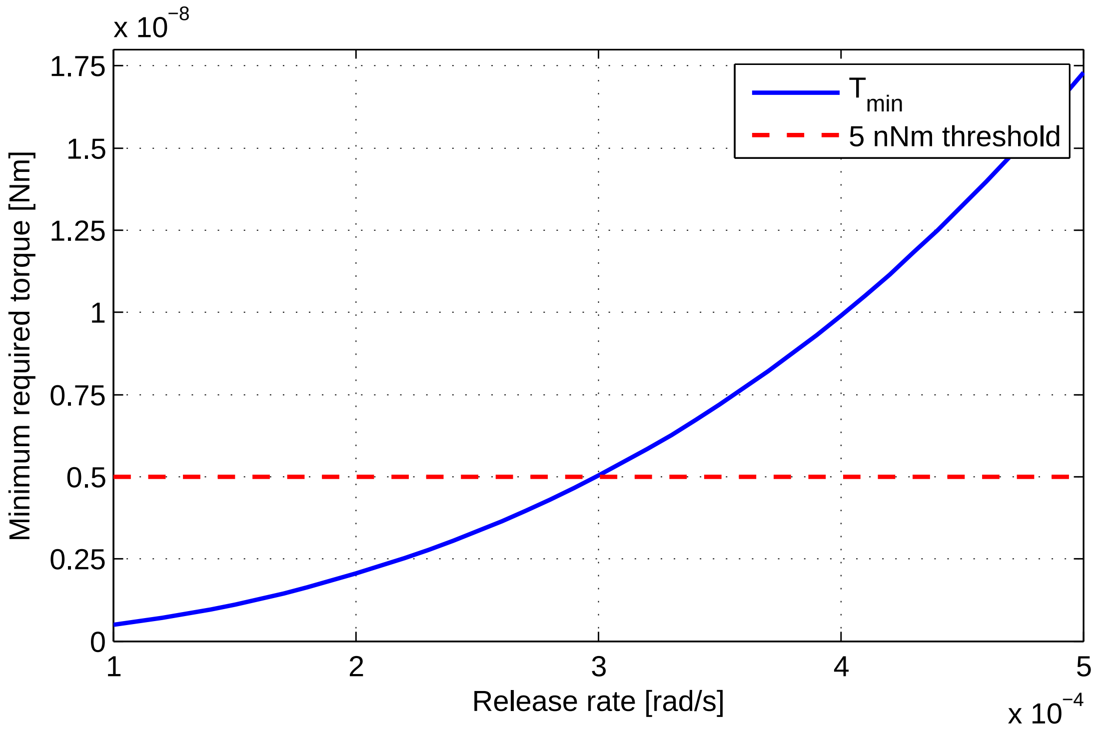


FIGURE D.5: Minimum required torque for 10 mrad maximum overshoot

Which can be expressed more conservatively as:

$$a_{CMD} \geq \frac{v_0^2}{2\left(q_{\max} - \left(q_0 + v_0 t_{drift}\right)\right)} + |a_{DC}| \tag{D.21}$$

The results of application of equation D.21 with the available data, for various values of initial velocity (for a fixed 10 mrad maximum overshoot) or maximum allowed overshoot (for a fixed 0.1 mrad/s release angular velocity), are shown in figures D.5 and D.6. The 5 nNm value chosen as torque limit for attitude controller is shown. The case shown in the pictures is for the $\theta$ DOF, but the result is analogous for any of the rotational DOF, the difference being only in the $a_{DC}$ term, which is anyway of negligible magnitude. Looking at the results given in figures D.5 and D.6, and considering that the maximum torque actuation authority is in the order of $10^{-8}$ Nm, it can be concluded that a 5 nNm torque is sufficient to prevent the test mass attitude from reaching maximum overshoot values.

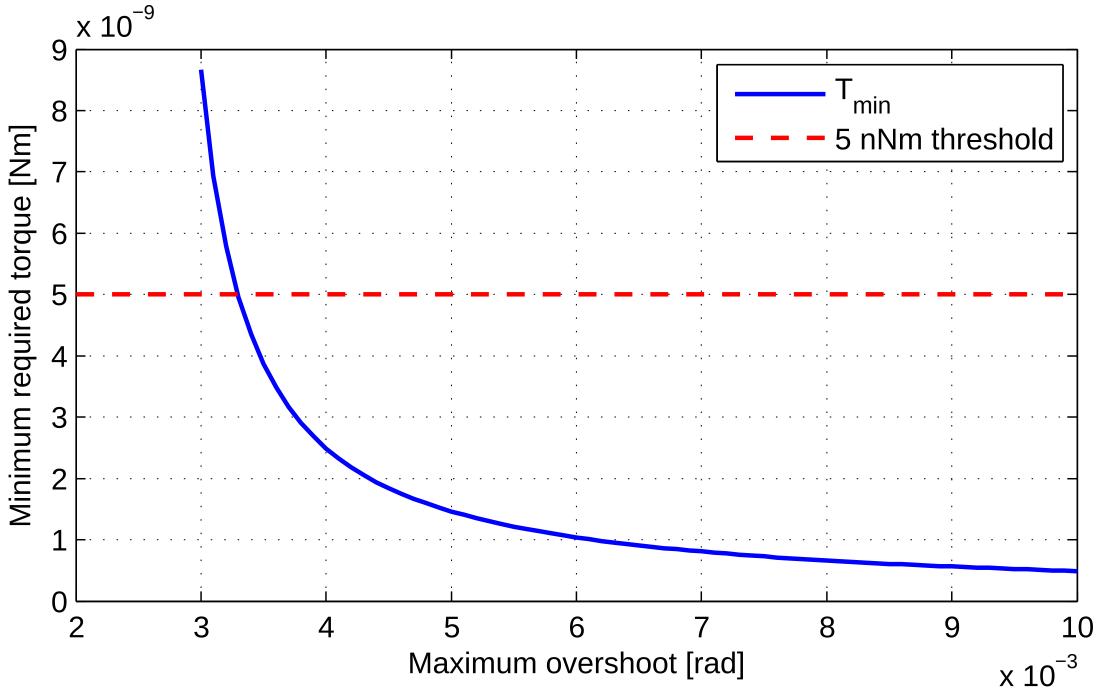


FIGURE D.6: Minimum required torque for 0.1 mrad/s release rate

## D.3 Maximum Force Command Calculation for Estimator Input

In this section, the problem of providing the state estimator with a command input when operating in the "maximum actuation" regime is addressed.

Due to the absence of a "real" force command output from the controller, while operating in its velocity breaking regime, the need arose for an evaluation of the actuated maximum force. A resulting force computation was included in the capacitive actuation algorithm which, based on the selected voltage triplet, carried out the calculation of the output force and provided it as an output, which was then used as input in the Kalman filter.

However, due to the practical necessity of using a first order capacitance model in the calculations, large errors were being introduced as the displacement grew. A comparison of the actuated force for full voltage on two electrodes, computed with $1^{st}$ and $6^{th}$ order models is shown in Figure A 16. Using as filter input the force computed with the first order model introduced huge filter errors, particularly on the disturbance estimate. A strategy was adopted, exploiting the knowledge that, beyond a certain limit, the "real" force showed an asymptotic-like behavior. With this in mind, the force output computed using the linear model was "cut" when it fell below a certain magnitude, and was substituted with a constant value (see figure D.8). The optimal constant value to adopt was calculated by minimizing the squared error between the first order model

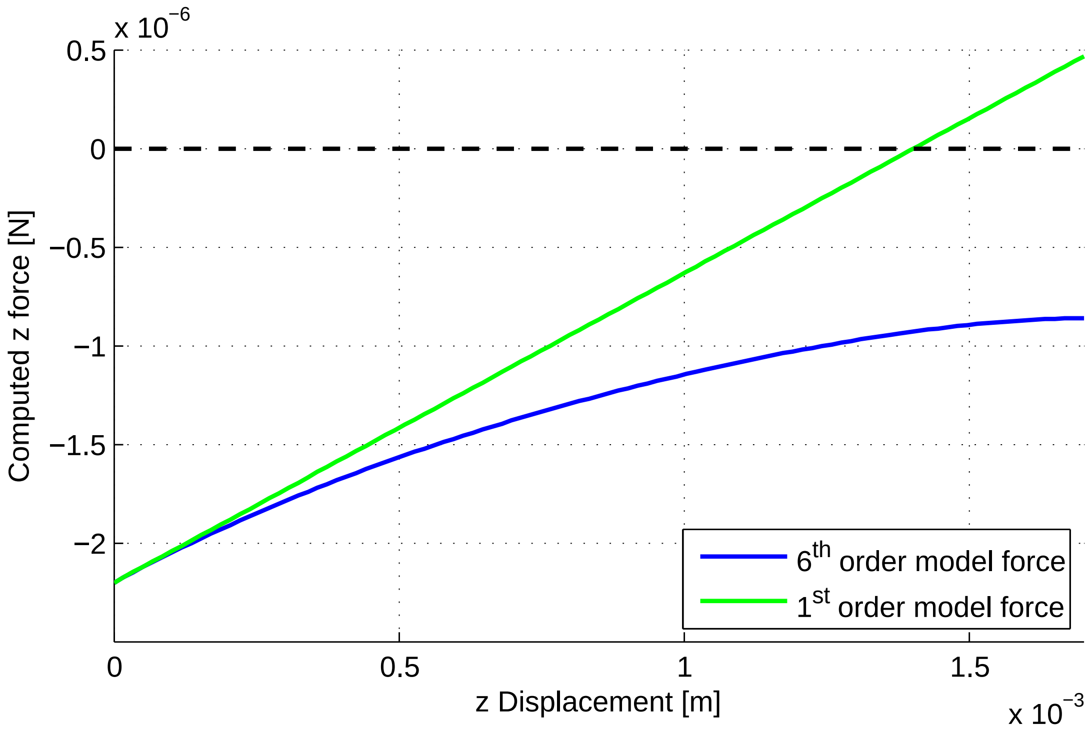


Figure D.7: Comparison of computed force for $1^{st}$ and $6^{th}$ order capacitance model

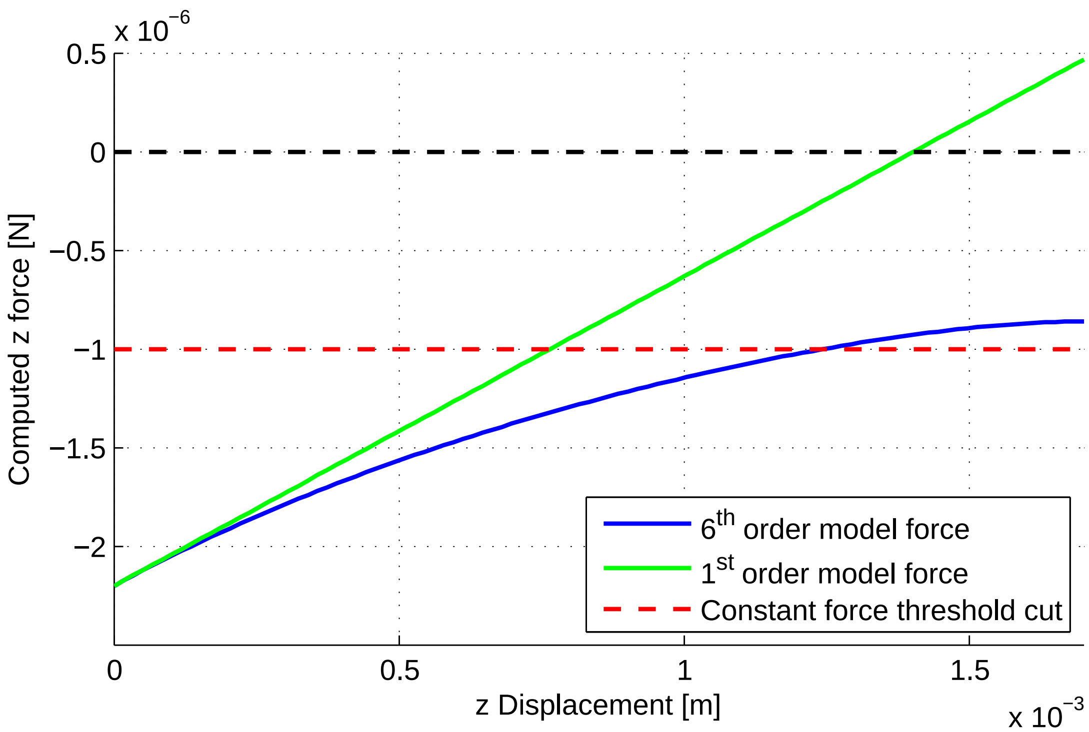


Figure D.8: Composition of corrected force output

output and the $6^{th}$ order model output. The optimization was carried out between nominal position and the assumed (1.7 mm) validity limit of the $6^{th}$ order model.
The case of a negative $z$ force for positive z displacement is considered. The simplified case of full voltage application on two electrodes is adopted. The assumed real force is calculated with the $6^{th}$ order model:

$$F_{6th} = \frac{1}{2}2\left(\frac{dC_{EL,TM}}{dz} + \frac{dC_{EL,H}}{dz}\right)_{6th} V_{\max}^2 \tag{D.22}$$

The force calculated with the $1^{st}$ order model is:

$$F_{1st} = \frac{1}{2}2\left(\frac{dC_{EL,TM}}{dz} + \frac{dC_{EL,H}}{dz}\right)_{1st} V_{\max}^2 \tag{D.23}$$

The computed output force is calculated with the $1^{st}$ order model, and then cut to a constant value:

$$F_{out} = \begin{cases} F_{1st} & z < z_c \\ F_{1st}\left(z_c\right) & z \geq z_c \end{cases} \tag{D.24}$$

The calculation of the integral the squared error between the assumed real force, and the output force, as a function of the cut displacement $z_c$ is carried out. The integral is truncated at the assumed $6^{th}$ order model validity limit, which in the case of the $z$ coordinate, is 1.7 mm.

$$SquaredError = \int_0^{z_{\lim}} \left(F_{6th} - F_{out}\right)^2 dz \tag{D.25}$$

$$SquaredError = \int_0^{z_c} \left(F_{6th} - F_{1st}\right)^2 dz + \int_{z_c}^{z_{\lim}} \left(F_{6th} - F_{1st}\left(z_c\right)\right)^2 dz \tag{D.26}$$

The value of $z_c$ which zeroes the derivative of the computed integral is found, and a verification that it represents a minimum by looking at the sign of the second derivative is performed. The resulting output force is shown in figure D.9 for the $z$ case. Resulting values for the three degrees of freedom are reported in table D.1.

| | $q_c$ | $\lvert F_{1st}\rvert\left(q_c\right)$ |
|---|---|---|
| $x$ | $8.654 \cdot 10^{-4} m$ | $1.877 \cdot 10^{-6} N$ |
| $y$ | $6.182 \cdot 10^{-4} m$ | $1.980 \cdot 10^{-6} N$ |
| $z$ | $7.385 \cdot 10^{-4} m$ | $1.042 \cdot 10^{-6} N$ |

Table D.1: Resulting values for force threshold

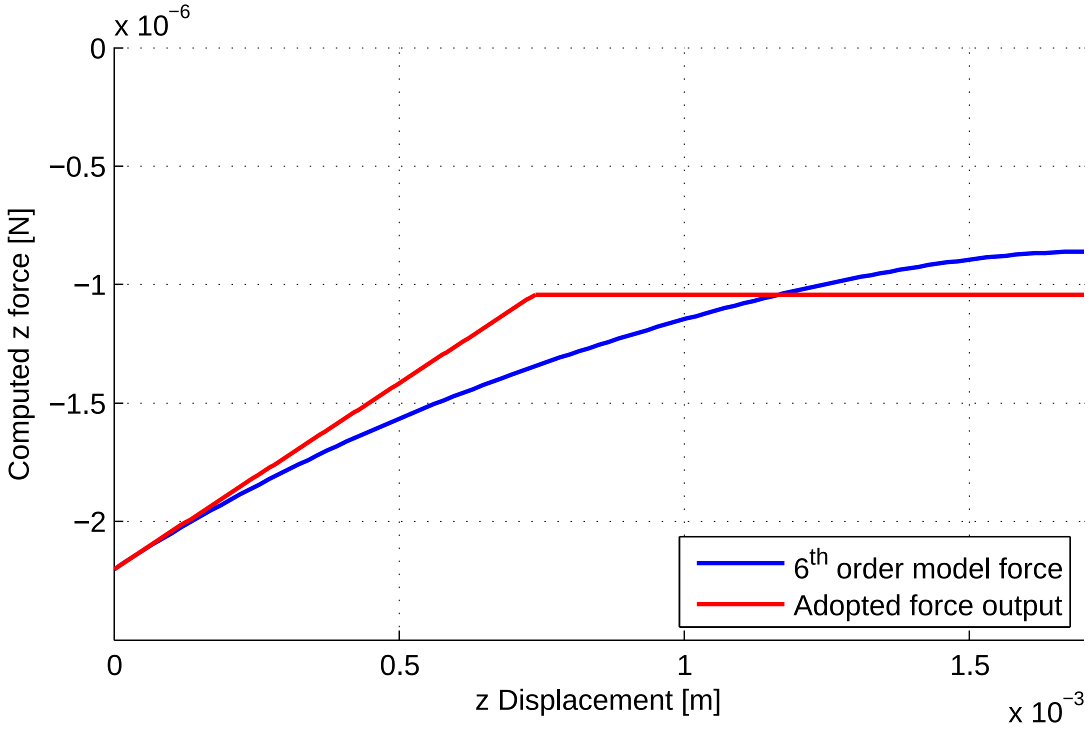


FIGURE D.9: Adopted force calculation output

# Bibliography

[1] D. Simon. *Optimal State Estimation.* John Wiley & Sons Inc, 2006.

[2] N. Brandt. Test Mass Actuation Algorithm for DFACS. Technical Note, EADS Astrium, 2011.

[3] N. Brandt and W. Fichter. Revised electrostatic model of the LISA Pathfinder interial sensor. *Journal of Physics*, 154(1), 2008. URL http://stacks.iop.org/1742-6596/145/i=1/a=012008.

[4] T. Ziegler F. Montemurro. DFACS Accelerometer Mode Design and Analysis. Technical note, EADS Astrium, 2005.

[5] J. Bik. LISA Pathfinder DFACS Alternative Accelerometer Mode Controllers Tuning Performance and Analysis. YGT final report, ESA, 2005.

[6] Li Weiping J. J. Slotine. *Applied Nonlinear Control.* Prentice Hall, 1991.

[7] R. Schulte. Design and Analysis of an Improved Actuation Algorithm for Inertial Sensors in Space. Bachelorthesis, Otto-von-Guericke Universität Magdeburg, Fakultät für Elektrotechnik und Informationstechnik, Institut für Automatisierungstechnik, 2013.

[8] A. Schleicher. DFACS Requirement Specification. Requirements specification, EADS Astrium, 2001.

[9] P. Ehrhardt T.Ziegler. Acc_derive_disturbances, 2011. MATLAB script.

[10] J. Powell F. Franklin. *Feedback Control of Dynamic Systems.* Addison-Wesley Publishing Company, 3rd edition, 1993.

[11] H. Musoff P. Zarchan. *Fundamentals of Kalman Filtering: A Practical Approach.* AIAA, 2005.

[12] P. J. Olver. Nonlinear ordinary differential equation lecture notes. Available at www.math.umn.edu/~olver/index.html[cited 5 Oct. 2013], 2012.

[13] R. Hannes. An Improved Analytical 6-DoF Electrostatic Force and Torque Model for the LISA Pathfinder Inertial Sensor. Technical report, Astrium GmbH, 2009.

[14] S. Vitale et al. *The LISA Technology Package on board SMART-2*. Unitn-Int Trento, 2002.

[15] C. Zanoni D. Bortoluzzi, S. Vitale. Test Mass Release Testing. Technical report, Università degli studi di Trento, September 2013.

[16] John B. Moore Teng-Tiow Tay, Iven Mareels. *High Performance Control*. Birkhäuser, 1998.

[17] A. Schleicher. DFACS external interface control document. Technical report, Astrium GmbH, 2013.